

國立交通大學  
光電工程研究所

碩士論文

寬能隙半導體微共振腔強耦合作用之研究

Strong Coupling Regime in Wide Bandgap

Semiconductor Microcavity

研究生：林詳淇

指導教授：盧廷昌教授

中華民國九十九年七月

寬能隙半導體微共振腔強耦合作用之研究  
Strong coupling regime in wide bandgap semiconductor  
microcavity

研究生：林詳淇

Student：Shiang-Chi Lin

指導教授：盧廷昌 教授

Advisor：Tien-Chang Lu

國立交通大學電機資訊學院

光電工程研究所

碩士論文

A Thesis

Submitted to Institute of Electro-Optical Engineering  
College of Electrical Engineering and Computer Science

National Chiao Tung University

in Partial Fulfillment of the Requirements

for the Degree of

Master

In

Electro-Optical Engineering

July 2010

Hsinchu, Taiwan, Republic of China

中華民國 九十九 年 七 月

# 寬能隙半導體微共振腔強耦合作用之研究

研究生：林詳淇

指導教授：盧廷昌 教授

國立交通大學光電工程研究所

## 摘要

半導體微共振腔中在強耦合作用下，光子與激子會混合形成新的準粒子，我們稱之為極化子(polariton)，這樣的粒子具有玻色子的特性，其有效質量很小並且擁有可調變的色散曲線，因此在研究固態系統的光與物質交互作用中，半導體微共振腔是一項十分有潛力的研究領域。在此論文中，我們主要著重於在強耦合作用下寬能隙材料的微共振腔特性研究，分別為混合型氧化鋅微共振腔以及電激發氮化鋁/氮化鎵多量子井微共振腔。

首先，我們研究混合型氧化鋅微共振腔中的高反射率分布式布拉格反射鏡，其結構為四分之一光學厚度的氮化鋁/氮化鎵薄膜組成。在 20 對氮化鋁/氮化鎵分布式布拉格反射鏡中，反射率為 97.2% 並且停止帶的寬度為 36.6 奈米。另外，值得注意的是氮化鋁/氮化鎵分布式布拉格反射鏡其反射率中心波長短於 380 奈米時，反射頻譜會受到氮化鎵嚴重的吸收使得反射率下降。實驗結果可藉由轉換矩陣計算出在考慮氮化鎵的吸收時反射頻譜的變化。

藉由 1.5 光學厚度的氧化鋅微共振腔，我們在室溫條件下，分別在反射頻譜和螢光激發頻譜觀察到 68 meV 的拉比分裂值(Rabi-splitting)。然而在實驗結果中，上極化子由於與激子連續態的散射，使得在實驗結果中無法清楚地觀察到上極化子分支。另外，為了對上極化子分支的鑑別度做進一步的討論，我們藉由數值模擬的方式對不同物理機制條件下的上極化子分支做討論。模擬結果顯示在氧化

鎘與氧化鋅的微共振腔中，其主動層厚度分別在 $\lambda$  和  $0.25\lambda$ 的情況下，上極子分支會變的無法分辨，主要的原因是在於寬能隙材料塊材的微共振腔中，具有較大的厚度與吸收係數之間乘積。另外，在共振腔與激子兩者模態的能量差距的選擇上，會偏向於能量差為負值，因為在此條件下，上極化子在較小的波向量會偏向激子特性，較不會發生激子連續態散射情形。此外，在寬能隙材料當中，上極化子分支的鑑別度也會同時受到非均勻性變寬的影響。而在結構的設計上，量子井結構的微共振腔因為具有較大的激子束縛能以及較小的厚度與吸收係數乘積，所以在結構的考量上，量子井結構的微共振腔相較於塊材結構會較容易觀察到上極化子分支。

在此碩論的最後章節中，我們在電激發氮化銦鎘的微共振腔中觀察到強耦合的情況。藉由變溫電激發頻譜，我們在 280k 的溫度條件下觀察到 6meV 的拉比分裂值。另外，我們再藉由變角度電激發頻譜的實驗，在 7.4 度的收光角度下觀察到 7meV 的拉比分裂值。最後我們在改變注入電流的情形下，可以發現隨著注入電流的增加拉比分裂值也隨著變小，進一步地證明我們在電激發氮化銦鎘微共振腔元件中觀察到激子與光子的強耦合現象。

# Strong coupling regime in wide bandgap semiconductor microcavity

Student : Shiang-Chi Lin

Advisor : Tien-Chang Lu

Institute of Electro-Optical Engineering, National Chiao Tung University

## Abstract

In the strong coupling regime, a new quasi-particle termed cavity –polariton with bosonic characteristics is created from the mixing of photons and excitons. It has very small effective mass as well as controllable dispersion curves, so that semiconductor microcavities (MCs) have been widely investigated due to the enhanced control of light-matter interaction in solid-state systems. In the thesis, we focus the strong coupling regime between cavity photon and exciton in two wide bandgap semiconductor microcavities—ZnO based hybrid microcavity and InGaN/GaN multiple-quantum-well microcavity.

First of all, we investigate high-reflectivity blue-violet distributed Bragg reflectors (DBRs) based on AlN/GaN quarter-wave layers for the hybrid ZnO-based MCs. The 20-pairs AlN/GaN DBRs achieve peak reflectivity of 97.2% at 440 nm together with a stopband width of 36.6 nm. Furthermore, the growth of 20-pair AlN/GaN DBR will suffer significant influence of GaN absorption when the designed DBR wavelength is shorter than about 380 nm. The experimental reflectivity spectra are modeled by transfer matrix theory including the effect of GaN absorption to compare the experimental and theoretical results.

For bulk ZnO-based microcavity with  $1.5\lambda$  optical thickness, we observed a vacuum Rabi-splitting as large as 68 meV at RT based on the angle-resolved photoluminescence and reflectivity experiments. It is found that the upper polariton branch (UPB) is blurred in both experiments due to the absorption from scattering states. Furthermore, we present in detail the possible physical mechanisms leading to the broadening of UPBs for different designs of MCs by numerical simulations based on GaAs, GaN and ZnO materials. The calculated results show that the UPBs of the GaN- and ZnO-based MCs will become indistinct when the thickness of optical cavity is larger than  $\lambda$  and  $0.25\lambda$ , respectively, mainly attributed to the larger product of the absorption coefficient and the active layer thickness. In wide-bandgap materials, it would be relatively easier to observe the UPB in the case of negative exciton-photon detuning due to the exciton-like UPB and lower absorption of scattering states. In addition, the inhomogeneous broadening would be an important factor causing the invisible UPB in wide-bandgap semiconductor MCs. We demonstrate that in a ZnO/ZnMgO multiple-quantum-well MCs, the UPB could be well-defined due to the large 2D exciton binding energy and the small product of absorption coefficient and active layer thickness. These results show that the UPBs can be properly defined in wide-bandgap semiconductor MCs by appropriate design of MC structures.

In the last of the thesis, we report the strong coupling regime in electrically pumped InGaN-based microcavity. Through the temperature-dependent electroluminescence (EL) spectra, there is a Rabi-splitting about 6 meV at a

temperature of 280 K. Moreover, the angle-resolved EL spectra at 180 K show the 7-meV Rabi-splitting at  $7.4^\circ$ , and the splitting value between lower polariton and upper polariton decreases with the increase of current density, which further evidence the strong coupling regime in electrically pumped InGaN-based microcavity.



## Acknowledgements

時間過的很快，從專題生到畢業，在實驗室也待了三年。首先，這期間最要感謝的就是盧廷昌老師這三年來耐心的教導，從一個連量子觀念都不懂的大專生，到現在順利的完成學位碩士生，每兩個禮拜充實的 meeting，讓我在這三年間成長了不少，十分感謝老師這三年來的栽培。當然還有郭浩中老師與王興宗老師對我的指導，也讓我在研究上的態度有更有想法與堅持。

另外，我要特別感謝的就是把我一手帶大的俊榮學長以及和我一起奮鬥的永吉。俊榮學長為人熱心，時常搭配著爽朗的笑聲出場，和學弟的相處就像朋友一樣。在研究上不論是實驗或是觀念都很有條理和見解，真的很慶幸能有這樣的機會給學長指導。而我的最佳實驗夥伴火星人永吉，在實驗上真的幫了很大的忙，模擬方面更是一把罩，每次與他的討論總是能獲得建設性的意見。這兩位學長對我的碩士生研究，真的是不可或缺的貴人啊！

最後還要感謝一起奮鬥的實驗室同仁們，跟我一樣是 GB 系列的阿伯、憨厚網球一哥信助、吃飯不找不行的板弟，擁有陽光般笑容的 Joseph、超麻吉但腦子有洞的傻子，超有趣開心果奇葩獸皇，很對 tone 的 Roommate 菲哥、不知長褲為何物的辣妹依寧、個性滿點的惟雯、超活潑且語不驚人死不休的嗡嗡、帶點正經又和李博擊拳的阿翔、緩速靈氣的”絕”高手小胖、擁有水汪汪大眼的哭哭、話不容易接的怪怪美少女小邱、話不少的彥群、還有新上任的 Microcavity 一哥思維、表裡不如一的阿國等等.....。這些人為我的碩士班生涯添加了許多回憶和歡笑，真的很開心能認識你們，也祝福大家在未來的路上都能有很好很好的發展。半導體雷射實驗室超酷的啦。

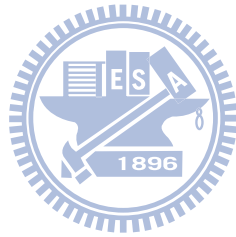


## Content

<b>Abstract (in Chinese)</b> .....	<b>i</b>
<b>Abstract(in English )</b> .....	<b>iii</b>
<b>Acknowledgement</b> .....	<b>vi</b>
<b>Content</b> .....	<b>vii</b>
<b>List of Figures</b> .....	<b>x</b>
<b>Chaper 1. Introduction</b> .....	<b>1</b>
1.1 Semiconductor Microcavity.....	1
1.2 Strong coupling regime in semiconductor microcavity.....	4
1.3 Wide bandgap semiconductor microcavity.....	7
<b>Chaper 2. Microcavity polaritons</b> .....	<b>12</b>
2.1 Strong coupling regime and weak coupling regime.....	12
2.2 What are microcavity Polaritons.....	19
2.2.1 Wannier-Mott exciton.....	19
2.2.2 Semiconductor microcavity cavity mode.....	21
2.2.3 Microcavity polaritons.....	24
2.3 Microcavity polaritons characteristics.....	26
<b>Chaper 3. Strong coupling regime in hybrid ZnO-based microcavity</b> .....	<b>35</b>
3.1 Sample Material and Structure.....	35

3.1.1	Ultra-Violet Distributed Bragg Reflectors.....	36
3.1.2	Microcavity Structure Design and Quality.....	41
3.2	Angle-Resolved Reflectivity.....	42
3.2.1	Principles and Setups.....	42
3.2.2	Simulation Model.....	44
3.2.2.1	Transfer matrix model.....	44
3.2.2.2	Oscillator model of strong coupling regime.....	48
3.2.3	Experimental results of strong coupling regime in ZnO microcavities.....	48
3.2.4	Exciton scattering states absorption.....	50
3.3	Broadening of upper polariton branch.....	52
3.3.1	Comparison of UPB broadening between microcavities based on different materials.....	53
3.3.1.1	Influence of the active layer thickness.....	56
3.3.1.2	Influence of exciton-cavity detuning.....	58
3.3.2	Influence of inhomogeneous broadening.....	59
3.3.3	Comparison between QWs-embedded and bulk ZnO-based microcavities.....	62
 <b>Chaper 4. Strong coupling in InGaN/GaN multi quantum well vertical cavity surface emitting laser.....</b>		<b>80</b>
4.1	Introduction.....	80

4.2	InGaN/GaN multi quantum well microcavity structure.....	84
4.3	Electroluminescence setup and principle.....	85
4.4	Experimental results.....	85
4.4.1	Temperature-dependent electroluminescence.....	85
4.4.2	Angle-resolved electroluminescence.....	89
4.4.3	Current-dependent electroluminescence.....	90
<b>Chaper 5.</b>	<b>Conclusion.....</b>	<b>96</b>



## List of Figures

Fig 1.1. Various schemes of lasing with semiconductors.....	11
Fig 2.1. The time-dependence of these probabilities.....	30
Fig 2.2. Damped Rabi oscillations for different ratio of the damping rate $\gamma$ .....	30
Fig 2.3. Schematic diagram of a free exciton.....	31
Fig 2.4. Reflection spectra of a typical distributed Bragg mirror.....	31
Fig 2.5. Reflectance of an empty $\lambda/2$ microcavity.....	32
Fig 2.6. Incidence angle $\theta$ dependence of the cavity reflectance.....	32
Fig 2.7. Cavity dispersion $E_{cav}$ vs. $\theta$ .....	33
Fig 2.8. Anti-crossing of LP and UP energy levels when tuning the cavity energy across the exciton energy by transfer matrix calculation.....	33
Fig 2.9. Polariton dispersions and corresponding Hopfield coefficients.....	34
Fig 3.1. Total <i>in-situ</i> reflectance signal at 440 nm for the growth of DBR I.....	65
Fig 3.2. The cross-section SEM images of DBRs I-VI.....	66
Fig 3.3. Measured and simulated reflectivity spectra of DBR I- VI.....	67
Fig 3.4. Measured and calculated maximum reflectivity values and stopband widths of the DBRs I-VI.....	68
Fig 3.5. (a) The schematic diagram of the ZnO-based hybrid microcavity. (b) The cross section image of the ZnO microcavity with bottom DBRs observed by SEM.....	68
Fig 3.6. Photoluminescence spectrum from the half-cavity ZnO film grown on AlN/AlGaN DBRs.....	69
Fig 3.7. Reflectivity spectra of a 30-pair AlN/Al <sub>0.23</sub> Ga <sub>0.77</sub> N DBR and a 9-pair SiO <sub>2</sub> /HfO <sub>2</sub> DBR. RT PL spectra from a half cavity.....	69
Fig 3.8. Reflectivity and PL spectra from the full hybrid microcavity.....	70
Fig 3.9. (a) Schematic of experimental setups for measuring reflectance. (b) Practical setup for the angle-resolved reflectivity.....	70
Fig 3.10. Schematic of the calculation for interface matrix and propagation matrix..	71
Fig 3.11. Schematic for multilayer structure for transfer matrix.....	72
Fig 3.12. Comparison between reflectivity of pure cavity mode and the polariton mode.....	72

Fig 3.13. Angle-resolved reflectivity spectra ranging from $8^\circ$ to $40^\circ$ for detunings of (a) $-93$ meV and (b) $-53$ meV.....	73
Fig 3.14. Experimental and theoretical polariton dispersion curves.....	73
Fig 3.15. (a) The color map of the measured angle-solved reflectivity spectra. (b) The color map of the calculated angle-solved reflectivity spectra without taking the resonant exciton into account. (c) The color map of the calculated angle-solved reflectivity spectra with taking the resonant exciton into account.....	74
Fig 3.16. Experimental and simulated absorption spectra of a bulk ZnO.....	75
Fig 3.17. (a) Color map of the angular dispersion of measured reflectivity spectra (b) Color maps of the calculated angle-resolved reflectivity spectra with taking the resonant exciton into account. (c) Simulation of angle-resolved reflectivity spectra for the bulk ZnO MCs after taking the absorption of scattering states into account.....	76
Fig 3.18. (a) Schematic diagram of the bulk semiconductor microcavity. (b) Refractive index profile and the optical-field intensity.....	77
Fig 3.19. Color maps of calculated reflectivity spectra as a function of active layer thickness for GaAs, GaN, and ZnO microcavities.....	77
Fig 3.20. Color maps of calculated reflectivity spectra as a function of exciton-photon detuning for GaAs, GaN, and ZnO MCs.....	78
Fig 3.21. (a) Calculated reflectivity spectra for the $\lambda$ ZnO cavity as varying the inhomogeneous broadening. (b) Color map of the reflectivity spectra as a function of inhomogeneous broadening.....	79
Fig 3.22. Color maps of the calculated angle-resolved reflectivity spectra of $0.5\text{-}\lambda$ (a) MQW ZnO-based MC, (b) bulk ZnO-based MC.....	79
Fig 4.1. The schematic diagram of completed electrical pumped InGaN-based microcavity.....	92
Fig 4.2. The schematic of low-temperature electroluminescence.....	92
Fig 4.3. (a) Series of electroluminescence spectra from polariton emission for different temperatures between 180K and 300K. (b) Color map of electroluminescence spectra from polariton emission for different temperatures between 180K and 300K. (c) Simulation of	

temperature-dependent transmittance spectra from 180K to 300 K (d) Color map of transmittance spectra ranging from 180K to 300K.....93

Fig 4.4. (a)Summarizes the angle-resolved emission spectra measured ranging from  $0^\circ$  to  $13^\circ$  at 180k. (b) Color map of the angle-resolved emission spectra measured ranging from  $0^\circ$  to  $13^\circ$  at 180k. (c) Simulation results for angle-resolved transmittance spectra (d) Color map of simulated angle-resolved transmittance spectra.....94

Fig 4.5. Electroluminescence spectra are shown as a function of injection current.95



## Chapter 1. Introduction

### 1.1. Semiconductor microcavity

Semiconductors are important materials in light–matter physics thanks to the radiative recombination of electrons and holes, although not at equilibrium where their densities are too small to produce a detectable quantity of light even with high doping. However, it is easy to operate a semiconductor out of equilibrium by applying an electric voltage to it and generating huge populations of carriers. Indeed, a forward biased p-n gallium arsenide junction generates strong light in the infrared as reported in the early 1960s by Hall *et al.* [1], Nathan *et al.*[2] and Quist *et al.*[3]. By increasing the pumping of the structure to the point where electrons and holes undergo an inversion of population, the diode reaches the stage where gain overcomes losses through stimulated emission, and an input signal on the active region is amplified. It remains to engineer the device so that this input is levied from its output to trigger the laser oscillations. When the light generated by recombination of electrons and holes gets to this surface, it is partially reflected back by internal reflection. The reflectivity is consequently quite low for such lasers, about 30% (the facets can be coated for better reflection).

For semiconductor laser, these preliminary diode sources were not efficient lasers as the active region where electron and hole recombine is spread out across the junction with great losses and requiring significant threshold currents to compensate. A solution was envisioned on how to constrain carriers effectively, theoretically by

Kroemer [4]: the double heterostructure (DH). It consists of a thin region of semiconductor with a small energy gap sandwiched between two oppositely doped semiconductors with a wider bandgap. When forward biased, carriers flow into the active region and recombine more efficiently because the potential barriers of the heterostructure confine the carriers to the active region. Practical and soon efficient operation was achieved and the device became one key element in the computer and information era, with maybe its most significant impact in the data storage with optical reading of CD and DVD types of optical disks.

These above-mentioned structures that are now called classical heterostructures rely on the profile of the energy bands for providing potential traps for the carriers. Their size varies in the range between a few hundred  $\mu\text{m}$  and a few mm. The idea was pushed forward by reducing further still the area of localization to the point where size-quantization plays a role, opening the way to quantum heterostructures, quantum wells, quantum wires and quantum dots. These various schemes of lasing with semiconductors are sketched in [Fig. 1.1](#).

Until the late 1970s, semiconductor lasers exclusively used the stripe geometry with cavity lengths longer than  $100\ \mu\text{m}$ . However, with the production of high-quality integrated DBR mirrors, it became possible to rotate the orientation of the emission so that it emerged normal to the growth-layer planes. The principal advantage of this surface emission geometry of vertical-cavity surface-emitting Lasers (VCSELs) is the ability to make and test large numbers of lasers on a single wafer without having to



cleave the wafer into individual lasers with facets, with a large reduction in the cost of quality control, manufacture and ease of packaging devices. With the introduction of lattice-matched DBR designs producing 99% to 99.9% intensity reflection coefficients, the VCSEL dimension can be reduce to about micrometre –sized.

A microcavity is an optical resonator close to, or below the dimension of the wavelength of light. Micrometre- and submicrometre-sized resonators use two different approaches to confine light, and the most common microcavity is the planar microcavity in which two flat mirrors are brought into close proximity so that only a few wavelengths of light can fit in between them such as VCSEL. Generally, planar microcavities use two different schemes to confine light. In the first, reflection off a single interface is used, such as a metallic surface, or total internal reflection at the boundary between two dielectrics. The second scheme is to use microstructures periodically patterned on the scale of the resonant optical wavelength, for instance a planar multilayer Bragg reflector with high reflectivity, or a photonic crystal. Since confinement by reflection is sometimes required in all three spatial directions, combinations of these approaches can be used within the same microcavity. To confine light laterally within these layers, a curved mirror or lens can be incorporated to focus the light, or they can be patterned into mesas.

Microcavities provide the gain is large enough to make up for the cavity losses. Because of the short round-trip length, the conditions on the reflectivity of the cavity walls are severe. However, these cavities are now the structure of choice (in the form

of VCSELs), due to their ease of integrable manufacture and their performance. Small cavity volumes are also advantageous for producing low threshold lasers as the condition for inversion can be reached by pumping fewer electronic states. On the other hand the total power produced from a microcavity is in general restricted as eventually the high power density causes problems of thermal loading, extra electronic scattering, and saturation. One advantage of a microcavity laser is the reduced number of optical modes into which spontaneous emission is directed, thus increasing the probability of spontaneous emission in a particular mode and thus reducing the lasing threshold.

## **1.2. Strong coupling regime in planar microcavity**

The optical properties of semiconductors and semiconductor structures have been the subject of intense experimental and theoretical investigation during recent decades. Consequently, many of the basic physical properties are understood very well and even used in commercial devices such as semiconductor lasers. When a quantum well grown in the center of a planar microcavity exhibits a pronounced exciton resonance and if the widths of the degenerate exciton and pure-cavity lines are both small enough, one sees two transmission peaks and two reflection dips [5]. This result of light-matter interaction is called here excitonic normal-mode coupling. In other words, If the rate of energy exchange between the cavity field and the excitons becomes much faster than the decay and decoherence rates of both the cavity photons and the excitons, an excitation in the system is stored in the combined system of

photon and exciton, which shows the light-matter strong coupling regime. In the strong coupling regime, it is often related to vacuum-field Rabi splitting of atoms or to a polariton describing light-propagation in a dielectric medium.

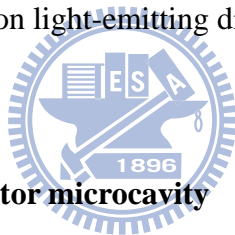
For atoms in a high-finesse cavity one finds a sinusoidal cycling of energy between the atom and the cavity field, which shows the reversible energy transition between atom and photon which causing the vacuum-field Rabi splitting. The study of vacuum-field Rabi splitting has been an exciting subfield of atomic physics. Thompson et al. demonstrate Rabi splitting with a single atom. This led recently to the first clear demonstration of the discrete nature of the coherent exchange of energy between the atom and the quantized electromagnetic field [6]. For such a truly quantum system the optical properties are changed by the addition of a single photon or single atom, which is often referred to as the quantum statistical limit. In the opposite limit of many atoms the system behaves semiclassically, i.e., the light-matter interaction can be described equally well on the basis of a classical field. Interestingly enough basically the same structures show very interesting light-matter coupling effects even under low excitation conditions, where the excitonic resonances dominate the optical semiconductor properties.

Many of the early experimental studies in quantum well structures were done in samples having linewidths of several meV. In the late 1980s great progress was made both in the growth of high-finesse monolithic semiconductor microcavities that spawned VCSEL's and in narrower-linewidth quantum wells. At low temperatures a

modern quantum well sample can have a narrow linewidth of less than one meV. This results in very pronounced index changes in the vicinity of the exciton resonance so that the Fabry-Pérot resonance condition, requiring an integral number of wavelengths between the two mirrors, can be satisfied at three different frequencies. In strong coupling regime, the high absorption at line center destroys the transmission at the central frequency Fabry-Pérot solution. That leaves the two sideband solutions giving the characteristic strong coupling two peaked transmission spectrum first observed by Weisbuch *et al.* in the GaAs/GaAlAs multi quantum well microcavity.

Planar semiconductor MCs in the strong coupling regime have attracted a good deal of attention owing to their potential to enhance and control the interaction between the light field with a single resonance of an infinite medium leads to a new quasi-particle termed cavity-polariton will be created and characterized by bosonic properties, very small effective mass, as well as controllable dispersion curves. The control of the aforementioned interaction is expected to lead to the realization of coherent optical sources such as polariton lasers, which are based on Bose-Einstein condensation or more strictly non-equilibrium polariton population, due to the collective interaction of cavity polaritons with photon modes. In contrast to bulk polaritons, the cavity polaritons have a quasi two-dimensional nature with a finite energy at zero wave vector,  $k=0$ , and is characterized by a very small in-plane effective mass. These characteristics lead to bosonic effects in MCs that cannot be achieved in bulk materials. This can potentially pave the way to ultra low threshold

polariton lasers. This feature is markedly different from those governing conventional lasers. Lasing in conventional lasers that we discussed above is predicated upon population inversion which requires substantial pumping injection. In a microcavity system involving polaritons, however, the lasing condition uniquely depends only on the lifetime of the lower polariton ground state. This is expected to lead to extremely low threshold lasers, even when compared to VCSELs. Through these unique properties of MC polaritons, the investigation on fundamental physical phenomena and advanced optoelectronic devices are reported in recent years, such as Bose Einstein condensates [7, 8], parametric amplifications [9], solid state cavity quantum electrodynamics [10], and polariton light-emitting diodes [11].



### **1.3. Wide bandgap semiconductor microcavity**

Since the first observation of the vacuum Rabi splitting in GaAs-based QW-MCs, the strong coupling of light with excitons in semiconductor MCs has attracted a good deal of interest for fundamental studies of exciton-polariton BEC in solid state as well as promising applications such as very low threshold vertical cavity lasers. So far, however, cavity polariton and BEC based on GaAs based MCs are observable only at very low temperatures because of the slow relaxation of cavity polariton due to the bottleneck effect. Furthermore, the critical temperature  $T_c$  of the bosonic phase transition for cavity polaritons is not limited by the effective mass but rather by the stability of these quasiparticles against temperature and carrier density

and by the value of the so-called Rabi splitting proportional to light-matter interaction strength. This  $T_c$  is of the order of a few tens of kelvins in GaAs-based structures and about 100–200 K in CdTe microcavities. In this respect, GaAs-based polariton LED [12] and electroluminescence from polariton state in the strong coupling regime [13] were reported. Yet, these experiments were conducted in the 4 – 10 K temperature range, and of course with the limitation imposed by low temperatures

It is only natural then wide-bandgap semiconductor based MCs such as GaN and ZnO came to attract increasing attention for RT polariton devices, such as polariton lasers, polariton LEDs, and polariton parametric amplifiers. This potential is due to the large exciton binding energies and oscillator strengths accorded to large bandgap semiconductors. The GaN technology is now reasonably well developed and it should come as no surprise that the strong coupling regime in GaN MCs has been observed by a number of research groups [14-16]. In principle, ZnO is even more attractive as it has a much larger exciton binding energy of 60 meV [17] as compared to 26 meV for GaN [18].

Wide bandgap semiconductor optical emitters have experienced tremendous progress and are now commercially available in the form of blue-violet GaN based edge emitting laser diodes (LDs) [19] and light emitting diodes (LEDs) which are sufficiently bright that general lighting applications, dubbed solid state lighting (SSL), are being pursued vigorously. With high efficiency LEDs for illumination are of industrial pursuit, a part of the focus has now shifted towards other types of emitters

with certain inherent advantages such as resonant cavity LEDs (RCLEDs) and VCSELs. Owing to significant efforts and ensuing continual advances in GaN technology, optically [20-23] and electrically [24] pumped GaN-based VCSELs have been reported at room temperature (RT). The study on GaN-based VCSELs is now poised to enter a new era wherein the threshold current, optical power emitted, efficiency and longevity will be drawing more attention. Beyond the standard VCSEL mentioned above, another type of laser, polariton laser is very attractive owing to its nearly threshold-less operation through Bose-Einstein condensation using cavity polaritons whose genesis lies in the interaction between photons and excitons.

Furthermore, ZnO is the other attractive wide band-gap material for the polariton laser device. ZnO is a II-VI semiconductor with a direct band gap around 3.3 eV, a large exciton binding energy of 60 meV, and extremely high exciton oscillator strength. In 2002 [25], it was suggested that these properties are ideal in order to fabricate a new type of coherent light emitter called polariton laser [26] which would emit light in the blue-UV range. Such laser would have a large technological interest, since there is, so far, no demonstration of VCSEL working in the UV frequency range. In parallel, the progress in ZnO technology [27] has made realistic a polariton laser based on this material. The strong coupling regime has been reported by several groups, [28-30] which have confirmed that (close of 100 meV) twice that of the best GaN samples could be achieved. Also some alternative systems to planar microcavities based on ZnO technology, such as micropillars or microdisks, have

allowed the observation of the strong coupling regime at RT [31].

Therefore, wide bandgap semiconductors such as GaN and ZnO are candidates for achieving low threshold, ideally threshold-less polariton lasing at RT, owing to large exciton binding energies and extremely high light-matter interaction constant in these materials systems. Recently, RT polariton lasing has been observed in a bulk-GaN MC [32] and multi quantum well (MQW) MC [33]. Since the study of polariton induced nonlinear phenomena is in its early stages, electrically injected polariton lasers are awaiting further development. However, the optically pumped experiments, which have been successful, form the stepping stone for electrical injection. Low-threshold UV polariton lasers should be of great technological interest as potential components for optical communications and data storage.





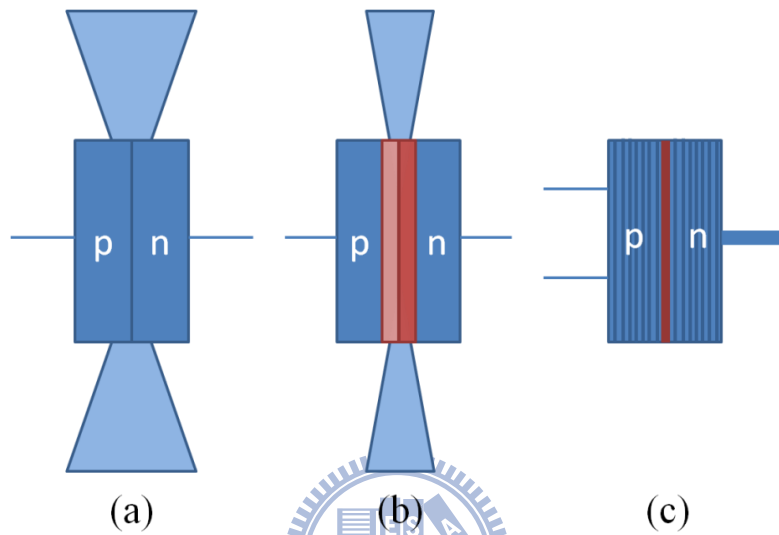


Fig 1.1 Various schemes of lasing with semiconductors (a) the p-n junction where electron-hole recombination at the interface serve as the active population, (b) the edge-emitting laser where the active region is confined by a heterostructure and (c) the VCSEL where localization is pushed to the quantum limit and emission made from the surface.

## Chapter 2. Microcavity polaritons

### 2.1 Strong coupling regime and weak coupling regime

The quantum treatment between light and atoms is usually developed in terms of the two-level atom approximation [34]. This approximation is applicable when the frequency of the light coincides with one of the optical transitions of the atom. The atom will have many quantum levels, and there will be many possible optical transitions between them. However, in the two-level atom approximation we only consider the specific transition that satisfies eq.(2.1-1) and ignore all the other levels. It is customary to label the lower and upper levels as 1 and 2, respectively.

$$\hbar\omega = E_2 - E_1 \quad (2.1-1)$$

Our objective is to solve the time-dependent Schrödinger equation for a two-level atom in the presence of the light. In other words, we must solve:

$$\hat{H}\Psi = i\hbar \frac{\partial \Psi}{\partial t} \quad (2.1-2)$$

We start by splitting the Hamiltonian into a time-independent part  $\hat{H}_0$  which describes the atom in the dark, and a perturbation term  $\hat{V}(t)$  which accounts for the light-atom interaction:

$$\hat{H} = \hat{H}_0(r) + \hat{V}(t) \quad (2.1-3)$$

In the case of a two-level atom, the general solution to the time-dependent Schrödinger equation reduces to

$$\Psi(r,t) = c_1(t)\psi_1(r)e^{-iE_1t/\hbar} + c_2(t)\psi_2(r)e^{-iE_2t/\hbar} \quad (2.1-4)$$

On substituting this wave function into eq.(2.1-2) with  $\hat{H}_0$  given by eq.(2.1-3),

we obtain:

$$c_1'(t) = -\frac{i}{\hbar}(c_1(t)V_{11} + c_2(t)V_{12}e^{-i\omega_0 t}) \quad (2.1-5)$$

$$c_2'(t) = -\frac{i}{\hbar}(c_1(t)V_{21}e^{i\omega_0 t} + c_2(t)V_{22}) \quad (2.1-6)$$

Where

$$V_{ij} \equiv \langle i | \hat{V}(t) | j \rangle = \int \psi_i^* \hat{V}(t) \psi_j d^3 r \quad (2.1-7)$$

To proceed further we must consider the explicit form of the perturbation  $\hat{V}(t)$ .

In the semi-classical approach, the light-atom interaction is given by the energy shift of the atomic dipole in the electric field of the light, and we arbitrarily choose the x-axis as the direction of the polarization so that we can write

$$\hat{V}(t) = exE_0 \cos \omega t = \frac{exE_0}{2}(e^{i\omega t} + e^{-i\omega t}) \quad (2.1-8)$$

where  $E_0$  is the amplitude of the light wave and the perturbation matrix elements are given by:

$$V_{ij} = -\frac{E_0}{2}(e^{i\omega t} + e^{-i\omega t})u_{ij} \quad (2.1-9)$$

where  $u_{ij}$  is the dipole matrix element given by

$$u_{ij} \equiv \int \psi_i^* x \psi_j d^3 r = -e \langle i | x | j \rangle \quad (2.1-10)$$

Since  $x$  is an odd parity operator and atomic states have either even or odd parities, it must be the case that  $u_{11} = u_{22} = 0$ . Moreover, the dipole matrix element represents a measurable quantity and must be real, which implies that  $u_{21} = u_{12}$ , because  $u_{21} = u_{12}^*$ . With these simplifications, eq.(2.1-5) and eq.(2.1-6) reduce to:

$$c_1'(t) = \frac{i}{2} \Omega_R (e^{i(\omega-\omega_0)t} + e^{-i(\omega+\omega_0)t}) c_2(t) \quad (2.1-11)$$

$$c_2'(t) = \frac{i}{2} \Omega_R (e^{-i(\omega-\omega_0)t} + e^{i(\omega+\omega_0)t}) c_1(t) \quad (2.1-12)$$

where we define the Rabi frequency  $\Omega_R = |u_{12} E_0 / \hbar|$

These are the equations that we must solve to understand the behavior of the atom in the light field. It turns out that there are two distinct types of solution that can be found, which correspond to the weak-field limit and the strong-field limit respectively.

We consider the weak-field limit first. The weak-field limit applies to low-intensity light sources. We assume that the atom is initially in the lower level and that the lamp is turned on at  $t = 0$ . This implies that  $c_1(0) = 1$  and  $c_2(0) = 0$ . With a low-intensity source, the electric field amplitude will be small and the perturbation weak. The number of transitions expected is therefore small, and it will always be the case that  $c_1(t) \gg c_2(t)$ . In these conditions we can put  $c_1(t) = 1$  for all  $t$ , so that eq. (2.1-14) reduces to

$$c_1'(t) = 0 \quad (2.1-13)$$

$$c_2'(t) = \frac{i}{2} \Omega_R (e^{-i(\omega-\omega_0)t} + e^{i(\omega+\omega_0)t}) c_1(t) \quad (2.1-14)$$

According to the rotating wave approximation, we now neglect the second term in eq.(2.1-14). This is justified by the fact that since  $\delta\omega \ll (\omega + \omega_0)$ , the second term is much smaller than the first. After some manipulation we find:

$$|c_2(t)|^2 = \left(\frac{\Omega_R}{2}\right)^2 \left(\frac{\sin \delta\omega t / 2}{\delta\omega / 2}\right)^2 \quad (2.1-15)$$

We know in fact that all spectral lines have a finite width  $\Delta\omega$ . Furthermore, we are considering the interaction between the atom and a broad-band source such as a black-body lamp. Such a broad-band source can be specified by the spectral energy density  $u(\omega)$ , which must satisfy:

$$\frac{1}{2} \varepsilon_0 E_o^2 = \int u(\omega) d\omega \quad (2.1-16)$$

We therefore integrate eq.(2.1-16) the spectral line:

$$|c_2(t)|^2 = \left( \frac{u_{12}^2}{2\varepsilon_0 \hbar^2} \right)^2 \int_{\omega_0 - \Delta\omega/2}^{\omega_0 + \Delta\omega/2} \left( \frac{\sin(\omega - \omega_0)t/2}{(\omega - \omega_0)/2} \right)^2 u(\omega) d\omega \quad (2.1-17)$$

We now make the approximation that the spectral line is sharp compared to the broad-band spectrum of the lamp, so that  $u(\omega)$  does not vary significantly within the integral. This allows us to replace  $u(\omega)$  by a constant value  $u(\omega_0)$ , and thus to evaluate the integral. The limiting value for  $t \Delta \omega \rightarrow \infty$  is  $u(\omega_0) 2\pi t$ . Hence we finally obtain:

$$|c_2(t)|^2 = \frac{\pi}{\varepsilon_0 \hbar^2} u_{12}^2 u(\omega_0) t \quad (2.1-18)$$

which is a much more satisfactory result because it implies that the probability that the atom is in the upper level increases linearly with time.

We now wish to return to the more general case in which the population of the upper level is significant. It is intuitively obvious that this condition applies when the light-atom interaction is strong. In other words, we are dealing with the case of strong electric fields, such as those found in powerful laser beams. In order to find a solution to eq.(2.1-12) in the strong-field limit we make two simplifications. First, we apply the rotating wave approximation to neglect the terms that oscillate at  $\pm(\omega + \omega_0)$ , as in

the previous section. Second, we only consider the case of exact resonance with  $\delta\omega = 0$ . With these simplifications, eq.(2.1-11) reduces to:

$$c_1'(t) = \frac{i}{2}\Omega_R c_2(t) \quad (2.1-19)$$

$$c_2'(t) = \frac{i}{2}\Omega_R c_1(t) \quad (2.1-20)$$

If the particle is in the lower level at  $t = 0$  so that  $c_1(0) = 1$  and  $c_2(0) = 0$ , the solution is:

$$c_1(t) = \cos(\Omega_R t / 2) \quad (2.1-21)$$

$$c_2(t) = i \sin(\Omega_R t / 2) \quad (2.1-22)$$

The probabilities for finding the electron in the upper or lower levels are then given by:

$$|c_1(t)|^2 = \cos^2(\Omega_R t / 2) \quad (2.1-23)$$

$$|c_2(t)|^2 = \sin^2(\Omega_R t / 2) \quad (2.1-24)$$

The time dependence of these probabilities is shown in Fig. 2.1. At  $t = \pi/\Omega_R$  the electron is in the upper level, whereas at  $t = 2\pi/\Omega_R$  it is back in the lower level. The process then repeats itself with a period equal to  $2\pi/\Omega_R$ . The electron thus oscillates back and forth between the lower and upper levels at a frequency equal to  $\Omega_R/2\pi$ . This oscillatory behavior in response to the strong-field is called Rabi oscillation or Rabi flopping. When the light is not exactly resonant with the transition, it can be shown that the second line of eq.(2.1-24) is modified to

$$|c_2(t)|^2 = \frac{\Omega_R^2}{\Omega^2} \sin^2(\Omega_R t / 2) \quad (2.1-25)$$

Where  $\Omega^2 = \Omega_R^2 + \delta\omega^2$ ,  $\delta\omega$  being the detuning. This shows that the frequency of the Rabi oscillations increases but their amplitude decreases as the light is tuned away from resonance.

At low powers, the oscillation period is longer than the radiative lifetime, and we would expect random spontaneous emission events to destroy the coherence of the superposition states, and hence curtail the oscillations. We thus have to work at higher powers to shorten the Rabi flopping period, which can be difficult to achieve in practice. The damping processes for coherent phenomena such as Rabi flopping are traditionally characterized by two time constants,  $T_1$  and  $T_2$ . These two types of damping are sometimes called longitudinal relaxation and transverse relaxation, respectively. In physical terms,  $T_1$  damping is essentially determined by population decay, whereas  $T_2$  damping is related to dephasing processes.

Having considered the processes that cause dephasing in quantum systems, we can now study the detailed effects of damping on Rabi oscillations. It can be shown that if the damping rate is  $\gamma$ , the probability that the electron is in the upper level, namely  $|c_2(t)|^2$ , is given by:

$$|c_2(t)|^2 = \frac{1}{2(1+1+2\xi^2)} \left[ 1 - \left( \cos \Omega' t + \frac{3\xi}{(4-\xi^2)^{1/2}} \sin \Omega' t \right) \exp\left(\frac{-3\gamma t}{2}\right) \right] \quad (2.1-25)$$

Where

$$\xi = \gamma / \Omega_R$$

$$\Omega' = \Omega_R \sqrt{1 - \xi^2 / 4}$$

Fig 2.2 shows graphs of  $|c_2(t)|^2$  from eq.(2.1-25) for three different values of the damping constant. The dotted line shows the undamped case with  $\gamma = 0$ . The two other graphs correspond to light damping ( $\gamma/\Omega_R = 0.1$ ) and strong damping ( $\gamma/\Omega_R = 1$ ), respectively. Let us consider the case of light damping first. The electron performs a few damped oscillations and then approaches the asymptotic limit with  $|c_1|^2 = |c_2|^2 = 1/2$ . This asymptotic limit is exactly the behavior we would have expected from the Einstein analysis of a pure two-level system in the strong-field limit. At high optical power levels the spontaneous emission rate is negligible and the rates of stimulated emission and absorption eventually equal out, leading to identical upper and lower level populations.



Now consider the behavior for strong damping. This is effectively equivalent to the weak-field limit, because we can always make  $\gamma/\Omega_R$  large by turning down the electric field of the light beam. (See eq. (2.1-25)) No oscillations are observed, and the asymptotic value of  $|c_2|^2$  for very large damping rates (i.e.  $\xi \gg 1$ ) is given by:

$$|c_2(t)| \rightarrow \frac{\xi^{-2}}{4} = \frac{\Omega_R^2}{4\gamma^2} \quad (2.1-25)$$

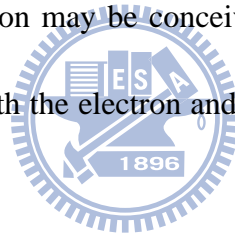
This simple discussion shows how the inclusion of damping allows us to understand the evolution of the behavior as the electric field strength is increased. At low fields, we are in the strongly damped regime where there are discrete transitions and the Einstein analysis is valid. As the field is increased, the ratio of the damping rate to the Rabi frequency decreases, and we can eventually reach the case where the oscillations are observable.



## 2.2 What are microcavity polaritons

### 2.2.1 Wannier-Mott exciton

The absorption of a photon by interband transition in a semiconductor or insulator creates an electron in the conduction band and a hole in the valence band. The oppositely charged particles are created at the same point in space and can attract each other through their mutual Coulomb interaction. This attractive interaction increases the probability of the formation of an electron-hole pair, and therefore increases the optical transition rate. Moreover, if the right condition is satisfied, a bound electron-hole pair can be formed. This neutral bound pair is called an exciton. In the simplest picture, the exciton may be conceived as a small hydrogenic system similar to a positronium atom with the electron and hole in a stable orbit around each other.



Excitons are observed in many crystalline materials. There are two basic types<sup>[35]</sup> :

- (a) Wannier-Mott excitons, also called free excitons
- (b) Frenkel excitons, also called tightly bound excitons

The Wannier-Mott excitons are mainly observed in semiconductors, while the Frenkel excitons are found in insulator crystals and molecular crystals. In our study, we focus on the Wannier-Mott excitons having a large radius that encompasses many atoms, and they are delocalized states that can move freely throughout the crystal; hence the alternative name of “free” excitons.

In a free exciton, the average separation of the electrons and holes is much greater than the atomic spacing, as shown in Fig 2.3. This is effectively the definition of a Wannier exciton, and it specifies more accurately what is meant by saying that the free exciton is weakly bound electron-hole pair. Since the electron-hole pair separation is so large, it is a good approximation to average over the detailed structure of the atoms in between the electron and hole and to consider the particles to be moving in a uniform dielectric material. We can then model the free exciton as a hydrogenic system similar to positronium.

We know from atomic physics that the motion of hydrogenic atoms splits into the centre of mass motion and the relative motion. The centre of mass motion describes the kinetic energy of the atom as a whole, while the relative motion determines the internal structure. The energies of the bound states can be determined by finding the eigenvalues of the Schrödinger equation for the relative motion. The main results are well explained by using the Bohr model and this is the procedure we will adopt here.

In applying the Bohr model to the exciton, we must take account of the fact that the electron and hole are moving through a medium with a high dielectric constant  $\epsilon_r$ .

We must also remember that the reduced mass  $\mu$  will be given by eq(2.2-1).

$$\frac{1}{\mu} = \frac{1}{m_e^*} + \frac{1}{m_h^*} \quad (2.2-1)$$

With these two qualifications, we can then just use the standard results of the Bohr model. The bound states are characterized by the principal quantum number  $n$ .

The energy of the  $n_{th}$  level relative to the ionization limit is given by

$$E(n) = -\frac{\mu}{m_0} \frac{1}{\epsilon_r^2} \frac{R_H}{n^2} = -\frac{R_y}{n^2} \quad (2.2-2)$$

where  $R_H$  is the Rydberg constant of the hydrogen atom (13.6 eV). The quantity  $R_y = (\mu/m_0\epsilon_r^2)R_H$  introduced here is the exciton Rydberg constant. The radius of the electron-hole orbit is given by

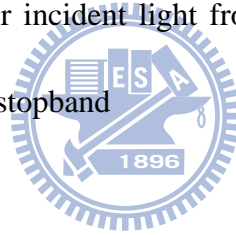
$$r_n = \frac{m_0}{\mu} \epsilon_r n^2 a_H = n^2 a_X \quad (2.2-3)$$

where  $a_H$  is the Bohr radius of the hydrogen atom ( $5.29 \times 10^{-11}$  m) and  $a_X = (m_0\epsilon_r / \mu)a_H$  is the exciton Bohr radius. Equation (2.2-2) and (2.2-3) show that the ground state with  $n=1$  has the largest binding energy and smallest radius. The excited states with  $n>1$  are less strongly bound and have a larger radius.

Stable excitons will only be formed if the attractive potential is sufficient to protect the exciton against collisions with phonons. Since the maximum energy of a thermally excited phonon at temperature  $T$  is about  $k_B T$ , where  $k_B$  is Boltzmann's constant, this condition will be satisfied if the exciton binding energy is greater than  $k_B T$ . Wannier-Mott excitons have small binding energies due to their large radius, with typical values of around 10meV. Since  $k_B T$  is about 25 meV at RT, it is necessary to direct the interest toward wide band-gap semiconductors for large exciton binding energy, such as GaN and ZnO. [Table 2.1](#) lists the exciton Rydberg constant and Bohr radius for number of direct gap III-V and II-VI semiconductors.

### 2.2.2 Semiconductor microcavity cavity mode

A typical structure of a semiconductor microcavity consisting of a cavity layer with  $m \lambda / 2$  ( $m$  is integer) sandwiched between two distributed Bragg reflectors (DBRs). A DBR is made of layers of alternating high and low refraction indices, each layer with an optical thickness of  $\lambda / 4$ . Light reflected from each interface destructively interfere, creating a stop-band for transmission. Hence the DBR acts as a high-reflectance mirror when the wavelength of the incident light is within the stopband. The bottom DBR consists of  $2N$  layers with alternating refraction indices of  $n_1$  and  $n_2$ , the first layer with refraction index ( $n_1$ ) is next to a cavity layer with refraction index ( $n_c$ ), while the last layer with refraction index ( $n_2$ ) is next to the substrate with reflection ( $n_s$ ). For incident light from the cavity side, the maximum reflectivity is at the center of the stopband



$$R_{\max}^{2N} = \left( \frac{1 - \frac{n_c}{n_s} \left(\frac{n_2}{n_1}\right)^{2N}}{1 + \frac{n_c}{n_s} \left(\frac{n_2}{n_1}\right)^{2N}} \right)^2 \quad (2.2-4)$$

If the DBR has  $N + 1$  layers with refraction index  $n_1$  and  $N$  layers with  $n_2$ , such as the top DBR,

$$R_{\max}^{2N} = \left( \frac{1 - \frac{n_c}{n_1} \frac{n_t}{n_1} \left(\frac{n_2}{n_1}\right)^{2N}}{1 + \frac{n_c}{n_1} \frac{n_t}{n_1} \left(\frac{n_2}{n_1}\right)^{2N}} \right)^2 \quad (2.2-5)$$

where  $R_{\max}$  always increases with  $N$  and increases with the refraction index contrast of the pair. Shown in [Fig 2.4](#) are the reflection spectra of a typical DBR.

When two such high-reflectance DBRs are attached to a layer with an optical

thickness integer times of  $\lambda_c/2$ , a cavity resonance is formed at  $\lambda_c$ , leading to a sharp increase of the transmission T at  $\lambda_c$ :

$$T = \frac{(1-R_1)(1-R_2)}{\left[1 - \sqrt{R_1 R_2}\right]^2 + 4\sqrt{R_1 R_2} \sin^2(\phi/2)} \quad (2.2-6)$$

where  $\phi$  is the cavity round-trip phase shift of a photon at  $\lambda_c$ .

One characteristic parameter of the cavity quality

$$Q \approx \frac{\lambda_c}{\Delta\lambda_c} \cong \frac{\pi(R_1 R_2)^{1/4}}{1 - (R_1 R_2)^{1/2}} \quad (2.2-7)$$

Q is the average number of round trips a photon travels inside the cavity before it escapes. Fig 2.5 gives an example of the reflection spectrum of a cavity with Q ~4000.

Yet unlike in a metallic cavity, the field penetration depth into the DBRs is much larger. So effective cavity length is extended in a semiconductor microcavity as:

$$L_{eff} = L_c + L_{DBR} \quad (2.2-8)$$

$$L_{DBR} \approx \frac{\lambda_c}{2n_c} \frac{n_1 n_2}{|n_1 - n_2|} \quad (2.2-9)$$

The planar DBR-cavity confines the photon field in the z-direction but not in plane, incident light from a slant angle  $\mu$  relative to the z-axis has a resonance at  $\lambda_c / \cos\theta$ . As a result, the cavity has an energy dispersion versus the inplane wavenumber  $k_{//}$ :

$$E_{cav} = \frac{\hbar c}{n_c} \sqrt{k_{\perp}^2 + k_{//}^2} \quad (2.2-10)$$

where  $k_{\perp} = n_c \frac{2\pi}{\lambda_c}$ . And there is a one-to-one correspondence between the incidence

angle  $\theta$  and each resonance mode with inplane wavenumber  $k_{//}$ :

$$k_{//} = n_c \frac{2\pi}{\lambda_c} \tan \left[ \sin^{-1} \left( \frac{\sin \theta}{n_c} \right) \right] \approx \frac{2\pi}{\lambda_c} \theta \quad \text{when } k_{//} \ll k_{\perp} \quad (2.2-11)$$

In the region  $k_{//} \ll k_{\perp}$ , we have:

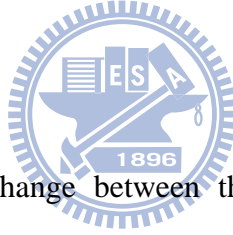
$$E_{cav} \approx \frac{\hbar c}{n_c k_{\perp}} \left( 1 + \frac{k_{//}^2}{2k_{\perp}^2} \right) = E_{cav}(k_{//} = 0) + \frac{\hbar^2 k_{//}^2}{2(2\pi\hbar / \lambda_c c)} = E_{cavo} + \frac{\hbar^2 k_{//}^2}{2m_{cav}} \quad (2.2-12)$$

Thus the cavity photon acquires an effective mass of

$$m_{cav} = \frac{2\pi\hbar}{\lambda_c c} \quad (2.2-13)$$

Fig 2.6 gives a numerical example of the angle-tuning, or energy and inplane wavenumber dispersion of the cavity resonance.

### 2.2.3. Microcavity polaritons



If the rate of energy exchange between the cavity field and the excitons becomes much faster than the decay and decoherence rates of both the cavity photons and the excitons, an excitation in the system is stored in the combined system of photon and exciton. Thus the elementary excitations of the system are no longer exciton *or* photon, but a new type of quasi-particles called the polaritons.

Using the rotating wave approximation, the linear Hamiltonian of the system is written in the second quantization form as: [36]

$$\begin{aligned} \hat{H}_{opl} &= \hat{H}_{opl} + \hat{H}_{exc} + \hat{H}_I \\ &= \sum E_{cav}(k_{//}, k_c) \hat{a}_{k_{//}}^+ \hat{a}_{k_{//}} + \sum E_{exc}(k_{//}) \hat{e}_{k_{//}}^+ \hat{e}_{k_{//}} + \sum \hbar\Omega(\hat{a}_{k_{//}k_c}^+ \hat{e}_{k_{//}} + \hat{a}_{k_{//}} \hat{e}_{k_{//}}^+) \end{aligned} \quad (2.2-14)$$

Here is  $\hat{a}_{k_{//}}^+$  the photon creation operator with inplane wavenumber  $k_{//}$  and longitudinal wavenumber  $k_c = k \cdot \hat{z}$  determined by the cavity resonance.  $\hat{e}_{k_{//}}^+$  is the

exciton creation operators with inplane wavenumber  $k_{//}$ .  $\hbar\Omega$  is the exciton-photon dipole interaction given by the exciton optical transition matrix element, and we used the condition that  $M$  is non-zero only between modes with the same  $k_{//}$ . The above Hamiltonian can be diagonalized by the transformation:

$$\hat{p}_{k_{//}} = X_{k_{//}} \hat{e}_{k_{//}} + C_{k_{//}} \hat{a}_{k_{//}} \quad (2.2-15)$$

$$\hat{q}_{k_{//}} = -C_{k_{//}} \hat{e}_{k_{//}} + X_{k_{//}} \hat{a}_{k_{//}} \quad (2.2-16)$$

And  $\hat{H}_{opt}$  becomes:

$$\hat{H}_{pol} = \sum E_{LP}(k_{//}) \hat{p}_{k_{//}}^{\dagger} \hat{p}_{k_{//}} + \sum E_{UP}(k_{//}) \hat{q}_{k_{//}}^{\dagger} \hat{q}_{k_{//}} \quad (2.2-17)$$

The new operators  $(\hat{p}_{k_{//}}, \hat{p}_{k_{//}}^{\dagger})$  and  $(\hat{q}_{k_{//}}, \hat{q}_{k_{//}}^{\dagger})$  are the new quasi-particles, or, eigenmodes, of the system. They are called the lower (LP) and upper polaritons (UP), corresponding to the lower and upper branches of the eigen energies. A polariton is a linear superposition of an exciton and a photon with the same inplane wavenumber  $k_{//}$ . Since both excitons and photons are bosons, so are the polaritons. The exciton and photon fractions in each lower polariton (and vice versa for upper polaritons) are given by the amplitude squared of  $X_{k_{//}}$  and  $C_{k_{//}}$  which are referred to as the Hopfield coefficients, they satisfy:

$$|X_{k_{//}}|^2 + |C_{k_{//}}|^2 = 1 \quad (2.2-18)$$

Let  $\Delta E(k_{//}) = E_{exc}(k_{//}) - E_{cav}(k_{//}, k_c)$ ,  $X_{k_{//}}$  and  $C_{k_{//}}$  are given by

$$|X_{k_{//}}|^2 = \frac{1}{2} \left( 1 + \frac{\Delta E(k_{//})}{\sqrt{\Delta E(k_{//})^2 + 4\hbar^2 \Omega^2}} \right) \quad (2.2-19)$$

$$|C_{k_{//}}|^2 = \frac{1}{2} \left( 1 - \frac{\Delta E(k_{//})}{\sqrt{\Delta E(k_{//})^2 + 4\hbar^2\Omega^2}} \right) \quad (2.2-20)$$

At  $\Delta E=0$ ,  $|X|^2 = |C|^2 = \frac{1}{2}$ , LP and UP are exactly half photon half exciton, and

the energies of the polaritons, which are the eigenenergies of the Hamiltonian (2.2-17),

are deduced from the diagonalization procedure as:

$$E_{LP,UP}(k_{//}) = \frac{1}{2} [E_{exc} + E_{cav} \pm \sqrt{4\hbar^2\Omega^2 + (E_{exc} - E_{cav})^2}] \quad (2.2-21)$$

When the un-coupled exciton and photon are at resonance,  $E_{exc} = E_{cav}$ , lower and upper polariton energies have the minimum separation  $E_{exc} - E_{cav} = 2\hbar\Omega$ , which is often called the Rabi splitting in analogy to the atomic cavity Rabi splitting. Due to the coupling between the exciton and photon modes, the new polariton energies anti-cross when the cavity energy is tuned across the exciton energy. This is one of the signatures of 'strong coupling' shown in Fig 2.8. When  $|E_{exc} - E_{cav}| \gg \hbar\Omega$ , the polariton energies reduce to the same as photon and exciton energies due to the very large detuning between the two modes, and polariton is no longer a useful concept. So the detuning is assumed to be comparable to or less than the coupling strength in our discussions unless specified.

### 2.3 Microcavity polaritons characteristics

The spin number of bosons is number of integer so that the kind of particle does not necessary to obey the Pauli Exclusion Principle which is much different from the fermions such as electron. Therefore, the bosons can condense at the lowest energy



ingenstate and form the unique physical phenomenon Bose Einstein Condensation. A polariton is a linear superposition of an exciton and a photon with the same inplane wavenumber  $k_{//}$ , and both excitons and photons are bosons, so the polaritons also have the bosonic properties.

Compared to other BEC systems, such as atomic gases and excitons, polaritons have vastly different length, energy and time scales. Beside as an essentially different system of fundamental interest, polaritons also possess many unique advantages for BEC research. First of all, the critical temperature of polariton condensation ranges from a few kelvin to above RT, which is four order of magnitude higher than that of excitons and eight orders of magnitude higher than that of atoms. It originates from the critical temperature is inverse proportional to the particle effective mass.

$$T_C \propto 2\pi\hbar^2 n_c^{-2/d} m^{-1} \quad (2.3-1)$$

The polariton effective mass is the weighted harmonic mean of the mass of its exciton and photon components:

$$\frac{1}{m_{LP}} = \frac{|X|^2}{m_{exc}} + \frac{|C|^2}{m_{cav}} \quad (2.3-2)$$

$$\frac{1}{m_{UP}} = \frac{|C|^2}{m_{exc}} + \frac{|X|^2}{m_{cav}} \quad (2.3-3)$$

where  $X$  and  $C$  are the exciton and photon fractions given by (2.2-19) and (2.2-20).  $m_{exc}$  is effective exciton mass of its center of mass motion, and  $m_{cav}$  is the effective cavity photon masses given by (2.2-12). Since  $m_{cav}$  is much smaller than  $m_{exc}$ ,

$$m_{LP}(k_{//} \sim 0) \cong m_{cav} / |C|^2 \sim 10^{-4} m_{exc} \quad (2.3-4)$$

$$m_{UP}(k_{//} \sim 0) \cong m_{cav} / |X|^2 \quad (2.3-5)$$

The very small effective mass of LPs at  $k_{//} \sim 0$  determines the very high critical temperature of phase transitions for the system. At large  $k_{//} \gg k_{c//}$ ,  $E_{cav}(k_{//}) - E_{exc}(k_{//}) \gg \hbar\Omega$ , dispersions of the LP and UP converge to the exciton and photon dispersions respectively, and LP has an effective mass  $m_{LP}(k_{//} \sim 0) \cong m_{cav} / |C|^2 \sim 10^{-4} m_{exc}$ . Hence the LP's effective mass changes by four order of magnitude from  $k_{//} \sim 0$  to large  $k_{//}$ . Therefore, the polariton effective mass of polaritons is much lighter than atoms and exciton gas due to the mixing with cavity photons, and most notable for the polariton system is its very light effective mass and very short time scale which leads to a critical temperature of phase transitions ranging from 1 Kelvin up to RT.



From the experimental viewpoints, the microcavity polariton is a most accessible system. There exists a one-to-one correspondence between an internal polariton in mode  $k_{//}$  and an external photon with the same energy and inplane-wavenumber, propagating at an angle  $\theta$  from the growth direction. The polariton is coupled to this photon via its the photonic component with a fixed coupling rate (2.2-20). The one-to-one correspondence between the internal polariton mode and the external out-coupled photon mode lends great convenience to experimental access to the system. The external emitted photon field carries directly information of the internal polaritons, such as the energy dispersion, population per

mode, and statistics of the polaritons. It is mainly through the emitted photons that we study the internal polaritons. Furthermore, polaritons are conveniently excited, resonantly or non-resonantly, by optical pumping. The excitation density spans the whole density range of interest. A major enemy against quantum phase transitions in solids is the unavoidable compositional and structural disorders.

Microcavity system of a given composition has two very useful and unique adjustable parameters: the active layer thickness and the cavity-exciton detuning ( $\delta$ ). For example, the active layer thickness changes the exciton-photon coupling strength  $\Omega \propto \sqrt{N_{QW}}$ , where  $N_{QW}$  is the number of quantum wells, When  $\Omega$  is increased to become comparable with the exciton binding energy, the very strong coupling effect further reduces exciton Bohr radius in the LP branch and increases the exciton mott density. The other parameter detuning  $\delta$  is very conveniently changed due to the taper of the cavity thickness across each wafer. It tunes the exciton and photon fractions in the LPs, hence the dispersions, lifetimes, effective mass of the polaritons. This peculiar parameter has important implications in polaritonic properties, especially for energy relaxation dynamics of polaritons. A few examples of the polariton dispersion with different  $\delta$  are given in [Fig 2.9](#)

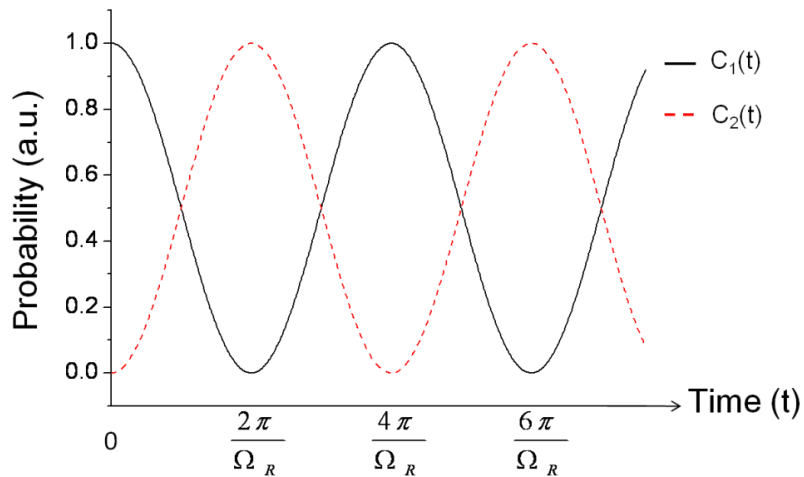


Fig 2.1 Time dependence of these probabilities for finding the electron in either the upper or lower level in the strong-field in the absence of damping. The electron oscillates back and forth between the two levels at the Rabi angular frequency,  $\Omega_R$ . This phenomenon is either called Rabi flopping or Rabi oscillation.

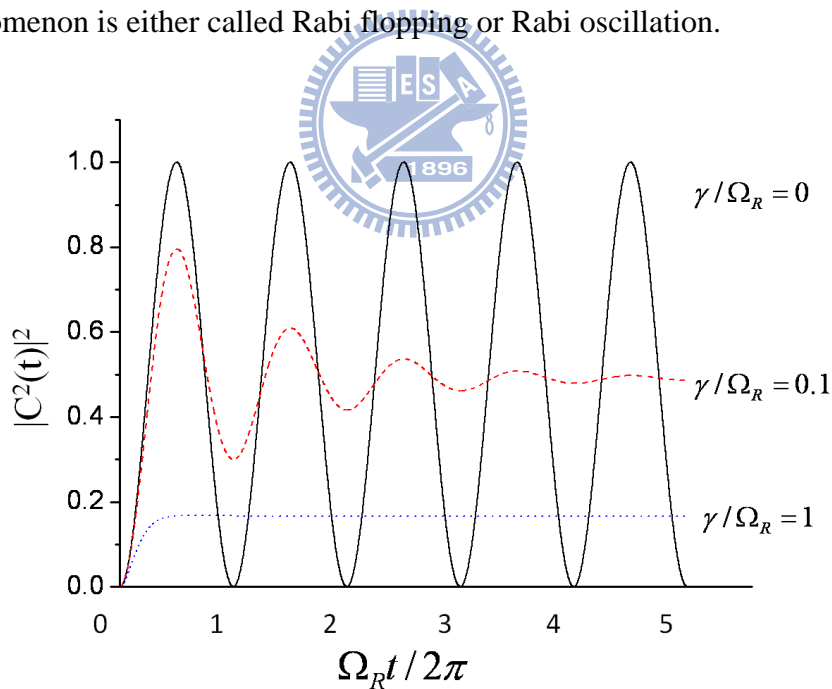


Fig 2.2 Damped Rabi oscillations for two ratio of the damping rate  $\gamma$  to the Rabi oscillation frequency  $\Omega_R$ . The dotted curve shows the oscillations when no damping is present.

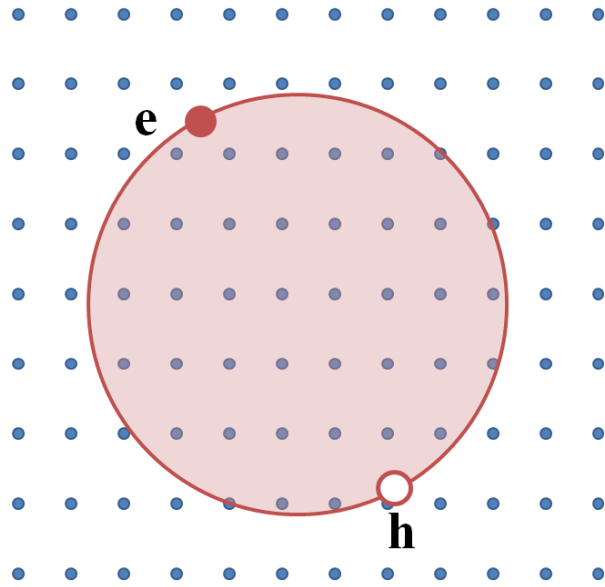


Fig 2.3 Schematic diagram of a free exciton which is called Wannier-Mott excitons

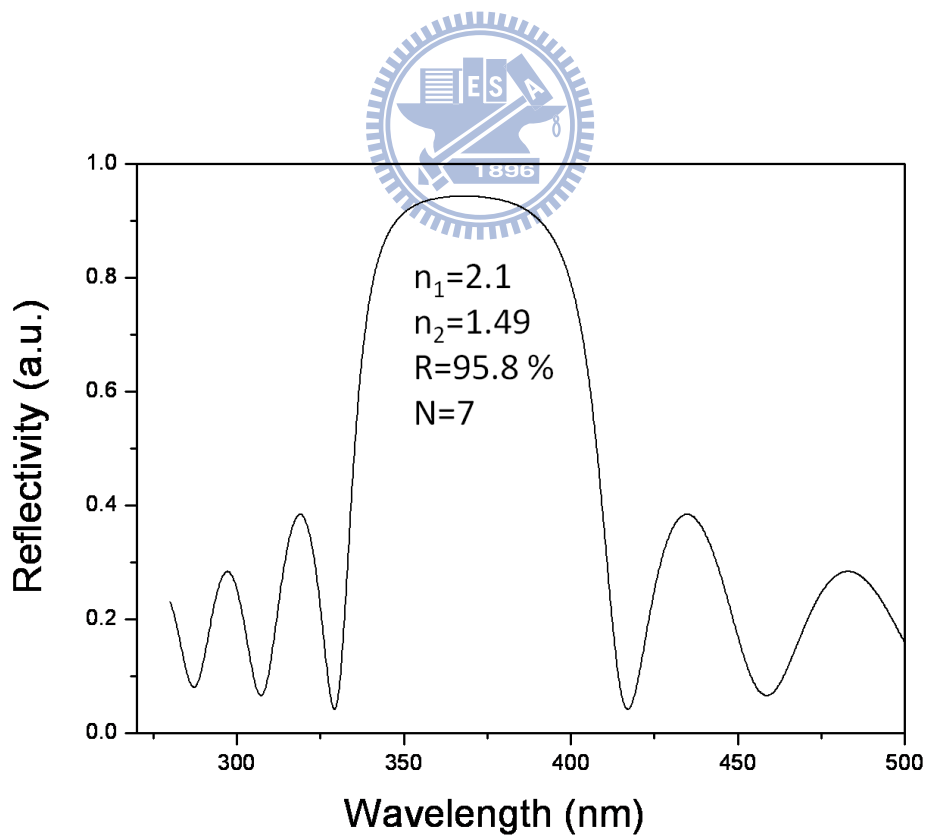


Fig 2.4 Reflectance spectra of typical DBR.

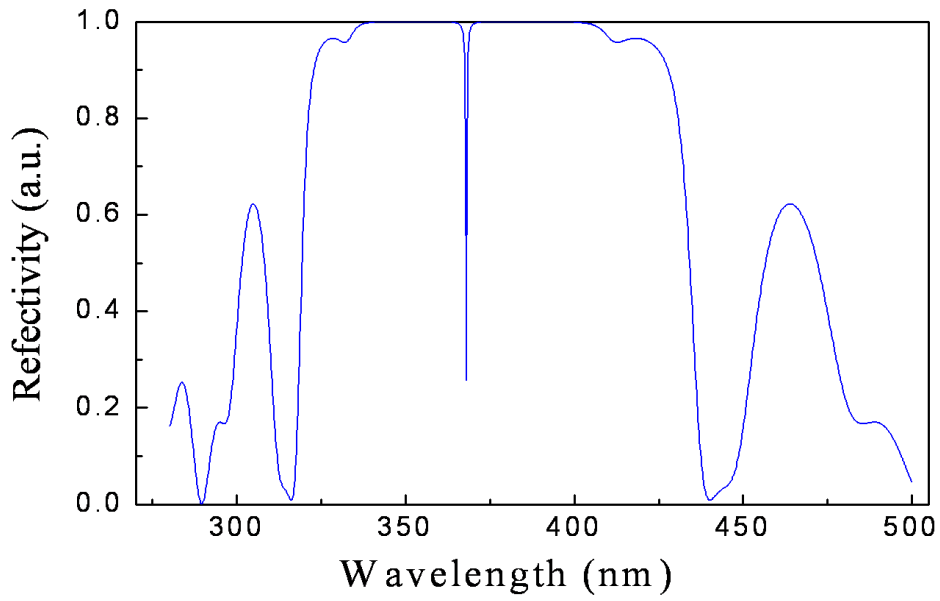


Fig 2.5 Reflectance of an empty,  $\lambda/2$  microcavity with the Q value of 4000

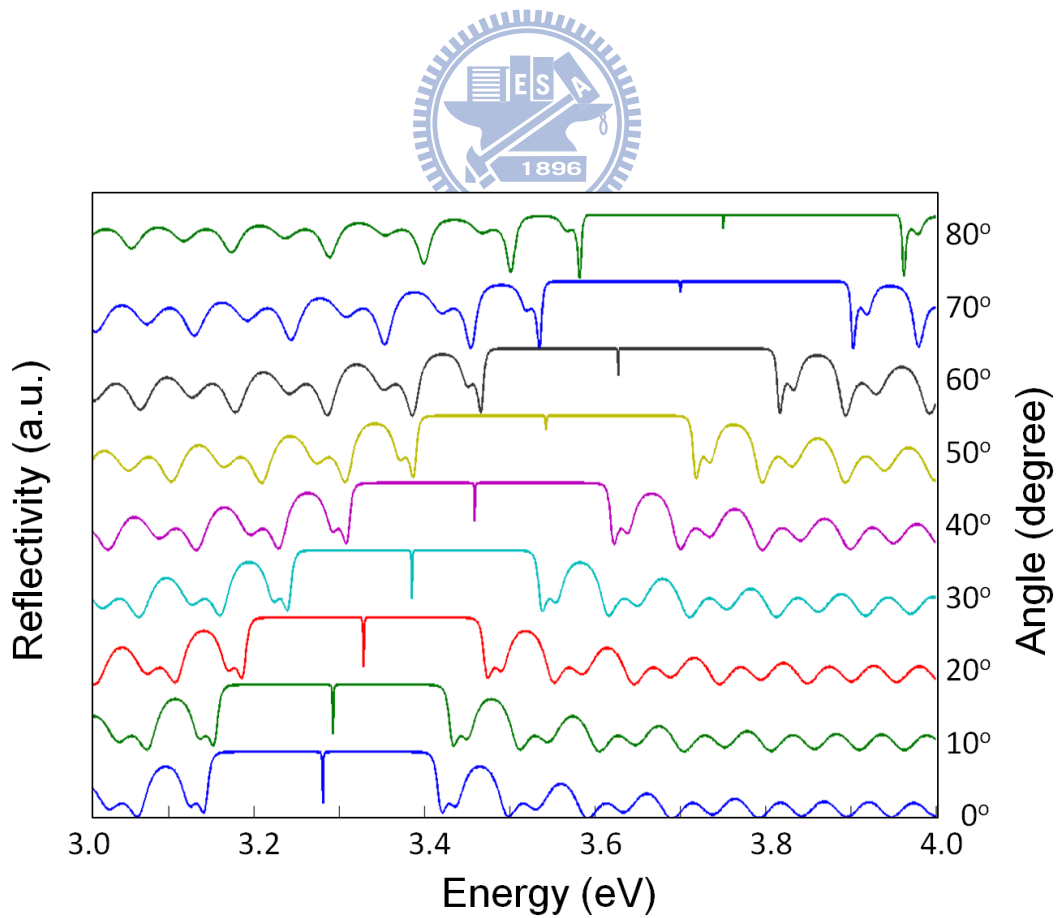


Fig 2.6 Incidence angle ( $\theta$ )-dependent reflectance for microcavity

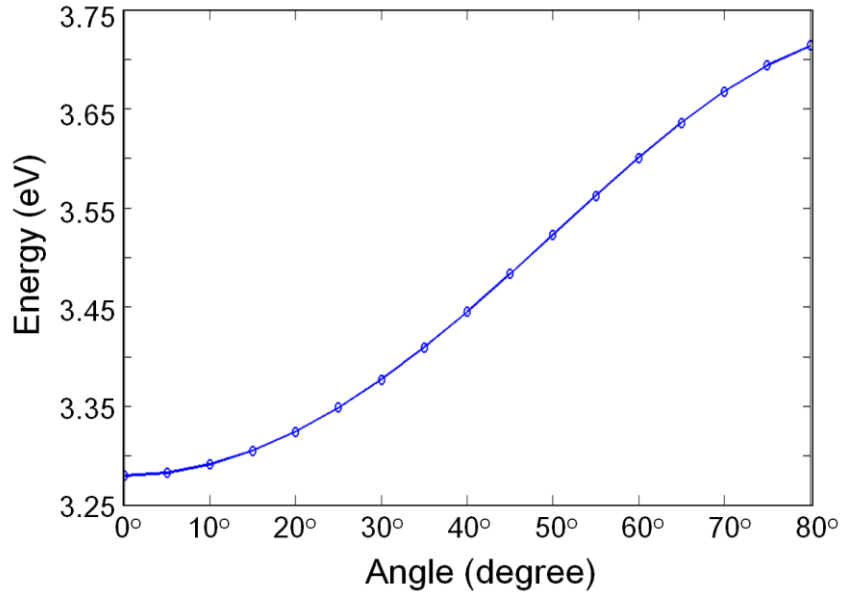


Fig 2.7 Pure cavity dispersion  $E_{cav}$  vs.  $\theta$

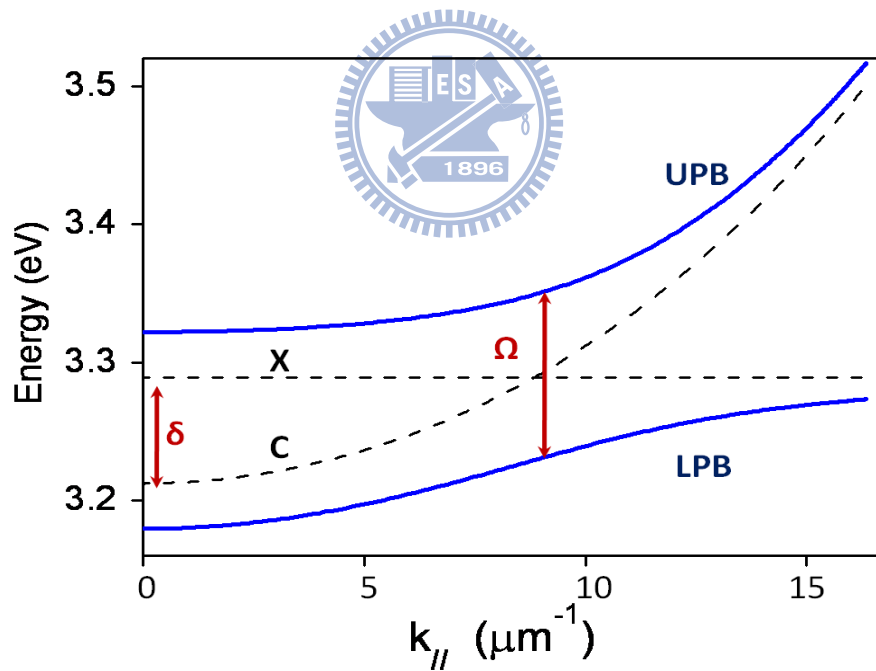


Fig 2.8 Anti-crossing of LP and UP energy levels when tuning the cavity energy across the exciton energy by transfer matrix calculation. X means the exciton mode, C pure cavity mode,  $\delta$  cavity-exciton detuning,  $\Omega$  Rabi-splitting, UPB upper polariton branch, and LPB lower polariton branch.

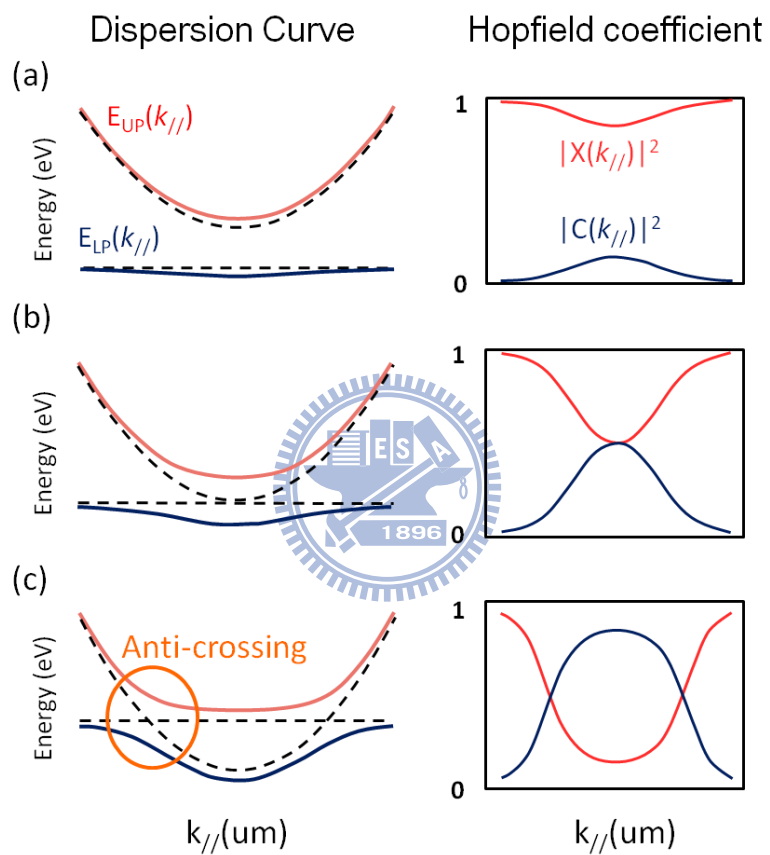


Fig 2.9 Polariton dispersions and corresponding Hopfield coefficients at (a)  $\delta < 0$  (b)  $\delta = 0$ , and (c)  $\delta > 0$ , where the negative detuning shows the obvious polaritonic characteristic : anticrossing.



## Chapter 3. Strong coupling regime in hybrid ZnO-based microcavity

### 3.1 Sample material and structure

An optimal microcavity system for polariton BEC shall have the following condition: (1) High quality cavity, hence long cavity photon and polariton lifetime. (2) Large polariton-phonon and polariton-polariton scattering cross-section, hence efficient polariton thermalization. (3) Small exciton Bohr radius and large exciton binding energy, hence high exciton saturation density. (4) Strong exciton-photon coupling, hence small decoherence rate. It requires both large exciton oscillator strength and large overlap of the photon field and the QWs. To address these issues, a careful choice of material is important. For given material, the exciton saturation density and exciton-photon coupling also depend on the structure design.

In 1992, the vacuum Rabi splitting in GaAs-based quantum well MCs was firstly observed by Weisbuch et al., and the amazing and peculiar experimental results have attracted a lot of interest for studies of BEC and potential applications. Nevertheless, the observation of polaritons in GaAs-based MCs can be only achieved at low temperature since the exciton binding energy of bulk GaAs is about 4 meV. Although GaAs-based MCs have high quality cavity for long cavity photon and polariton lifetime, we still need to search new material to overcome the problem as a result of the temperature limitation. The wide-bandgap semiconductor-based microcavities are the attractive candidates, such as ZnO whose exciton binding energy is about 60 meV for bulk layer.

For ZnO-based MCs, the strong coupling regime can be performed at RT due to strong coupling strength and binding energy, which unfortunately cannot be fulfilled by the GaAs based planar cavities. Besides, the smaller Bohr radius of ZnO excitons also allows a larger saturation density, and ZnO is itself a promising material for UV or visible photonic nanodevices [37,38]. Indeed, a large Rabi splitting of 120 meV has been reported recently for exciton polaritons in ZnO nanowire cavity exhibiting a FP type resonance [39]. This finding strongly suggests that ZnO microcavities may be a promising system for studying polariton physics and for developing “polariton laser”. However fabrication of high quality planar resonator using ZnO has not been achieved thus far [40].



### 3.1.1 Ultra-violet distributed Bragg reflectors

Epitaxial growth of nitride-based distributed Bragg reflectors (DBRs) is a critical approach to the development of GaN- and ZnO-based optical devices such as resonant-cavity light-emitting diodes (RCLEDs) [41, 42] and vertical-cavity surface-emitting lasers (VCSELs) [43, 44]. Nevertheless, contrary to the well-known AlAs/GaAs material system nitride-based compounds suffer from a large lattice mismatch of about 2.4% between AlN and GaN, which causes a huge challenge for the growth of high-reflectivity nitride-based DBRs. In general, there are three kinds of material systems used in nitride-based DBRs, including AlN/GaN, Al(Ga)N/(Al)GaN, and AlInN/GaN. The AlN/GaN DBRs provide the highest refractive index contrast

among the III-nitride compounds. Therefore, the high-reflectivity DBRs together with a large stopband width can be achieved simultaneously by employing a reduced number of pairs. However, the large lattice mismatch within AlN/GaN multilayers generally results in a tensile strain and the formation of cracks. These cracks tend to grow into V-shaped grooves and seriously affect the reflectivity of the DBR due to scattering, diffraction, and absorption. To prevent the formation of cracks, the  $\text{Al}_x\text{Ga}_{1-x}\text{N}/\text{Al}_y\text{Ga}_{1-y}\text{N}$  material system is usually used to reduce the strain in the whole DBR structure. Nevertheless, the refractive index contrast decreases with increasing Al composition in GaN or Ga composition in AlN, which leads to a reduced stopband width and the requirement of increased number of pairs to achieve high reflectivity.

In our work, the AlN/GaN DBRs were grown on 2 inch c-sapphire substrates in a low-pressure high-speed rotating-disk MOCVD system. During the growth, trimethylgallium (TMGa) and trimethylaluminum (TMAI) were used as group III source materials and ammonia ( $\text{NH}_3$ ) as the group V source material. After thermal cleaning of the substrate in hydrogen ambient for 5 min at 1100 °C, a 30-nm-thick GaN nucleation layer was grown at 550 °C. The growth temperature was raised up to 1040 °C for the growth of 3  $\mu\text{m}$  GaN buffer layer. Then, the AlN/GaN DBRs were grown under the fixed chamber pressure of  $1.33 \times 10^4$  Pa similar to the previous reported growth conditions [45]. Six 20-pair AlN/GaN DBR samples with different quarter-wavelength thicknesses were prepared and labeled DBRs I-VI. During the growth, we used *in-situ* monitoring reflectivity signals. By choosing the monitor

wavelength to be the specific stopband center wavelength, the thickness of each quarter-wavelength GaN and AlN can be precisely controlled by following the reflectance signals during the MOCVD growth

The surface morphology of the DBRs was studied by optical microscopy. The thicknesses of the total DBR structures were investigated by scanning electron microscopy (SEM). The reflectivity spectra of the AlN/GaN DBRs were measured by the n & k ultraviolet-visible spectrometer with normal incidence at RT (RT). The photoluminescence (PL) emission spectra of the DBRs were measured at RT in order to study the crystal quality of GaN layers. The excitation light of PL is a 325-nm line of HeCd laser and the PL emission is dispersed by a 0.32  $\mu\text{m}$  monochromator and detected with a photomultiplier with standard lock-in technique.

The designed center wavelengths of the DBRs I–VI are about 440, 417, 408, 392, 373, and 364 nm, respectively. Although it is well-known that the designed center wavelength of DBR VI will suffer the absorption of GaN layers, we will investigate the influence of GaN absorption on reflectivity and stopband width of the AlN/GaN DBRs. The total *in-situ* reflectance signal at 440 nm for the growth of DBR I is shown in Fig. 3.1. The reflectance signal of the general two-step process for the growth of GaN on sapphire is shown in Fig. 3.1 as well. After the growth of bulk GaN layer, it is obvious that the relative reflectivity is gradually saturated with increasing number of DBR pairs. Therefore, the thicknesses of quarter-wavelength DBR layers can be controlled precisely by monitoring the real time reflectance signal and the

growth rate can be estimated simultaneously. The growth rates of the AlN and GaN layers are about 0.6 and 2.3 Å/s, respectively. The cross-section SEM images of DBRs I-VI are shown in Fig.3.2.

Fig. 3.3 shows the measured (solid line) and simulated (dashed line) reflectivity spectra of DBRs I-VI. In Fig. 3.3(a), experimental measurement shows that the peak reflectivity of DBR I at 440 nm is about 97.2% and the stopband width is 36.6 nm. To compare experimental and calculated reflectivity spectra, theoretical simulation based on transfer matrix theory was performed using the layer thicknesses listed in Table 3.1 for DBRs I-VI. The refractive index dispersion and the extinction coefficient of the GaN layer were taken from the measured data based on a bulk GaN grown on sapphire substrate. As for the parameters of the AlN layer, since the wavelength range calculated here is far away from the bandgap of AlN, we only took the refractive index dispersion into account and ignored the extinction coefficient in our simulation. The calculated reflectivity spectra of DBRs I-VI are also shown in Fig. 3.3. By comparing the measured and calculated results, the characteristics of simulated reflectivity spectrum of DBR I including stopband width and the phase of the short- and long-wavelength oscillations are in good agreement with the measured spectrum, as shown in Fig. 3.3(a). The calculated peak reflectivity and stopband width are about 98.2% and 43.5 nm, respectively. These calculated values are larger than the measured results, which may come from the degradation of crystal quality in the samples and the structural imperfections such as deviations from the designed layer thickness and

interface roughness between each epitaxial layer. Moreover, the mismatch between the measured and calculated reflectivity spectra in the short wavelength interference fringes is due to the absorption in the GaN layers because it is difficult to perfectly consider the scattering loss and absorption of the bilayers in our simulation. Additionally, the calculated reflectivity spectrum of DBR VI deviates obviously from the measured result, as shown in Fig. 3.3 (f). Since the stopband of DBR VI is centered at a shorter wavelength than GaN bandgap (~363 nm), the absorption from GaN layers will play a greater role in the case of DBR VI. Although the extinction coefficient of a bulk GaN was taken into account in our calculation, the effects of strain and defects in the GaN layers of DBRs will modify the original absorption in a bulk GaN. Similarly, the measured short wavelength interference fringes in Figs. 3.3 (c)-(e) are not resolved as compared with simulation results. Consequently, according to the difference between the measured and calculated reflectivity spectra the effect of GaN absorption in the AlN/GaN DBRs is larger than that in a bulk GaN layer. Furthermore, the measured and calculated maximum reflectivity values and stopband widths of the DBRs I-VI are summarized in Fig. 3.4, respectively. The GaN absorption significantly influences the reflectivity and stopband width when the designed DBR wavelength is shorter than about 380 nm.

Thus, the simulation results show that the calculated reflectivity spectra deviate from the measured results with decreasing designed DBR wavelength due to the significant GaN absorption. RT PL measurement shows that the degradation of GaN

crystal quality in DBR structures is more serious than that of bulk GaN, which will significantly affect the reflectivity and stopband width of the AlN/GaN DBRs when the designed DBR wavelength is near GaN bandgap.

### 3.1.2 Microcavity structure design and quality

Our microcavity structure consists of a bulk ZnO  $3/2 \lambda$  thick cavity sandwiched between a bottom 30-pair AlN/AlGa<sub>N</sub> DBR and a top 9-period dielectric SiO<sub>2</sub>/HfO<sub>2</sub> DBR. Here we chose  $\lambda$  to be 380 nm in air. The growth condition is similar to the previous reported setup in section 3.1.1. The bulk ZnO  $3/2 \lambda$  thick cavity was grown on AlN/AlGa<sub>N</sub> DBR by pulse laser deposition (PLD) system under the growth temperature of about 550 °C. The 9-period SiO<sub>2</sub>/HfO<sub>2</sub> dielectric DBR was deposited by dual electron-beam gun evaporation system to complete the hybrid microcavity structure. The schematic sketch of the ZnO-based microcavity structure is shown in Fig. 3.5 (a). The interface between the AlN/AlGa<sub>N</sub> DBR and the ZnO cavity is smooth as seen from the cross-sectional scanning electron microscope (SEM) image in Fig. 3.5(b). Fig. 3.6 shows the RT PL spectrum from the ZnO film grown on AlN/AlGa<sub>N</sub> DBR. The good material quality of the ZnO film can be observed from the suppression of the deep level emission band in the RT PL spectrum.

The reflectivity spectra of a 30-pair AlN/Al<sub>0.23</sub>Ga<sub>0.77</sub>N DBR and a 9-pair SiO<sub>2</sub>/HfO<sub>2</sub> DBR were measured at RT respectively for normal incidence, as shown in Fig. 3.7. The peak reflectivity of bottom AlN/AlGa<sub>N</sub> DBR is about 93% and the stop

band width is about 145 meV. As for the top SiO<sub>2</sub>/HfO<sub>2</sub> DBR, the peak reflectivity and the stop band width are 97% and 790 meV, respectively. The RT PL spectrum from a half-cavity structure (i.e., without the top SiO<sub>2</sub>/HfO<sub>2</sub> DBR) is also shown in Fig. 3.7. It is found that the PL spectrum from the half-cavity ZnO layer is mostly covered by the stop band width of the bottom and top DBRs. Fig. 3.8 shows the RT reflectivity and PL spectra from the full ZnO MC structure at normal incidence. The PL linewidth is decreased to be about 15 meV ( $\Delta\lambda \sim 1.73$  nm) due to the microcavity effect and the PL peak energy is about 3.237 eV ( $\lambda \sim 383$  nm). Therefore, the cavity quality factor  $Q$  ( $=\lambda/\Delta\lambda$ ) is about 221 when the pump spot size is about 3  $\mu\text{m}$ . Furthermore, the cavity dip can be clearly observed in the reflectivity spectrum, which shows a precise alignment between the DBR stop band and the ZnO cavity thickness. We found that the cavity dip was strongly dependent on the sample position due to the thickness nonuniformity in the ZnO cavity layer and the bottom DBR.

## 3.2 Angle-resolved reflectivity

The first experiments to carry out with a sample are to find its eigenmodes, such as by a reflection measurement. Reflection measurement with low-intensity input light is a passive measurement which gives the eigen modes of the undisturbed system, as shown by the transfer matrix calculation results simultaneously.

### 3.2.1 Principles and setups

When taking into account the finite lifetime of the cavity photon and QW exciton,



the eigen-energy equation is modified as:

$$E_{LP,UP}(k_{//}) = \frac{1}{2} [E_{exc} + E_{cav} + i(\gamma_{cav} + \gamma_{exc})] \pm \sqrt{4\hbar^2\Omega^2 + [E_{exc} - E_{cav} + i(\gamma_{cav} - \gamma_{exc})]^2} \quad (3.2.1)$$

Here  $\gamma_{cav}$  is the out-coupling rate of a cavity photon due to imperfect mirrors, and  $\gamma_{exc}$  is the non-radiative decay rate of an exciton. There exists a one-to-one correspondence between an internal polariton in mode  $k_{//}$  and an external photon with the same energy and inplane-wavenumber, propagating at an angle  $\theta$  from in-plane direction. Furthermore, we can change different detuning via different position of our sample owing to the nonuniformity growth. The polariton is coupled to the photon via photonic component with a fixed coupling rate  $\gamma_{cav}$ . Thus the coupling strength must be larger than half of the difference in decay rates to exhibit anti-crossing, i.e., to have polaritons as the new eigen modes. The coupling rate is determined by the fixed cavity photon out-coupling rate. As a result, information about the internal polaritons can be directly obtained from the external photon emission by well developed optical techniques.

Fig 3.9(a) shows the schematic of experimental setups for measuring reflectance at RT, and Fig 3.9 (b) is the practical setup for the angle-resolved reflectivity. The experimental setup of angle-resolved reflectivity performed by using a two arm goniometer, and a xenon lamp was employed as a white light source. Trough a 6cm focal lens, the input beam is focused onto a spot  $\sim 100$   $\mu\text{m}$  in diameter on the sample surface with an incident angle  $\theta$ . The reflected beam is picked up by the 600  $\mu\text{m}$  core

UV optical fiber mounted on a rotating stage at the same angle  $\theta$ . Furthermore, we put a pinhole front the collection fiber to improve the angle-resolved resolution, and the angle-resolved resolution is about 1 degree in our setup. Because the emission spectra of xenon lamp are not flat broad band, we must replaced the sample by reference mirror with reflectance  $R_{\text{ref}}$  to normalize the reflectivity, then the ratio of the two reflected intensities corrected by  $R_{\text{ref}}$  gives the reflectance of the sample.

### 3.2.2 Simulation model

#### 3.2.2.1 Transfer matrix model

In our simulation work, we employ the transfer matrix [46] used in the calculation for the reflectivity spectrum. The coherent optical reflectance and transmittance of a multilayer structure are readily represented, for normally incident radiation, as a product of matrices, the system transfer matrix. This matrix method assumes a multilayer structure composed of optically isotropic and homogeneous layers, with plane and parallel faces. The elements of the system transfer matrix can be written in terms of the complex-amplitude reflection and transmission coefficients  $r$  and  $t$  of the multilayer structure.

First we consider the transmission and reflection off a single layer in a multiple layer system. The electrical and magnetic components of the wave in the upper interface of the material must be related to the electrical and magnetic components in the lower interface by some transformation matrix. In the simulation, the

transformation matrix can divide into two parts: one is interface matrix, and the other is propagation matrix. Through the periodic product of these two matrices, we can get the total transformation matrix for the multilayer-structure microcavity. We can further get the reflection and transmittance coefficients via the elements in the transformation matrix. The following text is the detailed calculation for reflection and transmittance coefficient

1. interface matrix (Fig 3.10 (a))

Assumption of the incident wave is transverse wave (TE wave), through the boundary condition, we can get:

$$E_1 + E' = E_2 + E'_2 \quad (3.2-2)$$

$$\frac{E_1 n_1 \cos \theta_1}{\eta_0} + \frac{E'_1 n_1 \cos \theta_1}{\eta_0} = \frac{E_2 n_2 \cos \theta_2}{\eta_0} + \frac{E'_2 n_2 \cos \theta_2}{\eta_0} \quad (3.2-3)$$

By (2.1-1) and (2.1-2), it is described

$$\begin{bmatrix} 1 & 1 \\ n_1 \cos \theta_1 & -n_1 \cos \theta_1 \end{bmatrix} \begin{bmatrix} E_1 \\ E'_1 \end{bmatrix} = \begin{bmatrix} 1 & 1 \\ n_2 \cos \theta_2 & -n_2 \cos \theta_2 \end{bmatrix} \begin{bmatrix} E_2 \\ E'_2 \end{bmatrix} \quad (3.2-4)$$

Set

$$D_1 = \begin{bmatrix} 1 & 1 \\ \alpha_1 & -\alpha_1 \end{bmatrix} \quad D_2 = \begin{bmatrix} 1 & 1 \\ \alpha_2 & -\alpha_2 \end{bmatrix} \quad \alpha_m = n_m \cos \theta_m \quad \text{which } m \text{ is the number of}$$

multiple layers. The (2.1-3) can be described

$$D_1 \begin{bmatrix} E_1 \\ E'_1 \end{bmatrix} = D_2 \begin{bmatrix} E_2 \\ E'_2 \end{bmatrix} \quad (3.2-5)$$

After the matrix calculation, we can get a new  $2 \times 2$  matrices in square

$$\begin{bmatrix} E_1 \\ E'_1 \end{bmatrix} = D_{12} \begin{bmatrix} E_2 \\ E'_2 \end{bmatrix} \quad (3.2-6)$$

$$D_{12} = D_1^{-1} D_2 = \begin{bmatrix} \frac{n_1 \cos \theta_1 + n_2 \cos \theta_2}{2n_1 \cos \theta_1} & \frac{n_1 \cos \theta_1 - n_2 \cos \theta_2}{2n_1 \cos \theta_1} \\ \frac{n_1 \cos \theta_1 - n_2 \cos \theta_2}{2n_1 \cos \theta_1} & \frac{n_1 \cos \theta_1 + n_2 \cos \theta_2}{2n_1 \cos \theta_1} \end{bmatrix} = \frac{1}{t_{12}} \begin{bmatrix} 1 & r_{12} \\ r_{12} & 1 \end{bmatrix} \quad (3.2-7)$$

The interface matrix ( $D_{12}$ ) can be presented by reflection coefficient ( $r_{12}$ ) and transmittance coefficients ( $t_{12}$ )

2. Propagation matrix :

From the Figure Fig 3.10 (b)

$$\begin{cases} B = A e^{-jk_z d_m} = A e^{-j\phi_m} \\ B' = A' e^{-jk_z d_m} = A' e^{-j\phi_m} \end{cases} \quad (3.2-8)$$

where  $\phi_m = k_0 n_m \cos \theta_m d_m$   $\cos \theta_m = \sqrt{1 - \left(\frac{n_0}{n_m} \sin \theta_0\right)^2}$

We can describe the (3.2-8) by

$$\begin{bmatrix} A \\ A' \end{bmatrix} = \begin{bmatrix} e^{j\phi} & 0 \\ 0 & e^{j\phi} \end{bmatrix} \begin{bmatrix} B \\ B' \end{bmatrix} = P_m \begin{bmatrix} B \\ B' \end{bmatrix} \quad (3.2-9)$$

where  $P_m$  is the propagation matrix for the  $m_{th}$  layer. The above-mentioned calculation is for the single layer structure, we can spread the result to multilayer structure calculation.

The Fig. 3.11 shows multilayer structure for transfer matrix, where  $n_m$  is the refractive index for the  $m_{th}$  layer,  $d_m$  is the thickness for the  $m_{th}$  layer. For the propagation wave, the  $A_m$  is the original incident wave for the  $m_{th}$  layer, the  $A_m'$  the incident wave through  $d_m$  thickness for the  $m_{th}$  layer,  $\tilde{A}_m$  original reflective wave for the  $m_{th}$  layer, and  $\tilde{A}_m'$  the reflective wave through  $d_m$  thickness for the  $m_{th}$  layer

Set

$$\bar{A}_0 = \begin{bmatrix} A_0 \\ A'_0 \end{bmatrix}, \bar{A}_1 = \begin{bmatrix} A_1 \\ A'_1 \end{bmatrix}, \text{ \& } \tilde{\bar{A}}_1 = \begin{bmatrix} \tilde{A}_1 \\ \tilde{A}'_1 \end{bmatrix}$$

Via the former interface and propagation matrix, we can get

$$D_0 \bar{A}_0 = D_1 \bar{A}_1, \bar{A}_1 = P_1 \tilde{\bar{A}}_1, D_1 \tilde{\bar{A}}_1 = D_2 \bar{A}_2 \quad (3.2-10)$$

Then we can transfer the (3.2-10) into the form of (3.2-11)

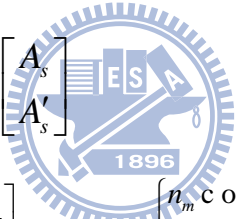
$$\bar{A}_0 = D_0^{-1} D_1 (P_1 \tilde{\bar{A}}_1) = D_0^{-1} (D_1 P_1 D_1^{-1}) D_2 \bar{A}_2 \quad (3.2-11)$$

We expand the (3.2-11) for  $n$  layer

$$\bar{A}_0 = D_0^{-1} (D_1 P_1 D_1^{-1}) (D_2 P_2 D_2^{-1}) \dots \dots \dots (D_n P_n D_n^{-1}) D_s \bar{A}_s \quad (3.2-12)$$

Finally, the (3.2-12) can be represented as

$$\begin{bmatrix} A_0 \\ A'_0 \end{bmatrix} = D_0^{-1} \left[ \prod_{m=1}^N D_m P_m D_m^{-1} \right] D_s \begin{bmatrix} A_s \\ A'_s \end{bmatrix} \quad (3.2-13)$$



$$D_m = \begin{bmatrix} 1 & 1 \\ \alpha_m & -\alpha_m \end{bmatrix}, \quad D_m^{-1} = \begin{bmatrix} \frac{1}{2} & \frac{1}{2\alpha_m} \\ \frac{1}{2} & \frac{-1}{2\alpha_m} \end{bmatrix}, \quad \alpha_m = \begin{cases} n_m \cos \theta_m \\ \frac{\cos \theta_m}{n_m} \end{cases}$$

There are two forms for  $\alpha_m$  : one is  $n_m \cos \theta_m$  for transverse wave, and the other is  $n_m / \cos \theta_m$  for the polarization wave.

In the last, we can acquire the transformation matrix for  $n$  layer structure.

$$M = D_0^{-1} \left[ \prod_{m=1}^N D_m P_m D_m^{-1} \right] D_s = \begin{bmatrix} M_{11} & M_{12} \\ M_{21} & M_{22} \end{bmatrix}_s \quad (3.2-14)$$

Where the reflection coefficient  $r = \frac{M_{21}}{M_{11}}$  and the transmittance coefficient  $t = \frac{1}{M_{11}}$ ,

thus we can further obtain the reflectivity  $R = r^2$  and transmittance  $T = t^2$ .

### 3.2.2.2 Oscillator model of strong coupling regime

The basic ideas of semiconductor in strong coupling regime are introduced for the example of an ensemble of oscillators in a planar Fabry-Pérot interferometer. In our analysis presented in this section we characterize light-matter interaction via absorption and refractive index. The fundamental excitonic transition is modeled as Lorentz oscillators in dielectric constant dispersion formula, which can be expressed as follows:

$$\varepsilon_r = \varepsilon_b + \frac{B}{E_0^2 - E^2 + j\Gamma E} \quad n = \sqrt{\varepsilon_r} \quad (3.2-15)$$

Where  $\varepsilon_b$  background dielectric constant  $E_0$  is the transition energy,  $B$  the parameter related to the oscillator strength and  $\Gamma$  the homogeneous broadening of the transition. Thus, we replace the general material dispersion with the Lorentz oscillator model to take into account of the light-matter strong coupling regime. Fig. 3.12 shows the reflectivity of pure cavity mode and the polariton mode in strong coupling regime.

### 3.2.3 Experimental results of strong coupling regime in ZnO microcavities

To further probe the characteristics of strong exciton-photon coupling in the ZnO MC structure, RT angle-resolved reflectivity measurements were performed for the observation of in-plane polariton dispersion curves. Such two series of RT angle-resolved reflectivity spectra ranging from  $8^\circ$  to  $40^\circ$  are shown in Fig. 3.13(a) and Fig 3.13(b) of different detunings of -93 meV and -53meV respectively. In the both case, it is obvious that the lower polariton branch (LPB) follows a parabolic

dispersion curve at small angles. Furthermore, with increasing incident angle, the LPB deviates from the original parabolic dispersion curve and approaches to the uncoupled exciton mode (X). The RT experimental and theoretical polariton dispersion curves are plotted in Fig 3.14(a) and (b). The theoretically calculated LPB is in good agreement with the experimental results, which implies the existence of cavity-polaritons. Large vacuum Rabi splitting of about 68 meV are estimated when the incident angle are  $33.7^\circ$  and  $27.3^\circ$  for the both detuning respectively.

To show the more obvious polariton dispersion curve, the color map of the measured angle-resolved reflectivity spectra is plotted in Fig. 3.15 for the case with the detunings of -93 meV. The color map of the angular dispersion of measured reflectivity spectra from  $8^\circ$  to  $38^\circ$  is shown in Fig. 3.15 (a). Furthermore, the color maps of the calculated angle-resolved reflectivity spectra without and with taking the resonant exciton into account are shown in Fig. 3.15 (b) and Fig. 3.15 (c) respectively. The theoretically calculated exciton-polariton dispersion curves are in good agreement with the measured results as we assign the parameter related to the oscillator strength to be about  $1.6 \times 10^5 \text{ meV}^2$  in our calculations. This value is reasonable for the materials with wide bandgap and large oscillator strength. In Fig. 3.15 (c), the pure cavity mode, marked with C, follows the parabolic dispersion, which is consistent with the Bragg mode (BM) from the low energy side of the stop band. However, when we consider the resonant exciton in our calculation, the behavior shown in Fig. 3.15 (c) is the characteristic of mode mixing between the

cavity and exciton modes, and the formation of lower and upper polariton branches (LPB and UPB) near the angle of about  $34^\circ$ . Under this circumstance, the photonlike lower polariton branch will approach to excitonlike lower polariton branch with increasing angle. Therefore, the LPB dispersion curve doesn't follow the original pure photon parabolic dispersion curve because of the strong interaction between photon and exciton modes. In the color map of the measured angle-resolved reflectivity spectra shown in Fig. 3.15 (a), the dispersion of the lower polariton branch deviates from the parabolic cavity mode and approach to exciton mode with increasing angle. Therefore, by comparing Fig. 3.15 (a) and Fig. 3.15 (c), the strong coupling phenomenon between exciton and photon modes is observed in this hybrid ZnO-based microcavity structure. However, the features of upper polariton branch (UPB) cannot be observed in the experimental results, and the phenomenon is ascribed to the scattering between polariton and excitonic scattering state. We will investigate the UPB broadening in the following text.

### 3.2.4 Exciton scattering states absorption

Although the angular dispersion of the LPB is well visible from experimental results, the signature of the UPB is nearly not observable, as shown in Fig. 3.15 (a). This interesting issue regarding the anticrossing behavior in bulk ZnO MCs was reported by Faure *et al.* in 2008. [47] They theoretically expected that the anti-crossing behavior can be properly defined in bulk GaAs and GaN MCs, whereas



only the LPB is a well-defined and well-mixed exciton-photon state in bulk ZnO MCs.

It is noteworthy that when the exciton eigenenergies are larger than zero, the eigenstates are not discrete bound states any more. They will be continuously distributed eigenstates termed continuum (scattering) states. Therefore, when the Rabi splitting value is of the same order or larger than the effective Rydberg energy such as ZnO-based MCs [48], the UPB will be pushed up to the energies of the exciton scattering states, and then upper polaritons scatter with exciton scattering states, which leads to the strong damping of the polaritons. Thus, they proposed that the UPB in bulk ZnO MCs is pushed into the scattering states of excitons due to the large vacuum Rabi splitting of 120 meV (i.e., twice larger than the exciton binding energy) in their calculation. Nevertheless, the Rabi splitting estimated in our structure is about 68 meV, which is only slightly larger than the exciton binding energy. Therefore, the UPB will not overlap with the exciton scattering states.

To understand the origin of the invisible UPB in the bulk ZnO MC, except for the exciton scattering states, we further take into account the effect of absorption induced by scattering states of excitons in our simulation. The 3D exciton physical model is used in our calculation to involve the absorption of bound states and scattering states. The absorption due to scattering states is added into the dielectric function and the amplitude is adjusted to match the experimental absorption spectra. Fig. 3.16 shows the experimental (open blue circle) and simulated (solid line)

absorption spectra of a bulk ZnO at RT. [49] When the vacuum Rabi splitting energy is nearly the same as the exciton binding energy, it will give rise to the energy overlap between the UPB and the scattering states, which may originate from the exciton excited states, the onset of scattering absorption, and the exciton-phonon complexes, especially at RT. In our simulation work, we further include the absorption of exciton scattering states in our simulation. Fig. 3(c) presents the simulation of angle-resolved reflectivity spectra for the bulk ZnO MCs after taking the scattering absorption into account. It is clearly observed that the UPB is significantly broadened due to its crossing with the scattering states of excitons. Such a situation is especially important for bulk ZnO MCs due to the relatively thick cavity layer and the large absorption coefficient ( $\sim 2 \times 10^5 \text{ cm}^{-1}$ ) for ZnO materials. These effects induce the damping of the coherence for upper polariton states and lead to the dispersion of UPB to be invisible. Although the full anticrossing behavior cannot be experimentally demonstrated because of the strong scattering absorption, it should be noted that clear observation of the LPB is more important for the investigation of Bose-Einstein condensation and polariton lasing. Furthermore, there are other physical factor will influence the UPB performance, and we will investigate these physical mechanism comprehensively in section 3.3.

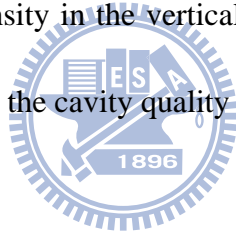
### 3.3. Broadening of upper polariton branch

The well-distinguished lower polariton branches (LPBs) and upper polariton

branches (UPBs) are characteristics of strong coupling in semiconductor microcavities (MCs). In practice, however, the UPBs are often broadening especially in wide-bandgap material MCs. We present in detail the possible physical mechanisms for the broadening of UPBs for different designs of MCs by numerical simulations based on GaAs, GaN and ZnO materials. The calculated results show that the UPBs of the GaN- and ZnO-based MCs will become indistinct when the thickness of optical cavity is larger than  $\lambda$  and  $0.25\lambda$ , respectively, mainly attributed to the larger product of the absorption coefficient and the active layer thickness. In wide-bandgap materials, it would be relatively easier to observe the UPB in the case of negative exciton-photon detuning due to the exciton-like UPB and lower absorption of scattering states. In addition, the inhomogeneous broadening would be an important factor causing the invisible UPB in wide-bandgap semiconductor MCs at negative detuning. We demonstrate that in multiple quantum-well embedded ZnO-based MCs, the UPB could be well-defined due to the large 2D exciton binding energy and the small product of absorption coefficient and active layer thickness. These results show that the UPBs can be properly defined in wide-bandgap semiconductor MCs by appropriate design of MC structures.

### **3.3.1. Comparison of UPB broadening between microcavities based on different materials**

For simplicity, the MC structures are composed of the same dielectric SiO<sub>2</sub>/HfO<sub>2</sub> Bragg mirrors and the active layer is based on the bulk GaAs, GaN, or ZnO, respectively. In addition, it is noteworthy that there are two compensating layers symmetrically on the both sides of the active layer, as shown in Fig. 3.18(a). These two layers are added in the optical cavity to satisfy the cavity thickness of  $m\lambda/2$ , where  $m$  is the number of cavity mode. Based on this design structure, we can obtain the mapping of the reflectivity spectra of MCs with continuous variable active layer thicknesses. We have to emphasize that the two compensating layers are not taken into account in strong light-matter interaction. Fig. 3.18(b) shows the refractive index profile and the optical-field intensity in the vertical direction. Moreover, the number of DBR layers is adjusted to keep the cavity quality factor the same for the pure cavity mode.



In the calculation, we only considered the excitonic transition from fundamental state ( $1s$ ) based on the assumption of probing the polariton properties of wide-bandgap materials (GaN and ZnO) at RT. In addition, the oscillator strength of  $ns$  excited states is inversely proportional to  $n^3$  [50], with  $n$  being the principle quantum number. Therefore, the excited states contribute only minor interaction with cavity photon modes. On the other hand, since excitons in GaAs are unstable and hardly exist at RT, we employed the relevant parameters obtained from the experimental measurements at cryogenic temperature for GaAs material [51]. The linewidths of exciton resonances are characterized by the same homogeneous

broadening of 1 meV in the three materials in order to clear the specificities and differences. The similar results are obtained for larger homogeneous broadening (~15 meV).

The reflectivity spectra of the MCs for three materials were calculated based on transfer matrix method [52] and the resonant exciton was modeled by a Lorentz oscillator dispersive dielectric function [53]. Besides, in order to take the exciton scattering states into account, the 3D exciton physical model is used in our calculation to involve the absorption of bound states and scattering states, which can be described as [54]

$$\alpha(\hbar\omega) = \frac{A_0}{2\pi^2 R_y a_0^3} \left[ 4 \sum \frac{\gamma/n^3}{(\chi + 1/n^2)^2 + \gamma^2} + \int \frac{d\chi'}{\pi} \frac{\gamma S_{3D}(\chi') \sqrt{\chi'}}{(\chi - \chi')^2 + \gamma^2} \right] \quad (3.2-16)$$

where  $A_0$  is proportional to the momentum matrix element of bulk semiconductors,  $R_y$  is the exciton Rydberg energy,  $a_0$  is the exciton Bohr radius,  $\gamma$  is the half-linewidth normalized by Rydberg,  $\chi$  is a normalized energy  $(\hbar\omega - E_g)/R_y$ , and  $S_{3D}$  is called the Sommerfeld enhancement factor and can be expressed as

$$S_{3D}(\chi) = \frac{2\pi / \sqrt{\chi}}{1 - e^{-2\pi / \sqrt{\chi}}}. \quad (3.2-17)$$

The corresponding parameters of the three materials were extracted from the literatures [55-60] and summarized in Table 3.2. By employing the 3D exciton model, we can define the scattering absorption including scattering states and excitonic absorption. The calculated results for the three materials are consistent with the

absorption spectra reported by Refs. [56-58].

### 3.3.1.1. Influence of the active layer thickness

In bulk semiconductor MCs system, the Rabi-splitting is strongly dependent on the thickness of cavity layer since the whole cavity can be referred to as the active material. Therefore, it is expected that the Rabi-splitting will increase with the thickness of the cavity layer due to the increased overlap between matter and confined photons [55]. Generally, the Rabi splitting in a semiconductor MC can be described by [59]

$$\Omega = 2\sqrt{\omega_0\omega_{LT}(d/L_{eff})} \quad (3.2-18)$$

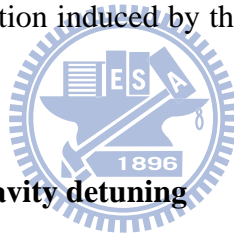
where  $\omega_0$  is the exciton resonance energy,  $\omega_{LT}$  the effective longitudinal-transverse splitting,  $d$  the active layer thickness, and  $L_{eff}$  the effective cavity thickness involving the optical field penetration in distributed Bragg reflectors (DBRs). An increase in Rabi splitting is obtained with increasing the active layer thickness of bulk cavity due to the larger ratio  $d/L_{eff}$  [51].

Fig. 3.19 presents the color maps of reflectivity spectra as a function of the active layer thickness for GaAs, GaN, and ZnO MCs, respectively. The reflectivity spectra were calculated in the condition of zero detuning and normal incidence ( $k_{||} = 0$ ). The calculated Rabi splitting values for the three MCs with optical thickness of  $1\lambda$  are listed in Table 3.3. In Fig. 3.19, it is apparent that there are two main branches, the UPB and LPB, for these three MC structures and the Rabi splitting becomes larger with increasing active layer thickness. It is worthy to mention that the Rabi splitting

near the  $0.5\lambda$  optical thickness of active layer shows approximately constant (i.e., the UPB and LPB are nearly parallel), which originates from the small increase in the exciton-photon interaction due to the node of the optical field in the MC structure. In the GaAs-based MCs, since the Rabi splitting is comparable to the effective Rydberg energy, as shown in [Tables 3.2 and 3.3](#), the UPB is broader than the LPB with increasing Rabi splitting because of its crossing with the scattering states of excitons. Nevertheless, it is still distinguishable even the optical thickness of the active layer is  $1.5\lambda$  [\[51\]](#). Furthermore, the UPBs of GaN and ZnO become broader with increasing thickness of active layer and subsequently fade as the optical thickness of about  $1\lambda$  and  $0.25\lambda$  for GaN and ZnO, respectively. These calculated results are in good agreement with the experimental measurements in recent literatures [\[59, 62-65\]](#). It is obvious that the maximum thickness of active layer for the visible UPB is different in the three materials. To clearly probe the UPB in ZnO MCs, the optical thickness of active layer should be kept thinner than  $0.25\lambda$  to suppress the absorption of scattering states, which may mainly originate from the onset of scattering absorption and the exciton-phonon complexes, especially at RT [\[66\]](#). Moreover, there are observable intermediate polariton branches (IPBs) in the map of the calculated reflectivity spectra nearby and above the exciton energy for GaN and ZnO MCs. This issue will be discussed further in [Sec. 3.3.2](#).

In addition, the important factor resulting in the discrepancies between the three materials is the product of the absorption coefficient and the active layer thickness

( $\alpha \cdot d$ ). The absorption coefficients near the band edge of GaN and ZnO are about one order of magnitude larger than that of GaAs, as shown in [Table 3.2](#). Specifically, a bulk GaAs with an optical thickness of  $1.5\lambda$  will absorb 49% of photons in a single pass when the photon energy is near the onset of the scattering states. As for a bulk ZnO with an optical thickness of  $1\lambda$ , there is 95% of photons absorbed by the scattering states. To sum up the influence of the active thickness, when the thickness of bulk active layer increases, there are two mechanisms leading to the invisible UPBs for the wide-bandgap materials. One is the large Rabi splitting with increasing the active layer thickness, which pushes the UPB into the absorption of scattering states. The other is the increased absorption induced by the increase in the thickness of bulk active layer.



### 3.3.1.2. Influence of exciton-cavity detuning

The effect of exciton-photon detuning dominates the polariton dispersion curves and therefore influences the characteristics of UPB. It has been observed that the linewidth of upper polariton increases with positive detuning due to the overlap between exciton scattering states and UPB in GaAs-based MCs [\[67, 68\]](#). Furthermore, semiclassical approach of linear dispersion theory including the scattering absorption presents the similar trend about detuning-dependent UPB linewidths [\[69\]](#). Therefore, to further investigate the effect of exciton-photon detuning on the properties of UPB in these three materials, we fixed the optical thickness of active layer to be  $0.5 \lambda$  for the three MCs and slightly changed the cavity thickness to increase or decrease the

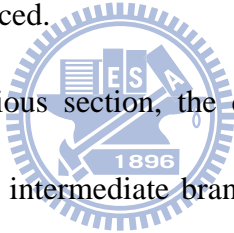


exciton-photon detuning. Fig. 3.20 shows the color maps of the calculated reflectivity spectra as a function of exciton-photon detuning for the three materials. A clear anticrossing behavior is observed for GaAs- and GaN-based MCs, respectively. Nevertheless, the signature of the UPB and LPB disappears rapidly in the GaAs MC with the varying detunings from zero. On the contrary, in the cases of GaN and ZnO MCs, the signatures of the UPB and LPB are still visible even though the detuning deviates from the zero detuning, since their exciton oscillator strength values are one order larger than that of GaAs [53, 55, 70]. Furthermore, although the anticrossing can be observed in the GaN MC, the signature of the UPB nearly disappears when the positive detuning is larger than about 10 meV. Similar situation also can be found in the ZnO MC when the detuning goes from negative to zero. For positive detuning, the upper polariton has high photon fractions, leading to the invisible UPB abruptly with increasing positive detuning due to the crossing with exciton scattering states. The UPB in GaAs MC is still distinct because the small term of  $\alpha d$ , as shown in Fig. 3.19(a). Therefore, in wide-bandgap materials it would be relatively easier to observe the UPB in the case of negative exciton-photon detuning, besides the thinner active layer thickness as discussed in Sec. 3.3.1

### 3.3.2. Influence of inhomogeneous broadening

Inhomogeneous broadening of excitons plays an important role in the investigation of strong exciton photon coupling as well, especially for wide-bandgap materials due to the difficulty in growth of high reflectivity DBRs and high  $Q$  cavities.

The effect of disorder on bulk polaritons results from the interaction between exciton states and imperfect bulk crystals. This mechanism breaks the conservation rule of in-plane wave vector in the exciton-photon interaction. As a result, the set of the disordered potential contributes to inhomogeneous broadening for the exciton-like polariton states in spectra. Currently, the epitaxial growth of wide-bandgap materials suffers from the severe strain accumulation in the DBRs, leading to crystal defects and potential fluctuations. Additionally, the small effective Bohr radius in wide-bandgap materials causes the polaritons more probably to be trapped by defects and perturbed by potential fluctuations, which results in the coherence length of polaritons to be significantly reduced.



As mentioned in the previous section, the calculated reflectivity spectra, as shown in Fig. 3.19, exhibit clear intermediate branches between the LPB and UPB. The IPBs are mainly resulted from the strong changes in the refractive index and the incoherent exciton absorption owing to the outcome of large exciton oscillator strength. However, these IPBs have never been observed experimentally in GaN- or ZnO-based MCs [63, 65]. Furthermore, although the results shown in Fig. 3.21 present visible UPBs with sharp linewidth in the range of negative detuning for the three materials, the most experimental results in reflectivity and photoluminescence spectra exhibit the broad linewidth of UPB [63, 65]. These differences are mainly attributed to the lack of inhomogeneous broadening in the calculation model. Therefore, in order to take the effect of inhomogeneous broadening into account, the

simulation model are reconstructed from a convolution of a Lorentzian lineshape and a Gaussian lineshape, which is more appropriate in the case of inhomogeneous broadening. The exciton Gaussian lineshape is symmetrically distributed in our work to avoid the breaking of translational symmetry and to modify the polariton eigenstates [71].

$$\varepsilon_r(E) = \varepsilon_b + \sum_i \frac{1}{\sqrt{2\pi}\Delta_i} \int \frac{B_i e^{-(x-E_{0i})^2/2\Delta_i^2}}{x^2 - E^2 - j\Gamma_i E} dx \quad (3.2-18)$$

where  $E$  is the cavity mode, and  $x$  is the exciton transition energy. The average transition energy is called  $E_{0i}$ , and a Gaussian distribution is used with a inhomogeneous broadening parameter  $\Delta_i$

The calculated results shown in Fig. 4 indicate that the UPBs in the range of positive detuning are significantly broadened by the absorption of exciton scattering states. As for the UPBs in the range of negative detuning, the inhomogeneous broadening will be the dominate mechanism leading to the invisible UPBs due to the exciton-like polaritons. Fig. 5(a) shows the calculated reflectivity spectra for the  $\lambda$  ZnO cavity in the condition of negative detuning of 50 meV and zero in-plane wavevector as varying the inhomogeneous broadening ranging from 1 to 10 meV. Fig. 5(b) presents the color map of the reflectivity spectra as a function of inhomogeneous broadening. The LPB is clearly distinguishable even if the inhomogeneous broadening increases to be 10 meV. However, the intermediate dips (i.e., IPBs) resulting from the incoherent excitons rapidly vanish with increasing inhomogeneous broadening, and finally the UPB becomes blurred and fades as the inhomogeneous

broadening approaches to 10 meV. The disappearance of UPB with increasing inhomogeneous broadening is mainly induced by the intrinsic exciton-like properties for the condition of negative detuning. On the contrary, the LPB is photon-like and therefore robust in spite of the increase of inhomogeneous broadening. Consequently, the inhomogeneous broadening induced by crystal imperfection would also be an important factor causing the invisible UPB in wide-bandgap semiconductor MCs.

### **3.3.3. Comparison between QWs-embedded and bulk ZnO-based microcavities**

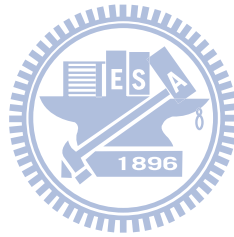
The above-discussed studies of strongly exciton-photon coupling are mainly based on bulk MCs because of the simpler geometry and the easier fabrication in practice, especially for wide-bandgap materials. However, with the target of realizing an electrically pumped polariton laser, a more realistic structure would employ QWs to achieve lower threshold due to improved carrier confinement and large oscillator strength. Recently, the strong coupling based on a GaN/AlGaIn multiple quantum well (MQW) MC structure has been experimentally demonstrated [72]. Nevertheless, the ZnO-based MQW MCs, such as ZnO/ZnMgO, have not been reported. Therefore, we will now focus on the comparison of polariton dispersion curves in bulk ZnO and ZnO/ZnMgO MQW MCs.

The MC structures for the bulk ZnO and ZnO/ZnMgO MQW are identical except for the design of cavities. The cavity thickness of these two structures is  $0.5\lambda$  and the MQW structure consists of three 3-nm ZnO QWs and 5-nm  $\text{Zn}_{0.73}\text{Mg}_{0.27}\text{O}$

barriers, which are symmetrically distributed around the anti-node of the optical field. In addition, the variations of exciton transition and binding energies in a ZnO/Zn<sub>0.73</sub>Mg<sub>0.27</sub>O QW as a function of well width have been investigated in the work by Coli and Bajaj [73]. The measured transition energy in a QW structure consisting of a 3-nm-thick ZnO well and Zn<sub>0.73</sub>Mg<sub>0.27</sub>O barriers is about 3.39 eV [73, 74].

Fig. 3.22 shows the comparison of the angle-resolved reflectivity spectra ranging from  $-35^\circ$  to  $35^\circ$  between MQW and bulk ZnO-based MCs. In Fig. 3.22 (a), it is obvious that the MQW ZnO-based MC presents an evident UPB. Therefore, it is easy to estimate the value of Rabi splitting. On the contrary, in the bulk ZnO MC the upper polariton is blurred and completely fades as a result of the intense damping by scattering states. The main factors resulting in the difference between MQW MC and bulk MC are essentially attributed to two reasons. One is the product of the absorption coefficient and the cavity thickness ( $\alpha \cdot d$ ). In the QWs-embedded MCs this value is effectively reduced because of the thinner active layer thickness. To be more specific, the product ( $\alpha \cdot d$ ) in a single pass is about 0.36 in the case of QWs-embedded MCs, which is about ten times less than that in bulk ZnO MCs ( $\sim 3.0$ ). The other is the difference in exciton binding energies. The QW structure is supposed to have larger exciton binding energy than bulk active layer. For ideal 2D QW structure, the exciton binding energy is expected to be 4 times larger than that in bulk active layer [14]. However, the practical QW is a quasi-2D structure since the wave functions of

electron and hole are confined in the direction normal to the wafer surface in a finite well width, which implies that the exciton binding energy in a quasi-2D QW is smaller than that in an ideal 2D QW. Additionally, the quantum confined Stark effects in c-axis ZnO QWs can shift the absorption peak and reduce exciton binding energies. Consequently, we assume the exciton binding energy of the ZnO/ZnMgO QW to be 99 meV in our calculation [75]. Under this condition, the exciton scattering states will be much far from the UPB, which is another benefit for the MQW ZnO-based MC in order to probe the visible UPB.



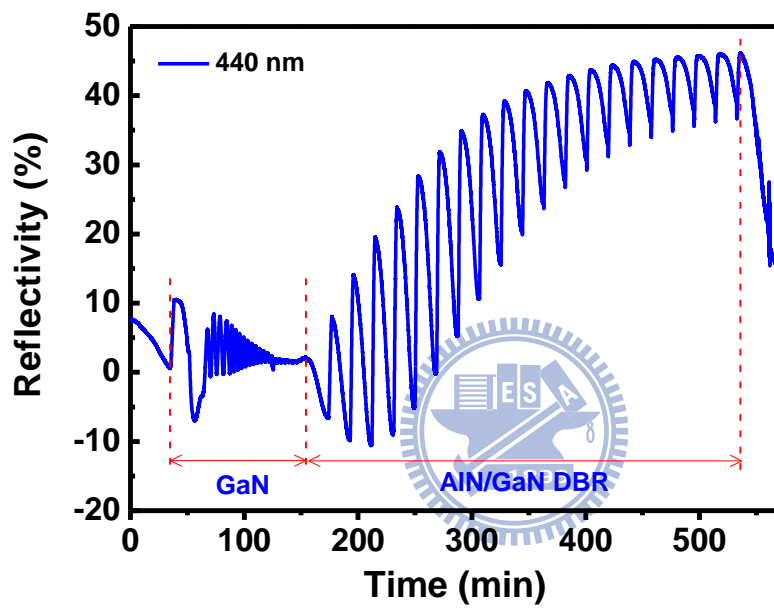


Fig 3.1 Total *in-situ* reflectance signal at 440 nm for the growth of DBR I.

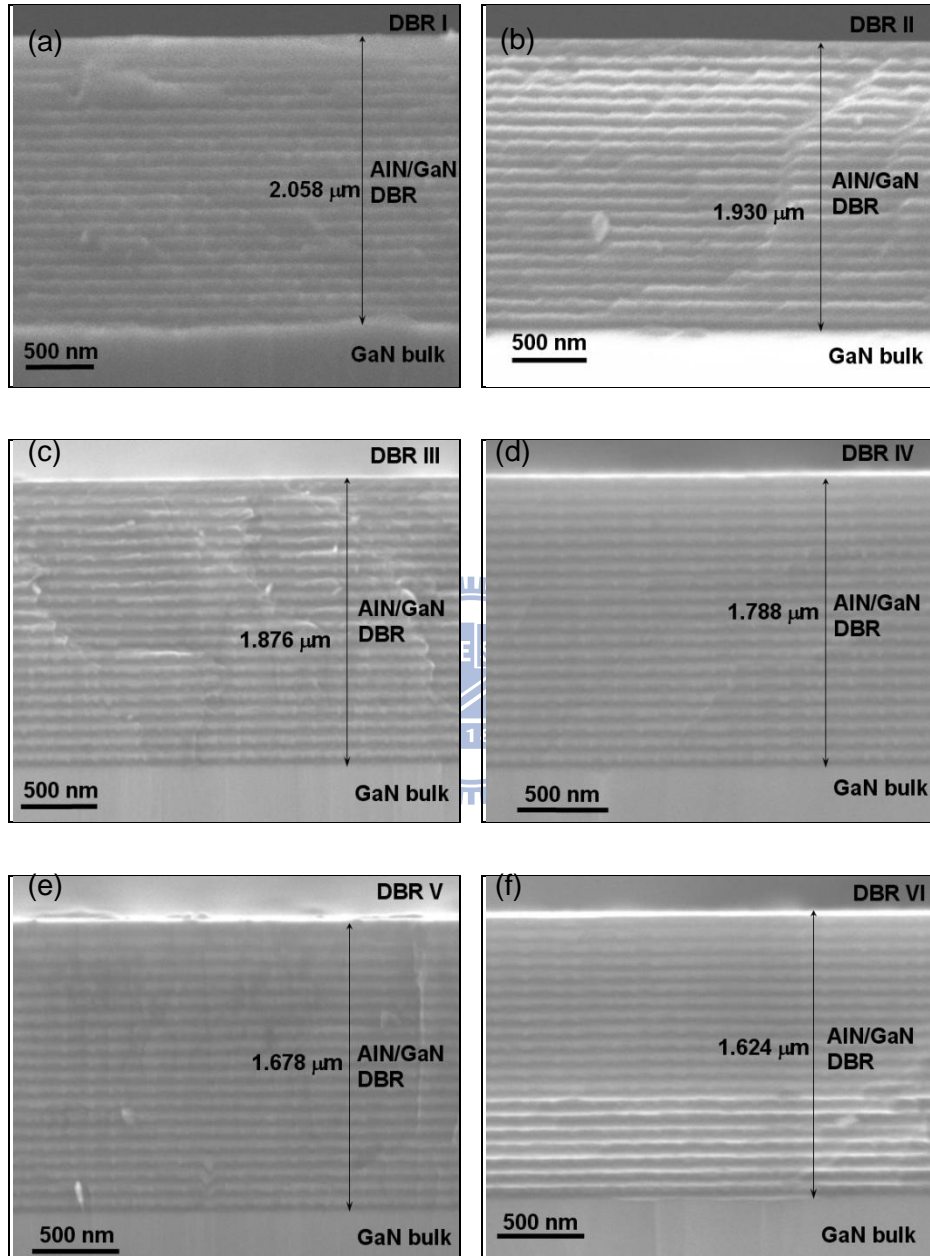


Fig 3.2 Cross-section SEM images of DBRs I-VI.



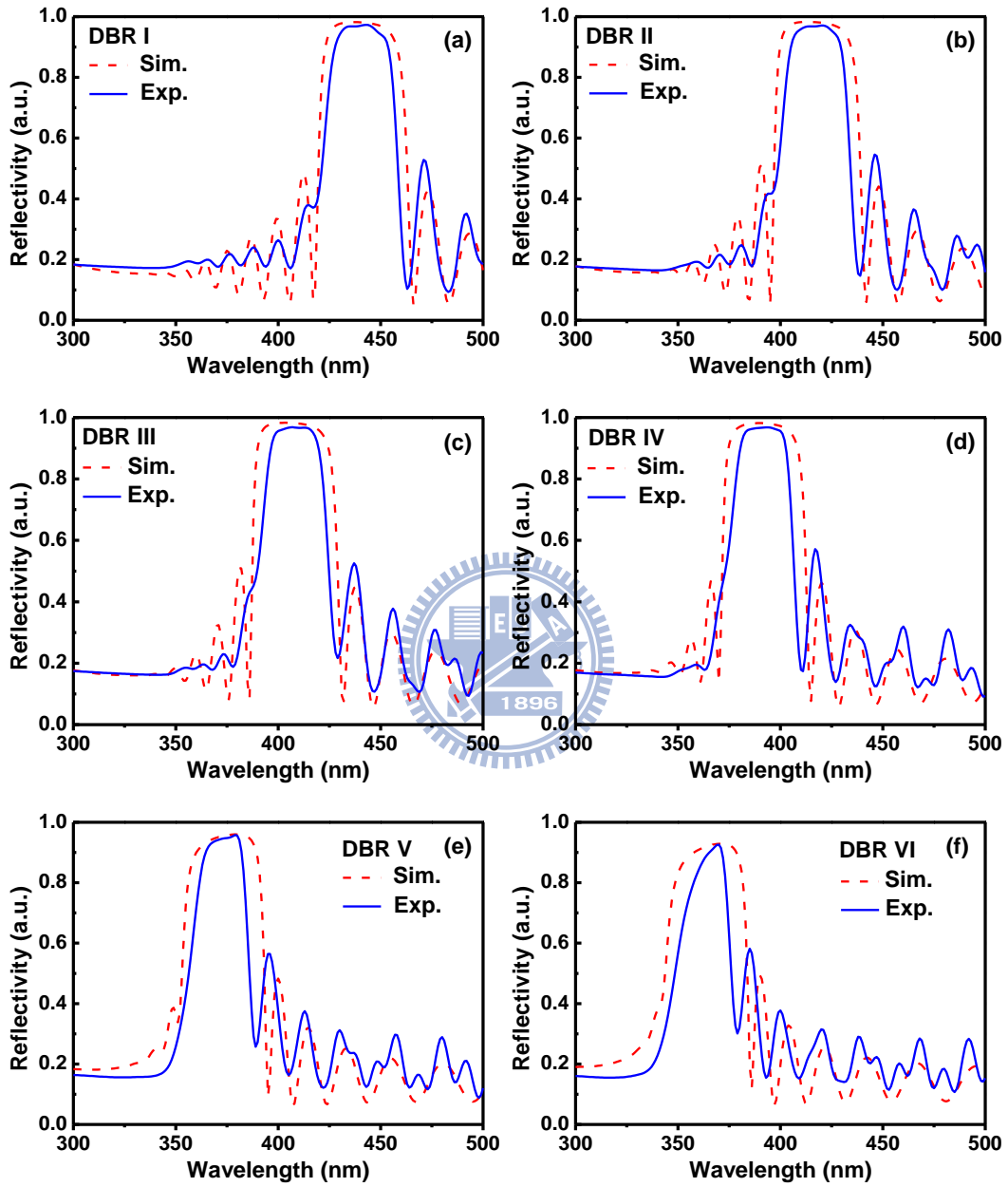


Fig 3.3 Measured (solid) and simulated (dashed) reflectivity spectra of (a) DBR I, (b) DBR II, (c) DBR III, (d) DBR IV, (e) DBR V, and (f) DBR VI.

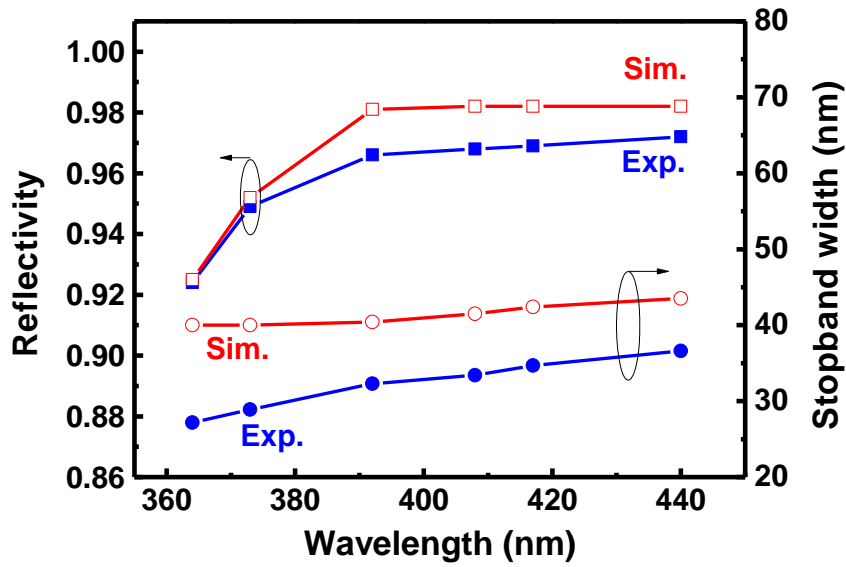


Fig 3.4 Measured and calculated maximum reflectivity values and stopband widths of the DBRs I-VI.

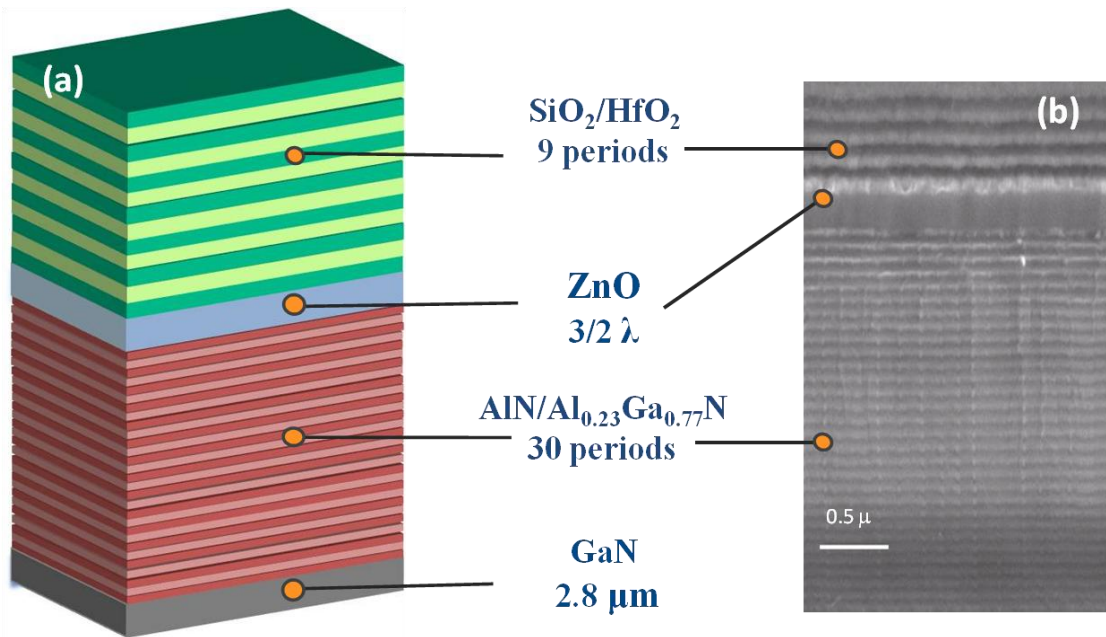


Fig 3.5 (a) Schematic diagram of the ZnO-based hybrid microcavity. (b) The cross section image of the ZnO microcavity with bottom DBRs observed by SEM.

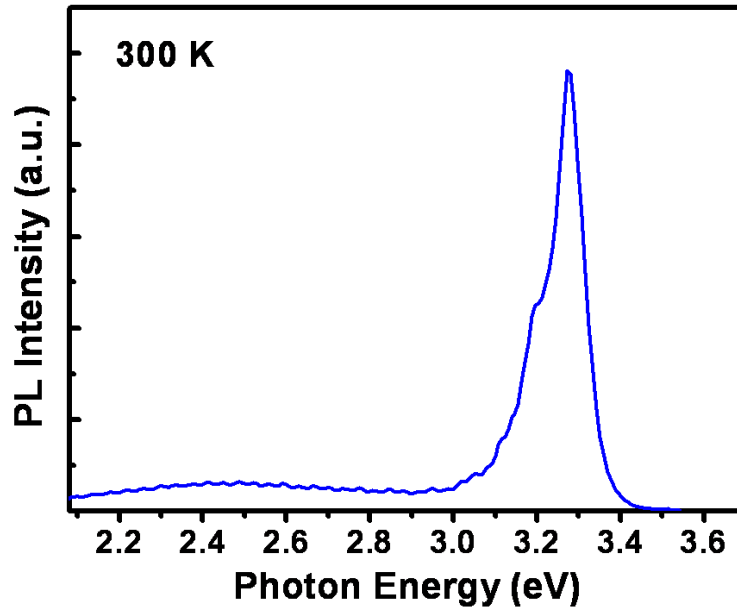


Fig 3.6 RT photoluminescence spectrum from the half-cavity ZnO film grown on AlN/AlGa<sub>N</sub> DBRs.

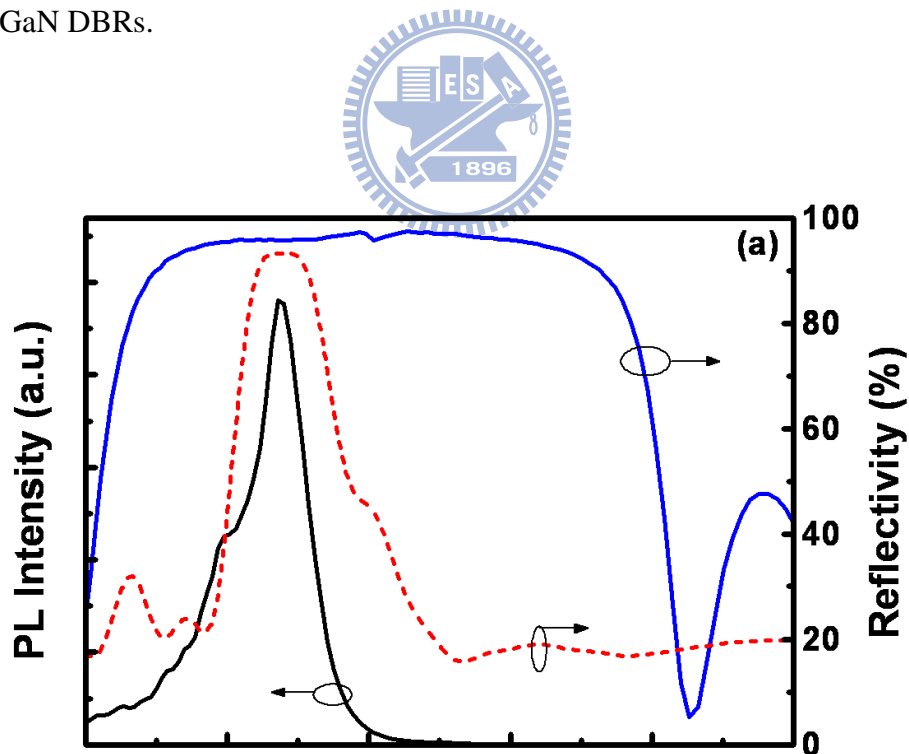


Fig 3.7 RT reflectivity spectra of a 30-pair AlN/Al<sub>0.23</sub>Ga<sub>0.77</sub>N DBR (dashed line) and a 9-pair SiO<sub>2</sub>/HfO<sub>2</sub> DBR (solid line). RT PL spectrum from a half cavity is located within the stop band of the bottom and top DBRs.

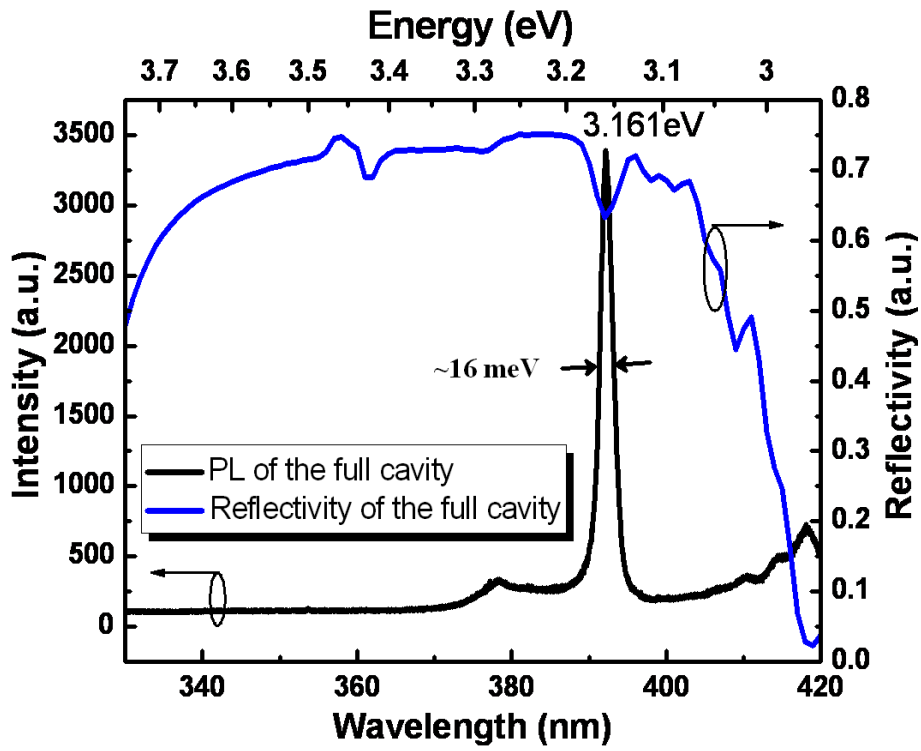
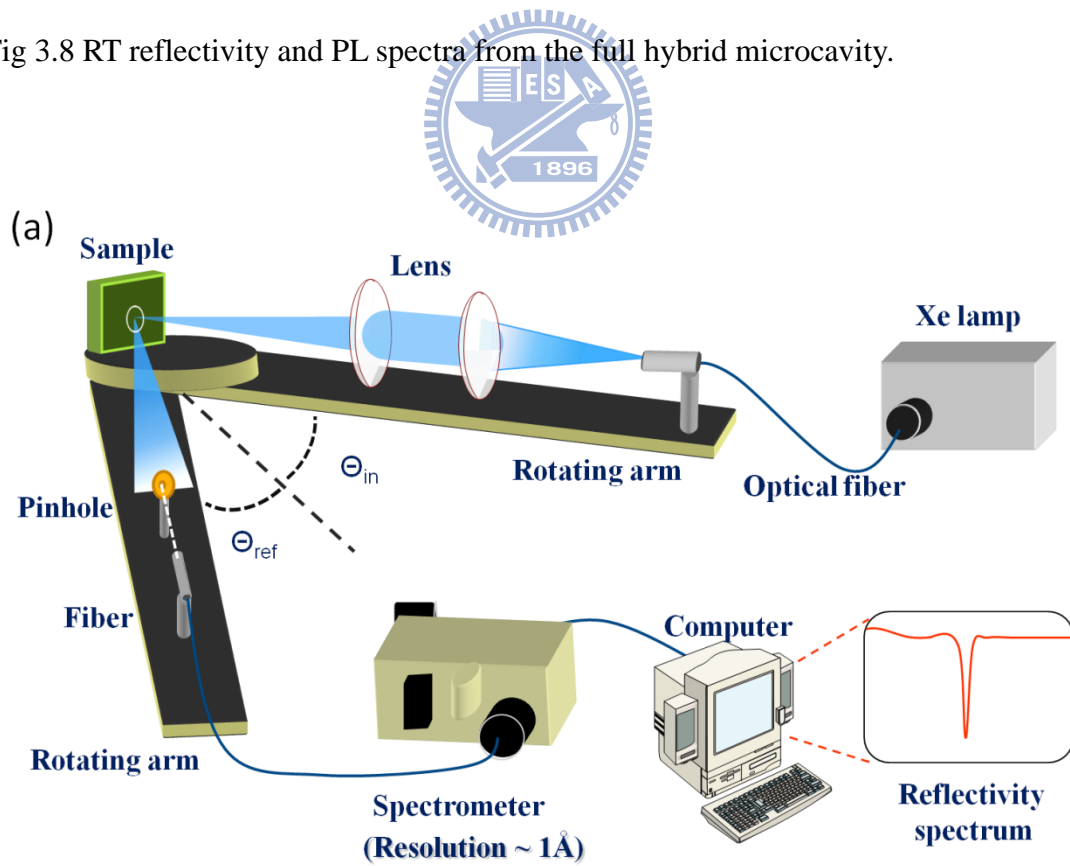


Fig 3.8 RT reflectivity and PL spectra from the full hybrid microcavity.



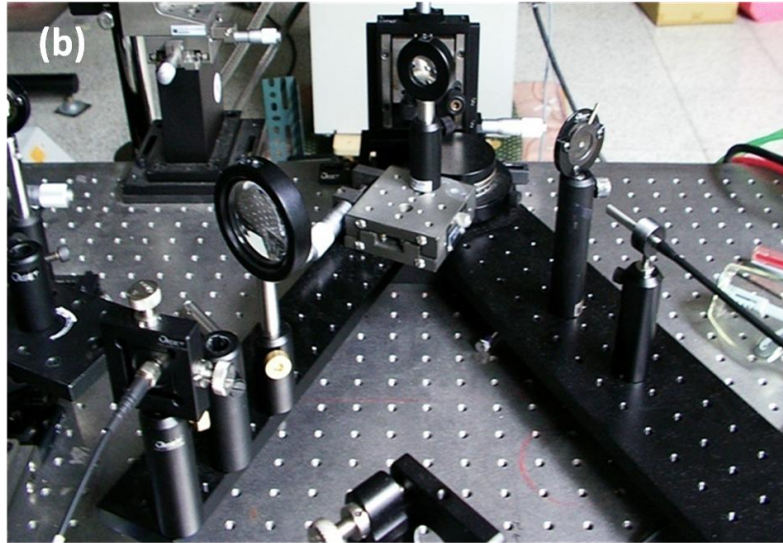


Fig 3.9(a) shows the schematic of experimental setups for measuring reflectance at RT, and (b) is the practical setup for the angle-resolved reflectivity.

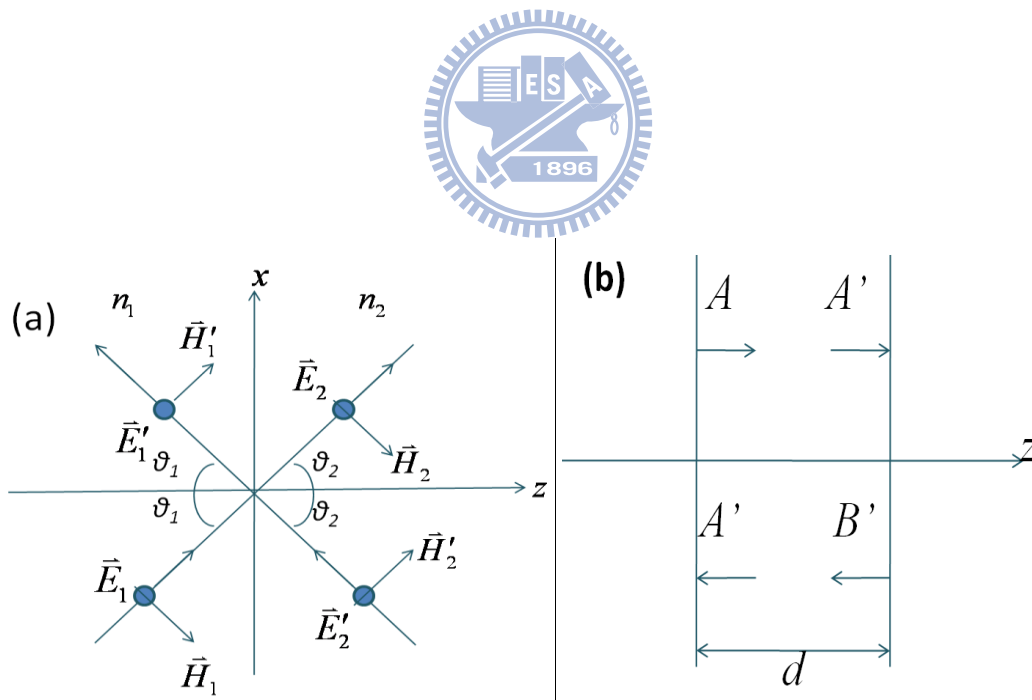


Fig 3.10 The schematic of the calculation for interface matrix and propagation matrix.

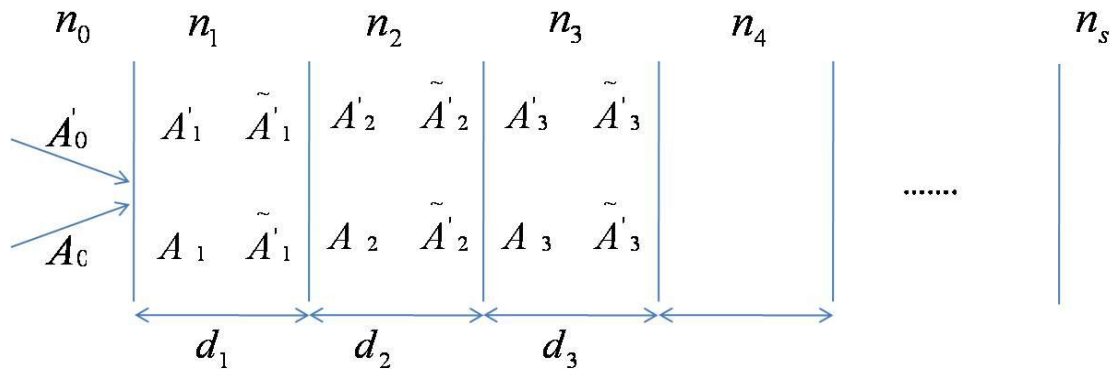


Fig 3.11 The schematic for multilayer structure for transfer matrix

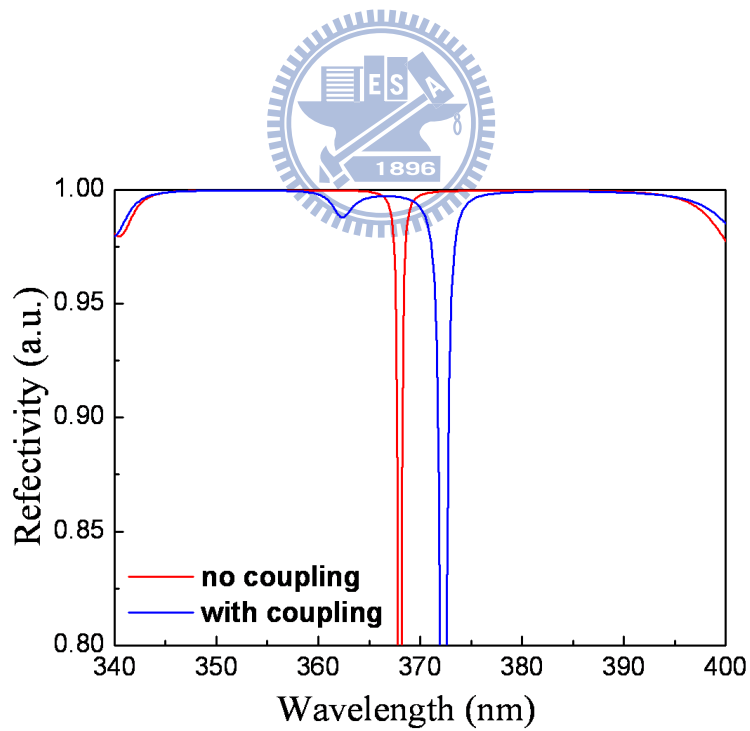


Fig 3.12 The reflectivity of pure cavity mode (red line) and the polariton mode (blue line) in strong coupling regime.

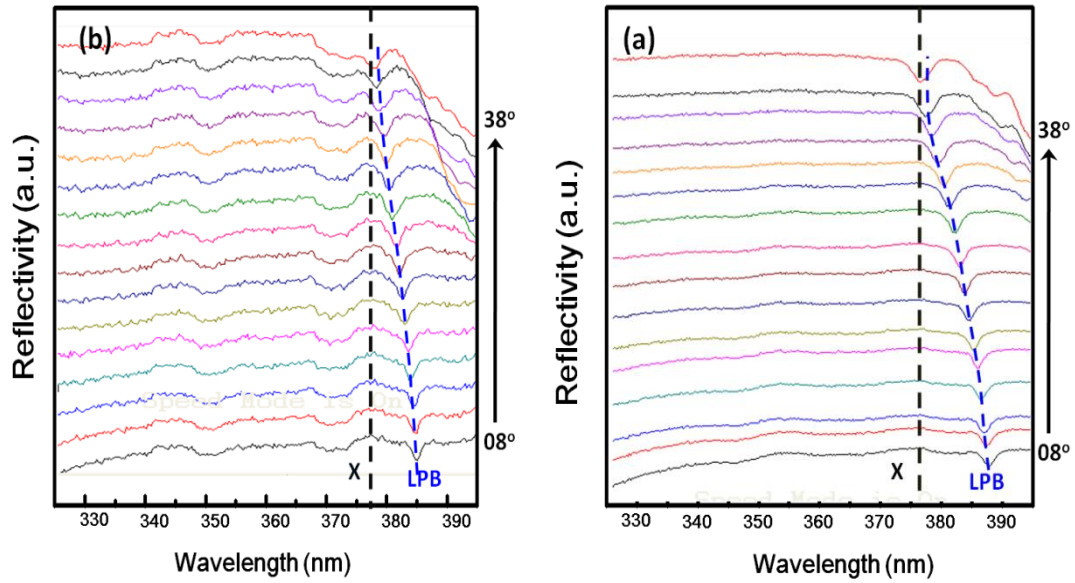


Fig 3.13 RT angle-resolved reflectivity spectra ranging from  $8^\circ$  to  $40^\circ$  for detunings of (a)  $-93$  meV and (b)  $-53$  meV respectively.

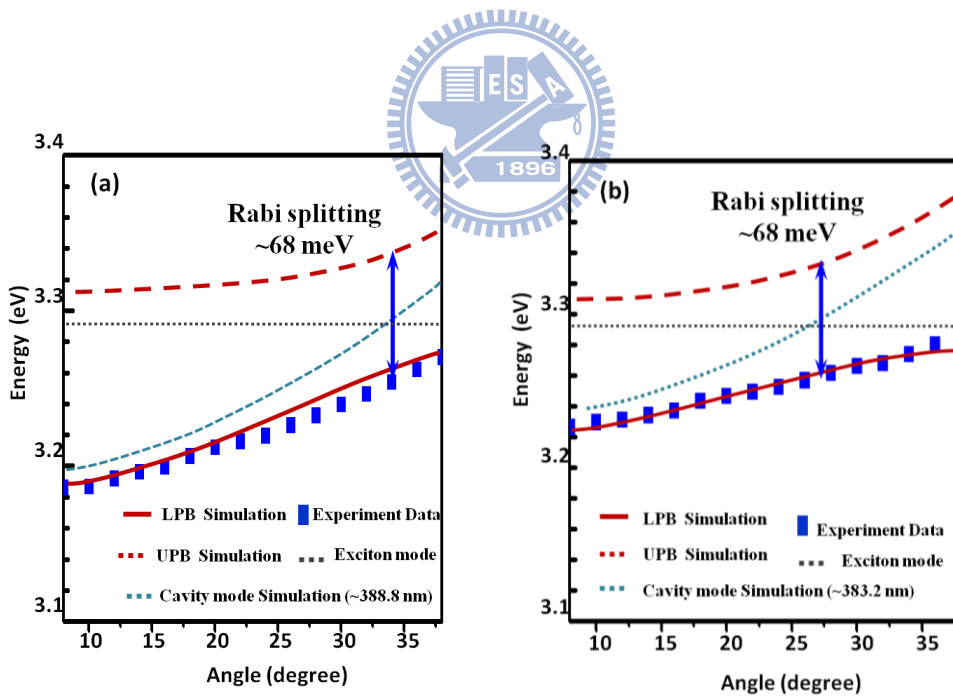


Fig 3.14 RT experimental and theoretical polariton dispersion curves for (a)  $-93$  meV and (b)  $-53$  meV respectively.

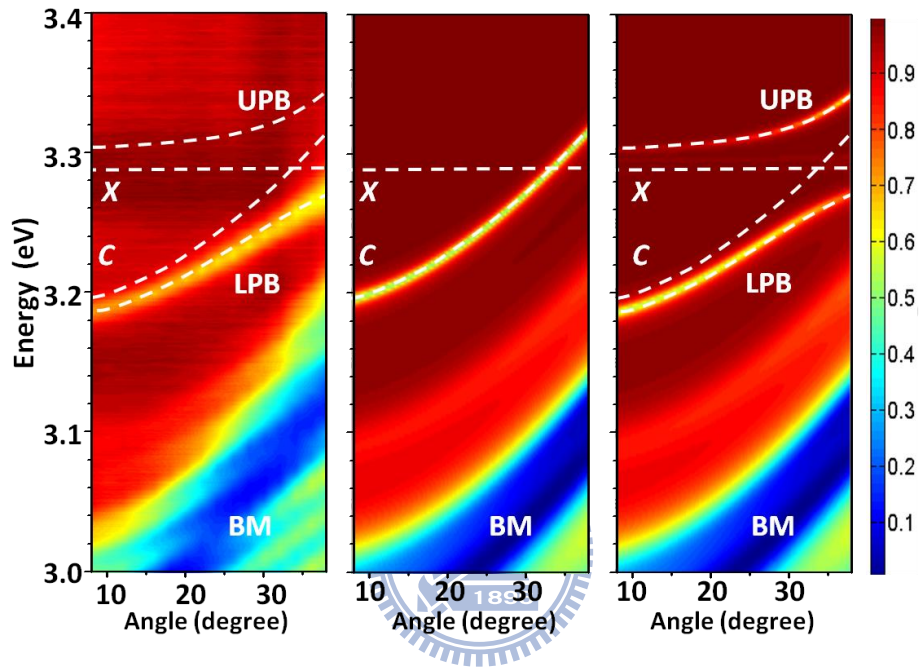


Fig 3.15 (a) The color map of the measured angle-solved reflectivity spectra from  $8^\circ$  to  $38^\circ$  at RT. (b) The color map of the calculated angle-solved reflectivity spectra from  $8^\circ$  to  $38^\circ$  without taking the resonant exciton into account, which shows the pure cavity mode. (c) The color map of the calculated angle-solved reflectivity spectra from  $8^\circ$  to  $38^\circ$  with taking the resonant exciton into account, where X means the exciton mode, C pure cavity mode, UPB upper polariton branch, and LPB lower polariton branch.



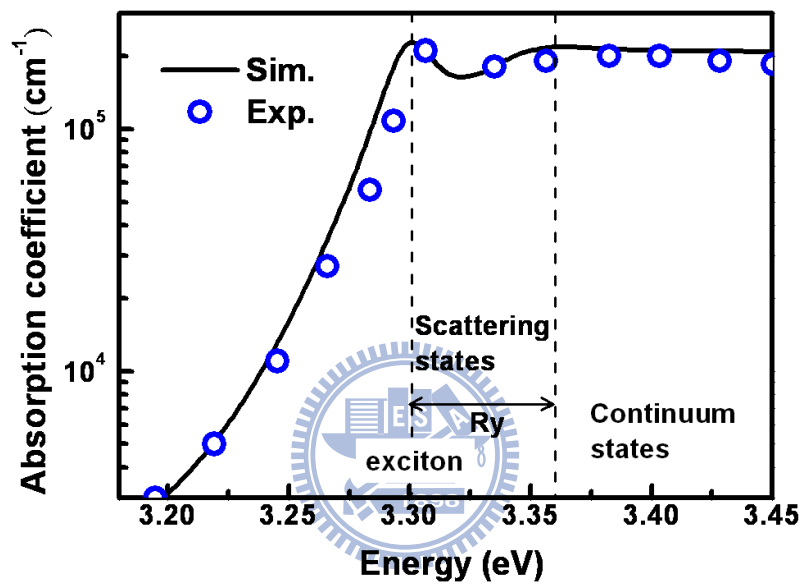


Fig 3.16 Experimental (open blue circle) and simulated (solid line) absorption spectra of a bulk ZnO at RT.

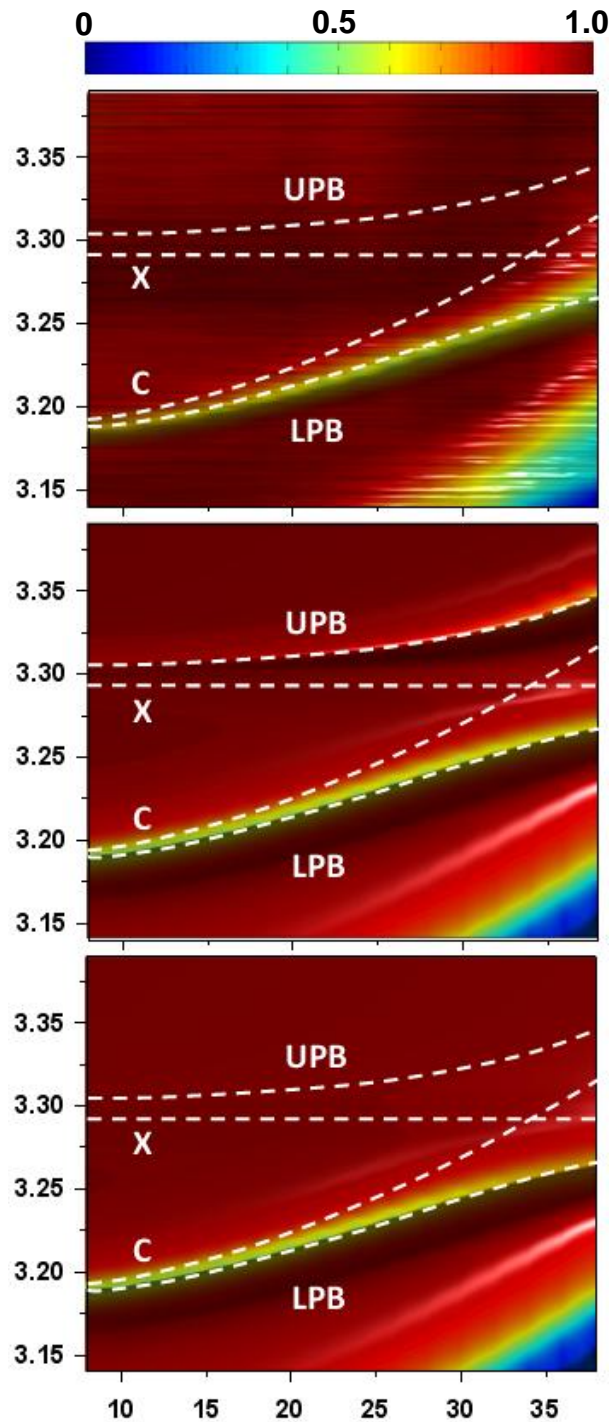


Fig. 3.17 (a) Color map of the angular dispersion of measured reflectivity spectra from 8 to 38° at. (b) Color maps of the calculated angle-resolved reflectivity spectra with taking the resonant exciton into account. (c) Simulation of angle-resolved reflectivity spectra for the bulk ZnO MCs after taking the absorption of scattering states into account.

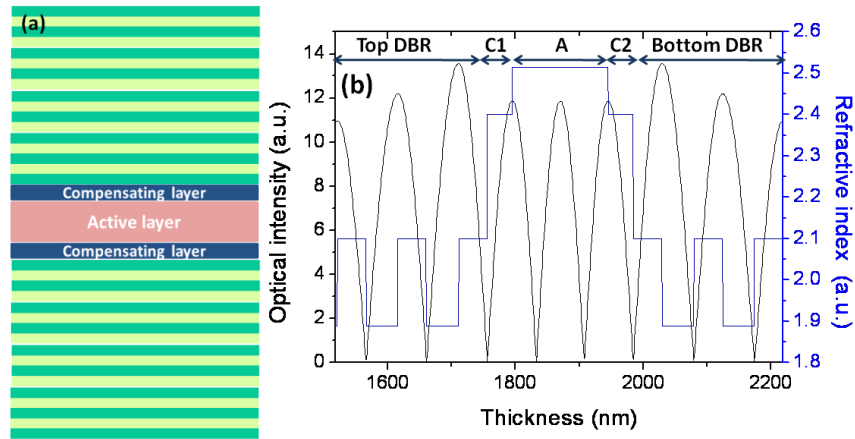


Fig. 3.18 (a) Schematic diagram of the bulk semiconductor microcavity. (b) Refractive index profile and the optical-field intensity in the vertical direction of the microcavity structure. A and C1(C2) represent the active layer and compensating layer, respectively.

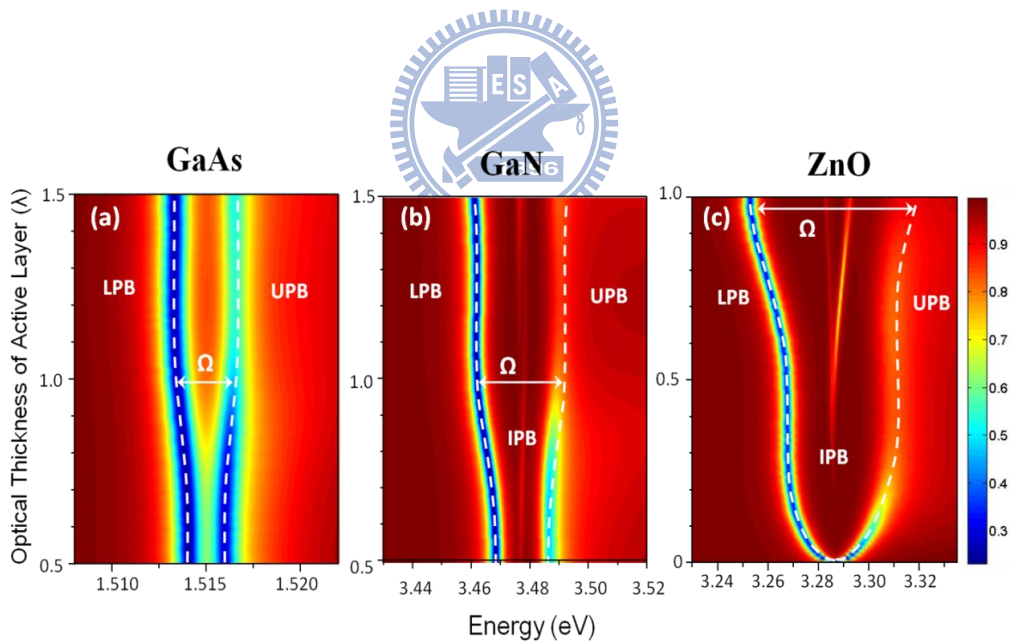


Fig. 3.19 Color maps of calculated reflectivity spectra as a function of active layer thickness for GaAs, GaN, and ZnO MCs at zero detuning and normal incidences. The whit dashed lines show the UPB and LPB without considering exciton scattering absorption.

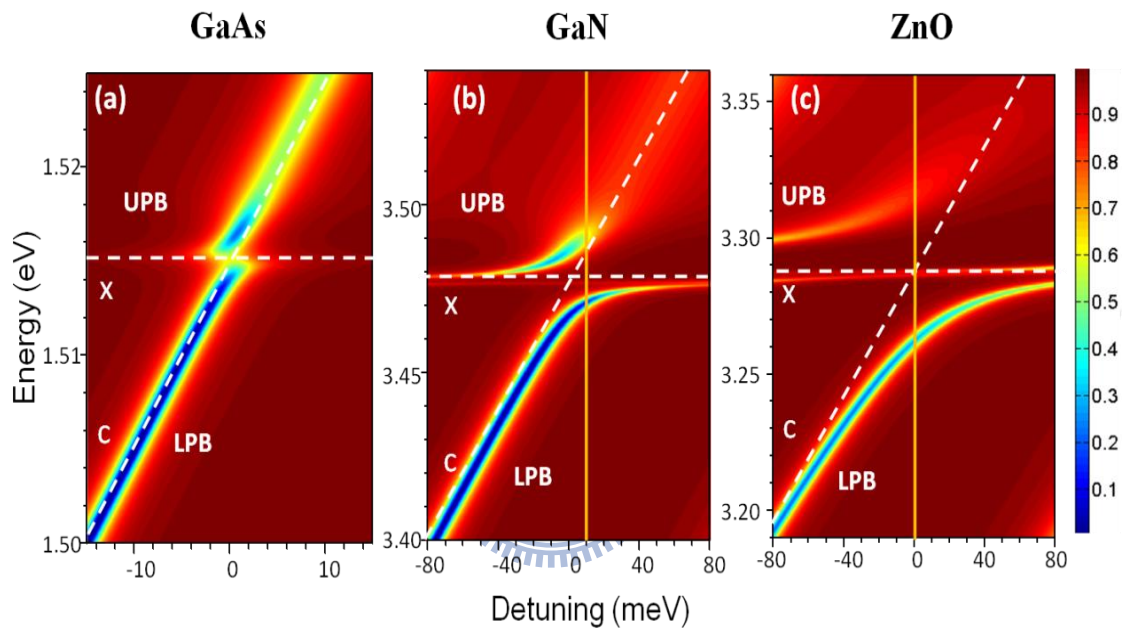


Fig. 3.20 Color maps of calculated reflectivity spectra as a function of exciton-photon detuning for GaAs, GaN, and ZnO MCs with  $\lambda$  active layer thickness at normal incidences. The pure cavity mode  $C$  and uncoupled exciton mode  $X$  are shown (white dashed line). The vertical yellow line represents the critical value of detuning for invisible UPB.

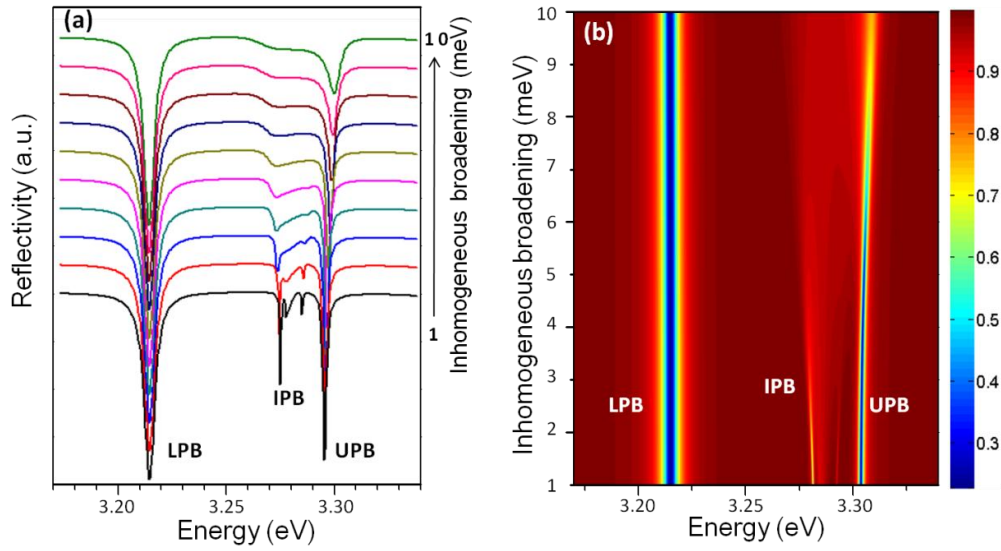


Fig. 3.21 (a) Calculated reflectivity spectra for the  $\lambda$  ZnO cavity at zero detuning and zero in-plane wave vector as varying the inhomogeneous broadening ranging from 1 to 10 meV. (b) Color map of the reflectivity spectra as a function of inhomogeneous broadening.

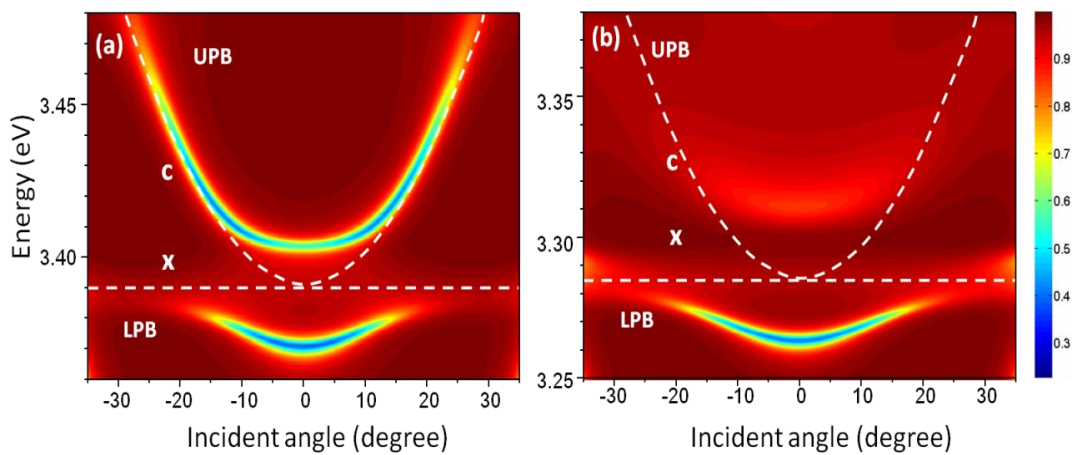


Fig. 3.22 Color maps of the calculated angle-resolved reflectivity spectra of  $0.5\lambda$  (a) MQW ZnO-based MC, (b) bulk ZnO-based MC.

## Chapter 4. Strong coupling regime in electrically pumped InGaN-based microcavity

### 4.1. Introduction

Optical devices based on InGaN quantum wells (QWs) have been actively studied. [76-78] As a result, they are now in practical use as light-emitting diodes and edge emitting laser diodes (LDs). The optical confinement in these devices is achieved by the refractive-index contrast at the interfaces between active and cladding layers in a vertical direction, and between semiconductor and air regions in a horizontal direction. However, these contrasts in III-nitride semiconductors are relatively small compared with those in GaAs/AlGaAs systems. This leads to an increase in the driving current needed for optical devices.

By contrast, another way to reduce the lasing threshold is to use a vertical microcavity structure with high reflectivity DBRs. If the cavity size is of the order of the emission wavelength, the spontaneous emission rate can be controlled and the lasing threshold can be reduced. [79-81] Several groups have reported that they observed the lasing action of III-nitride microcavities with a blue/violet emission when they used optical pumping at RT. [81-85]

The difficulty in the realization of an electrically pumped GaN-based microcavity mainly comes from two factors. First is the requirement of high reflectivity and high quality DBR. The reported DBR structure that is composed of  $\text{Al}_x\text{Ga}_{1-x}\text{N}$  and GaN has a large lattice mismatch and a difference in the thermal

expansion coefficients between these two materials that tend to form cracks in the epitaxially grown DBR structure. These cracks in the DBR could result in the reduction in optical reflectivity and increase in the scattering loss. Moreover, the cracks could also become a current leakage path, making the realization of an effective current injection into GaN microcavities very difficult. The second factor is the need for a high transparency yet good conductivity contact for injection of the carriers into the multiple quantum well (MQW) active region. Since the  $p$  doping of GaN is very difficult, the carrier injection path with low resistance and optical loss is required for efficient current injection.

When strong coupling regime occurs in planar MCs, polariton lasing theoretically predicted several years ago to be achievable which has now been fulfilled experimentally [86-88]. Bose Einstein condensation of polaritons in quasithermal equilibrium at low temperature in GaAs- [89] and CdTe- [90] based structures and at RT in GaN [91] has been demonstrated, showing thresholds 10–100 times better than that for general microcavities, and this kind of laser termed polariton laser (PLSER). Theoretically, the lasing threshold of conventional VCSEL is fixed by the critical conditions required for the population inversion condition to take place, but it is not constrained by for the PLSER. The effective mass of a polariton at the bottom of the lower branch is  $10^8$  times smaller than the typical mass of an atom and  $10^4$  times smaller than the mass of an exciton, which implies the polariton has much higher critical temperatures ( $T_c$ ) than for the other two heavy species. The  $T_c$  is of the

order of a few tens of kelvins in GaAs-based structures and about 100–200 K in CdTe microcavities. It falls close to 500 K for GaN-based cavities with extremely high exciton binding energy and light-matter interaction constant, which, in principle, makes these cavities ideal for making UV polariton laser devices working at RT. Such laser would have a large technological interest, since there is, so far, no demonstration of VCSEL working in the strong coupling regime.

These features are promising for future quantum applications but have up to now only been observed under optical pumping. The next and final step in implementing the fabrication of a polariton laser device is to pass from the optical to the electrical injection. Electrical injection of these entangled light-matter states is a key step toward the implementation of practical, compact devices. So far, electrical injection of cavity polaritons has been reported in organic semiconductors [92] where the coupling strength is very large (Rabi splitting of several hundreds of meV). The drawback of organic microcavities is that the electroluminescence spectra are superposed on emission from the hole-injection diamine derivative (TPD) layer and localized excitonic states that do not strongly couple to cavity photons, restricting severely the purity and efficiency of polaritonic emission. Furthermore, a different type of intersubband polariton has been reported recently in quantum cascade structures [93] along with a demonstration of a mid-infrared polariton quantum cascade LED device. However, the validity of the bosonic description for intersubband polaritons remains to be tested experimentally, raising fundamental



questions about whether it is possible to produce a polariton-based laser. Thus the achievement of the polariton lasing effect under this pumping condition remains a challenging task.

In 2004, T. Tawara et al. [94] observed the cavity polaritons in high-quality InGaN-based microcavities by reflection measurements. The microcavities consisted of InGaN-based quantum well (QW) layers and dielectric DBRs, using the wafer-bonding technique. The InGaN-based QW has a photoluminescence linewidth, i.e., the sum total of homogeneous and inhomogeneous linewidth, of about 200 meV in the as-grown samples. With an InGaN-based QW, it is well known that the Indium composition fluctuates in the QW plane. The light emission from the InGaN-based QW originates from the localized excitons in the Indium rich regions and this leads to inhomogeneous spectral broadening [95-97]. When the localized excitons in an InGaN-based QW have discrete energy states such as quantum dots, only those excitons whose energy matches the cavity resonant energy are picked out by the cavity filter effect. Of these localized excitons, only those whose energies are resonant with the cavity mode contribute Rabi splitting. In the InGaN-based QW microcavities the localized excitons with large oscillator strengths at certain discrete energy levels enabled us to observe the Rabi splitting. The anticrossing behavior of strong exciton-photon coupling had been represented with a vacuum-field Rabi splitting of 6 meV at RT, and this strong coupling is further enhanced with a Rabi splitting of 17 meV by increasing the integrated oscillator strength coupled to the cavity mode.

Inspiringly, in our study, we go a step further to demonstrate the strong coupling regime in InGaN/GaN quantum well in the current injection microcavity.

#### 4.2. InGaN/GaN multi quantum well microcavity structure

Fig. 4.1 shows the schematic of the hybrid microcavity GaN VCSEL structure. The device fabrication steps are as follows: first, the MOCVD reactor was used to grow the device epitaxial structure. The epitaxial structure mainly consists of a 29-pair AlN/GaN DBR and a  $5\lambda$  (our target wavelength is  $\lambda=460\text{ nm}$ ) optical thickness microcavity composed of a 790-nm-thick Si-doped n-type GaN, ten pairs of In<sub>0.2</sub>Ga<sub>0.8</sub>N (2.5 nm)/GaN (7.5 nm) MQWs, and a 120-nm-thick Mg-doped p-type GaN layer. The MQWs were located at the antinode of light field in the microcavity for enhancing the coupling of photons and the cavity mode. To obtain a crack-free and high reflectivity AlN/GaN DBR, we insert the AlN/GaN superlattices into the AlN/GaN DBR structure during the epitaxial growth to reduce the biaxial tensile strain in AlN/GaN DBR. The superlattice has 5.5 pairs of AlN/GaN corresponding to a half-wavelength stack and was inserted in every four pairs of AlN/GaN quarter wavelength stacks to form a 29-pair AlN/GaN bottom DBR. The grown DBR showed a high peak reflectivity of R=99.4% with a spectral bandwidth of ~25 nm. The epitaxially grown structure was then processed to form the intra-cavity coplanar p and n contacts for current injection. A 0.2  $\mu\text{m}$ -thick SiN<sub>x</sub> layer was used to form a current injection and a light emitting aperture of 30  $\mu\text{m}$  in diameter. An ITO was deposited

on top of the aperture to serve as the transparent contact layer. The deposited ITO has a measured transmittance of about 98.6% at  $\lambda=460$  nm. Finally, an eight-pair  $\text{Ta}_2\text{O}_5/\text{SiO}_2$  dielectric DBR measured reflectivity of about 99% at  $\lambda=460$  nm was deposited as the top DBR mirror to complete the full hybrid microcavity VCSEL device.

### 4.3. Electroluminescence setup and principle

A set of instruments for the electroluminescence setup including current source Kiethley 238, a microscope to observe the patterned electrode of sample surface, three axial stages for probe and fiber to detect the light output, and a cryostat for the cooling system which use the liquid helium to cooling the chamber. The sample surface image could be received by CCD and observed on the CRT screen, and then the light detected by a  $0.32 \mu\text{m}$  monochromator (Jobin-Yvon Triax-320) with 1800, 1200, and 300 grooves/mm grating. And all the samples were placed in the closed-cycle cryostat with a temperature controller ranging from 77 K (Liquid helium) to RT. Fig. 4.2 shows the schematic of low temperature electroluminescence.

## 4.4. Experimental results

### 4.4.1. Temperature-dependent electroluminescence

The demonstration of the strong coupling regime in a variety of semiconductor systems via measurements of reflectivity, transmission, or photo- or electroluminescence involves the ability to tune either of the excitonic and cavity

mode resonances with respect to the other, showing the characteristic anticrossing between the two modes. To study polariton emission properties of our InGaN/GaN microcavity device under electrical injection, we used both temperature and angular tuning measurements to prove that emission arises truly from polariton states.

Through the temperature controller, we employ the temperature-dependent electroluminescence to improve the anti-crossing phenomenon for strong coupling regime. The corresponding cavity mode energy shift is due to the change of the refractive index and is much weaker (about-0.10 meV K<sup>-1</sup> at 180 K) [98] than the emission energy of the quantum well excitons follows the temperature dependence of the In<sub>0.2</sub>Ga<sub>0.8</sub>N bandgap by the fitting formula given by [99]

$$E(T) = E_m(0) - \frac{\alpha T^2}{T + \beta} - \frac{\sigma}{k_B T} \quad (4.4-1)$$

where  $E(T)$  is the emission energy at  $T$ , the third term comes from the localization effect, in which  $s$  is related with localization effect, and  $k_b$  is the Boltzmann constant. The value of  $s$  gives an estimate of the degree of localization effect. That is, if the value is larger, the localization effect is stronger. In our work, the simulation parameters of  $\alpha$  is 0.635 (meVK<sup>-1</sup>),  $\beta$  1000K, and  $\sigma$  17.5 meV.

Fig 4.3 (a) shows a series of electroluminescence spectra from microcavity polariton emission for different temperatures between 180 and 300 K, collected at zero-degree angle, and the Fig 4.3 (b) shows the corresponding mapping. The emission at 180 K consists of a high energy quantum well exciton line X at 3.028 eV and a low energy cavity mode line C at 3.022 eV. The increase of the sample's

temperature by 120 K tunes the exciton energy by 18.6 meV down to 3.0102 eV, and the cavity mode by 12 meV down to 3.01 eV. Notably, at 280 K the low energy line has transformed into excitonic emission whereas the high energy line has transformed into cavity mode emission. The exciton and cavity modes are resolved over the entire temperature range, and exhibit the characteristic anticrossing behavior of the strong coupling regime. This shows that electroluminescence in this intermediate temperature range arises unambiguously from exciton polariton states in the strong coupling regime, which is demonstrated for the first time in electrically pumped InGaN/GaN microcavities.

To shed more light on the dispersive features of the two polariton branches, in the InGaN/GaN microcavity, we employ the above-mentioned simulation approach to improve the strong coupling regime. The simulation of temperature-dependent spectra is shown in Fig 4.3 (c) ranging from 180 K to 300 K, and the Fig 4.3 (d) presents the simulation mapping corresponding to Fig 4.3 (c). In the model, we employ the similar temperature-dependent exciton mode and cavity mode corresponding the experimental results and the homogeneous broadening is about 15 meV. Moreover, the oscillator strength of InGaN/GaN quantum well is  $0.0289 \text{ eV}^2$  per quantum well, which is the same order as GaN bulk microcavity. Fig 4.3 (c)(d) demonstrate an excellent fit of the upper and lower polariton branches is obtained by applying a coupled harmonic oscillator model to our data. Small deviations from experiment could be well understood by considering that no dependence of exciton oscillator

strength on temperature has been included in the model. The fits reveal that the condition of zero exciton-photon detuning at zero angle is reached at a temperature of 280K with a normal mode Rabi splitting of 6.5 meV, in good agreement with the simulation results.

In our experiment of temperature-dependent electroluminescence, it should be noted that the current injection is 2 mA, and the InGaN-based microcavity we employed is with current aperture of 30  $\mu\text{m}$ . To estimate the carrier density, we assume that all injected carriers are trapped into the quantum well. This hypothesis is supported by the absence of InGaN emission and by the linear dependence of the total electroluminescence intensity with current intensity, indicating that nonradiative processes can be neglected. As a result, the total electron-hole pair density  $n$  can be directly deduced from the current density, the same way as it is usually deduced from the excitation power under optical pumping. Thus,  $n = j\tau/e$ , where  $e$  is the electron charge,  $j$  the current density, and  $\tau$  averaged recombination time (about 200~400 ps ) [100] in such sample. For  $I=2$  mA, the estimated value of the polariton density is of the order of  $n$  about  $7.36 \times 10^{18} \text{ cm}^{-3}$  which is about which is much smaller than the InGaN/GaN QWs Mott density ( $\sim 2.89 \times 10^{19} \text{ cm}^{-3}$ ) [101]. Furthermore, the exciton binding energy of the InGaN/ GaN QWs is about 25 meV, so we can make sure that the InGaN-based microcavity is operated in the strong coupling regime with 2 mA injection current at RT.

#### 4.4.2. Angle-resolved electroluminescence

To further confirm the strong coupling regime in InGaN/GaN microcavity, we employ another approach to demonstrate the anticrossing dispersion curve in electroluminescence. Angle-resolved electroluminescence measurements were performed in a temperature-controlled, closed-cycle, electrically wired liquid helium cryostat. The light was collected through an optical fiber mounted on one of the axis stage. In the angle-resolved electroluminescence setup, we remove the axial stages of collection fiber to replace turning the light collection angle owing to the instrument restriction. Via the placement of the fiber stage, the fiber collection angle can be estimated

$$\theta = \tan\left(\frac{x}{d}\right)$$



(4.4-1)

where  $x$  is the fiber stage displacement, and  $d$  is the distance between fiber and sample.

Evidence of the strong coupling regime is obtained by monitoring the electroluminescence spectra as a function of the emission angle. Fig 4.4(a) summarizes the emission spectra measured under moderate injection conditions (current intensity  $I=2$  mA), which corresponds to the same carrier density as temperature dependent electroluminescence in section 4.4.1. Fig 4.4(b) shows the corresponding color map of angle resolved electroluminescence ranging from  $0^\circ$  to  $13^\circ$  at 180K. The cavity-exciton detuning is about -6.4 meV, and both polariton branches are clearly evidenced with the characteristic s-shape of the lower branch. Fig

4.4 (c) and (d) present the transmittance spectra and corresponding map from the simulated transmittance calculated by transfer matrix simulation, and it is in good agreement in experiment results. The Rabi-splitting value is estimated about 7meV at 7.4 degree which larger than the one measured at 280 K, which results from the homogeneous broadening due to higher temperature. These consequences further confirm the strong coupling regime in the current injection InGaN-based microcavity device.

#### 4.4.3. Current-dependent electroluminescence

A legitimate question to ask is whether increasing injection density will lead to polariton lasing or to a collapse of the strong coupling regime and transition to conventional VCSEL operation. Theoretically, in high injection density regime, excitons are bleached by the screening of the Coulomb interaction and phase space filling: the optical properties are therefore dominated by the recombination of uncorrelated electron-hole pairs. This continuum of unbound electron-hole pairs is in the weak coupling regime with the cavity mode, and the emission is simply filtered by the cavity mode. Thus the transition from the strong coupling to the weak coupling regime when increasing the density of electrically injected electrons and holes.

We resort to a current-dependent electroluminescence on the same InGaN-based microcavity device, which exhibits the zero-detuning condition in the normal direction at 240 K, and the injection is improved at higher operation temperatures



because of the lower series resistance of the p-type DBR. In Fig. 5(a), electroluminescence spectra are shown as a function of injection current. At low injection currents, two clearly resolved polariton peaks are evident. With increasing injection current, the two polariton peaks progressively merge together but not transform into totally a single emission line due to the current tolerance of the InGaN-based microcavity device. Furthermore, we estimate that at the maximum current injection of 4 mA in our experiments an estimated density of  $1.47 \times 10^{19}$  polaritons  $\text{cm}^{-3}$  are injected per quantum well. Although this density is near exciton Mott density, the Rabi-splitting is still obvious due to the carrier density is evaluated by stricter assumptions. Fig 5(b) shows the Rabi-splitting reduces from 7.2 meV to 5.4 meV with the increment of current injection from 0.5 mA to 4 mA, which contributes to the homogeneous broadening increment owing to the more exciton-exciton scatterings.

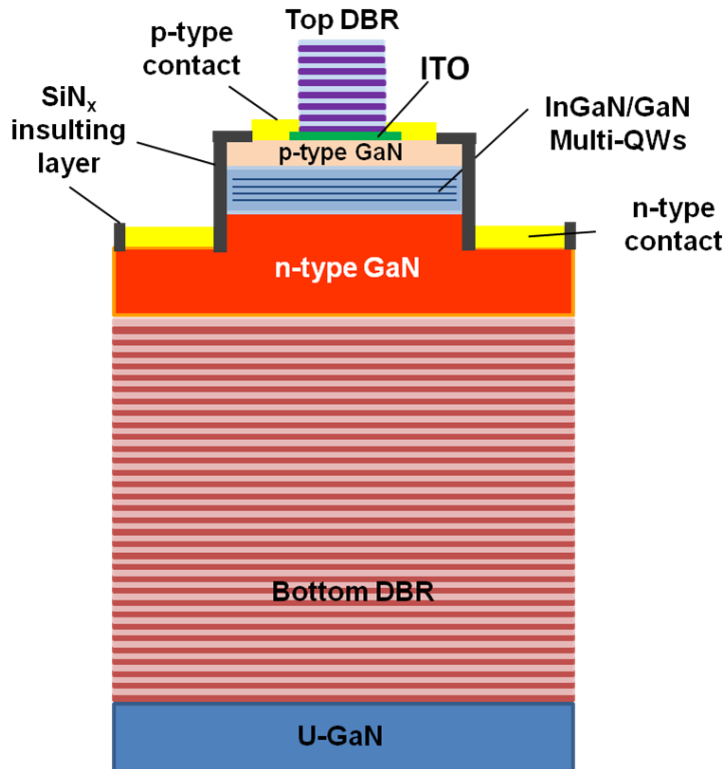


Fig 4.1 Schematic diagram of completed electrical pumped InGaN-based microcavity.

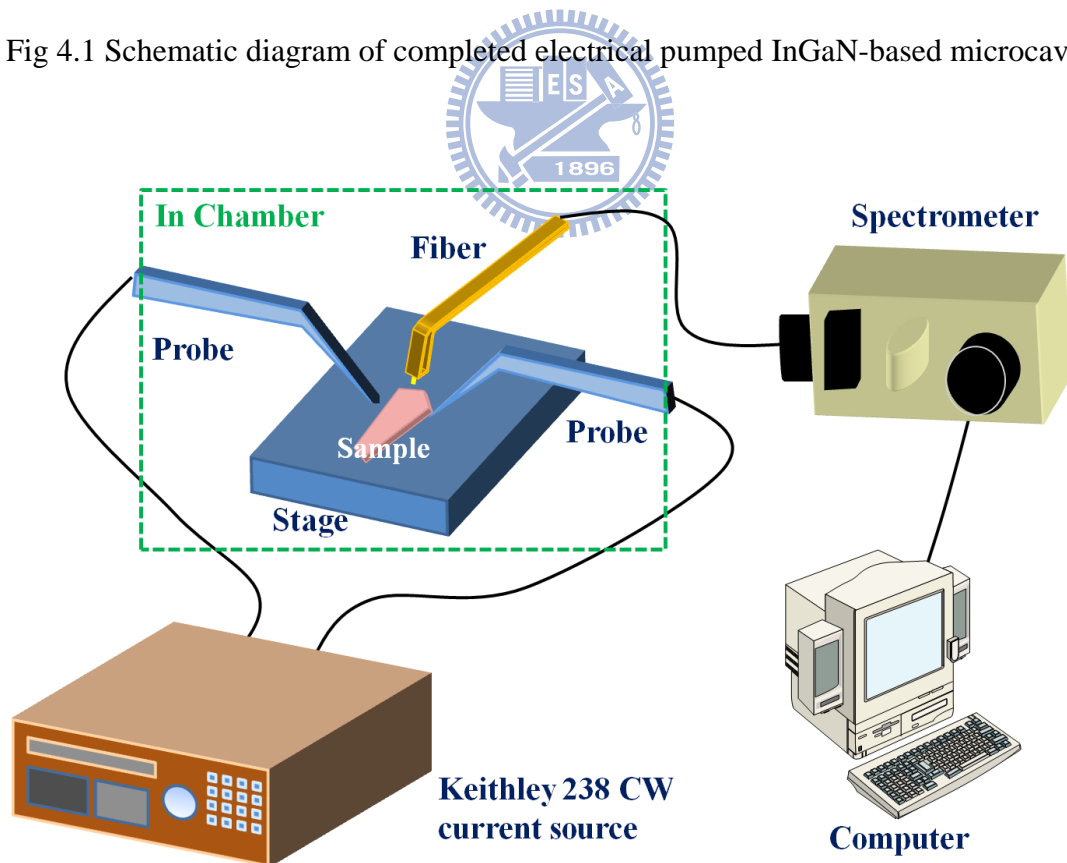


Fig 4.2 Schematic of experimental setup for low temperature electroluminescence.

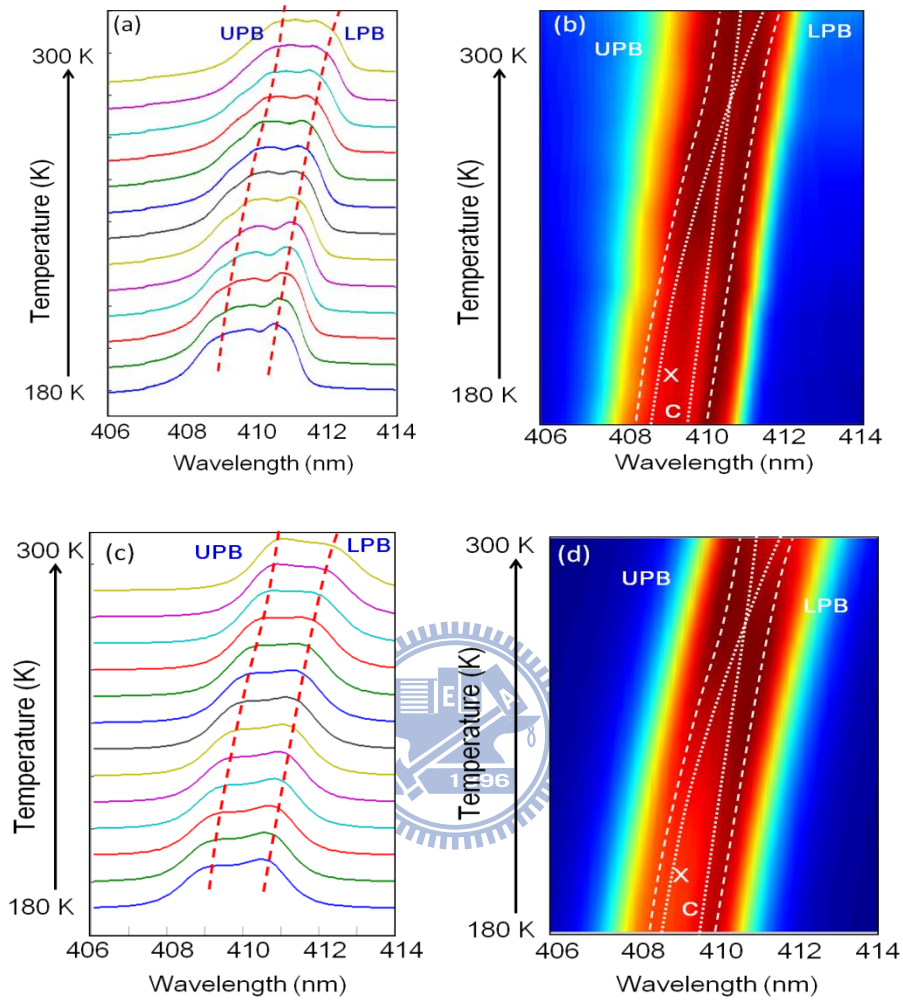


Fig. 4.3 (a) Series of electroluminescence spectra from InGaN-based microcavity polariton emission for different temperatures between 180 K and 300 K (b) Corresponding color map of electroluminescence spectra ranging from 180 K to 300 K (c) Transmittance spectra simulation of temperature-dependent transmittance spectra from 180 to 300 K (d) Color map of transmittance spectra ranging from 180 K to 300 K

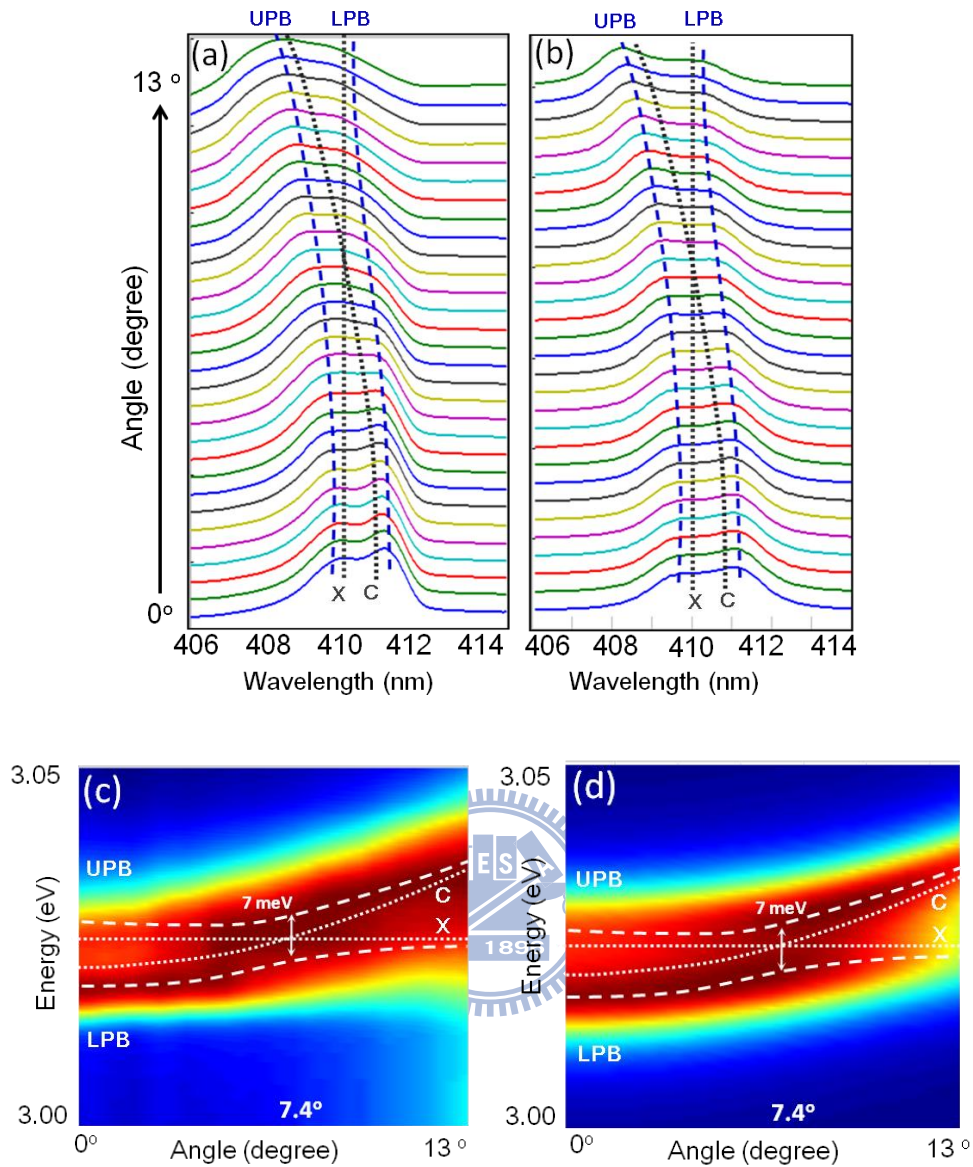


Fig. 4.4 (a) Series of electroluminescence spectra from InGaN-based microcavity polariton emission for different angle ranging from  $0^\circ$  and  $13^\circ$  (b) The simulation of angle-resolved spectra ranging from  $0^\circ$  and  $13^\circ$ . (c) Color map of electroluminescence spectra from InGaN-based microcavity polariton emission for different angle ranging from  $0^\circ$  and  $13^\circ$  (d) Color map of simulated angle-resolved spectra ranging from  $0^\circ$  and  $13^\circ$

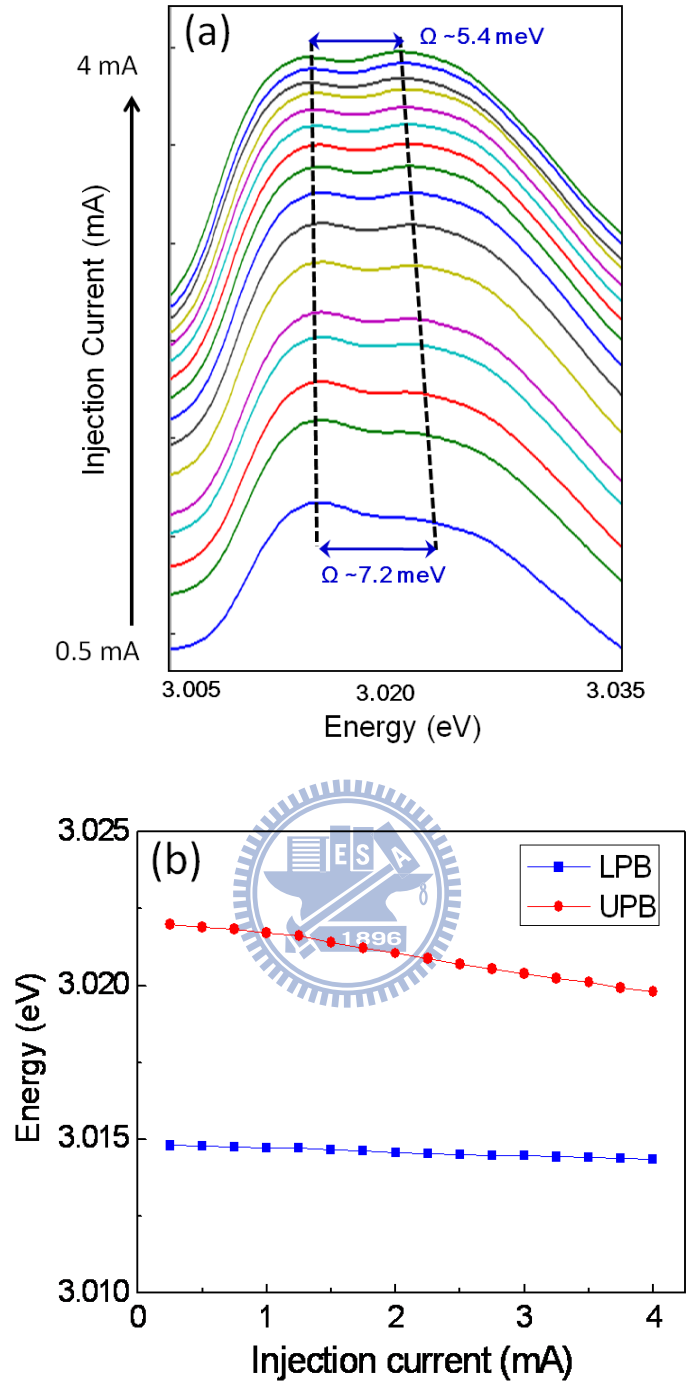


Fig. 4.5 (a) Series of electroluminescence spectra are shown as a function of injection current ranging from 0.5 mA to 4 mA. (b) Extracted lower (blue square) and upper (red square) polariton peaks with various injection current.

## Chapter 5. Conclusion

In conclusion, the strong exciton-photon coupling at RT in bulk ZnO-based hybrid MCs has been demonstrated according to the excellent agreement between experimental and theoretical angle-resolved reflectivity spectra. The large vacuum Rabi splitting of the order of 68 meV is achieved in the ZnO MCs at RT. Furthermore, it is found that the UPB could not be experimentally probed in the thick bulk ZnO MCs since the Rabi splitting energy is larger than the exciton binding energy, pushing the UPB into the energies of scattering absorption.

Furthermore, we have presented the numerical simulation about the investigation of different physical mechanisms inducing the broadening of UPB in semiconductor MCs based on three different materials. According to the simulation results, the UPBs of the GaN- and ZnO-based MCs will become indistinct when the thickness of optical cavity is larger than  $\lambda$  and  $0.25\lambda$  respectively. The invisible UPBs are mainly dominated by the product of the absorption coefficient and the active layer thickness. Furthermore, it is preferred to probe a visible UPB in the case of negative exciton-photon detuning since the UPB in positive detuning is photon-like and induces decoherence by exciton scattering states, especially for wide-bandgap MCs. There is still a clear UPB in GaAs-based MC with thick bulk active layer due to the smaller absorption coefficient than that in wide-bandgap materials. In addition to the active layer thickness and exciton-photon detuning impact on the broadening of UPBs, the inhomogeneous broadening induced by crystal imperfection would also be an

important factor causing the invisible UPB in wide-bandgap semiconductor MCs. We as well as demonstrated the potential for MQW ZnO-based MCs to improve the visibility of UPB due to the large 2D exciton binding energy and the small product of absorption coefficient and active layer thickness. Therefore, the employment of MQW ZnO-based MCs and the improvement of wide-bandgap material quality will be necessary to observe well-define strong coupling regime and even to achieve low-threshold polariton devices.

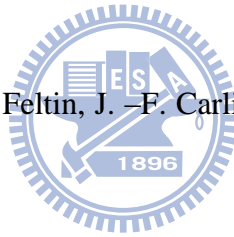
In the last, we present the strong coupling regime in 10 pairs of InGaN/GaN InGaN-based electrically driven microcavity. The results of temperature-dependent electroluminescence show the Rabi-splitting of 6meV at 280K with 2-mA current injection. Furthermore, the angle-resolved electroluminescence spectra show the anti-crossing characteristic at 180 K with Rabi-splitting of 7 meV at 7.4 degree. The both experiments are in good agreement with the simulation results employed by transfer matrix and dipole oscillator model. In the last, Rabi-splitting value decreases from 7.2 meV to 5.4 meV with the increase of carrier density, which resulting from the homogeneous broadening increment owing to more exciton-exciton scatterings

## Reference

- [1]. Hall, R. N., Fenner, G. E., Kingsley, J. D., Soltys, T. J. and Carlson, R. O. *Phys. Rev. Lett.*, Vol. 9, 366. (1962)
- [2]. Nathan, M., Dumke, W. P., Burns, G., F. H. Dill, J. and Lasher, G. *Appl. Phys. Lett.*, vol. 1, 62 (1962)
- [3]. Quist, T. M., Rediker, R. H., Keyes, R. J., Krag, W. E., Lax, B., McWhorter, A. L. and Zeigler, H. J. *Appl. Phys. Lett.* vol. 1, 91, (1962).
- [4]. Kroemer, H., *Proc. IEEE*, vol.51 1782,(1963)
- [5]. C. Weisbuch, M. Nishioka, A. Ishikawa, Y. Arakawa, *Phys. Rev. Lett.* 69, 3314 (1992)
- [6]. Brune, M., Schmidt-Kaler, F., Maali, A., Dreyer, J., Hagley, E., Raimond, J. M. and Haroche, S. (1996). *Phys. Rev. Lett.* 76, 1800.
- [7]. J. Kasprzak, M. Richard, S. Kundermann, A. Baas, P. Jeambrun, J.M.J. Keeling, F.M. Marchetti, M.H. Szymańska, R. André, J.L. Staehli, V. Savona, P.B. Littlewood, B. Deveaud, L.S. Dang, *Nature* 443, 409 (2006)
- [8]. R. Balili, V. Hartwell, D. Snoke, L. Pfeiffer, K. West, *Science* 316, 1007 (2007)
- [9]. M. Saba, C. Ciuti, J. Bloch, V. Thierry-Mieg, R. André, L.S. Dang, S. Kundermann, A. Mura, G. Bongiovanni, J.L. Staehli, B. Deveaud, *Nature* 414, 731 (2001)
- [10]. K.J. Vahala, *Nature (London)* 424, 839 (2003)



- [11].S.I. Tsintzos, N.T. Pelekanos, G. Konstantinidis, Z. Hatzopoulos, P.G. Savvidis,  
Nature 453, 372 (2008)
- [12].D. Bajoni, E. Semenova, A. Lemaître, S. Bouchoule, E. Wertz, P. Senellart, and  
J. Bloch,, Phys. Rev. B, vol. 77, 113303 (2008).
- [13].A. A. Khalifa, A. P. D. Love, D. N. Krizhanovskii, M. S. Skolnick, and J. S.  
Roberts, Appl. Phys. Lett., vol. 92, 061107 (2008).
- [14].N. Antoine-Vincent, F. Natali, F. Byrne, A. Vasson, P. Disseix, J. Leymarie, M.  
Leroux, F. Semond, and J. Massies, Phys. Rev. B, vol.68, 153313 (2003).
- [15].T. Tawara, H. Gotoh, T. Akasaka, N. Kobayashi, and T. Saitoh, , Phys. Rev. Lett.  
vol. 92, 256402 (2004).
- [16].G. Christmann, R. Butté, E. Feltin, J. –F. Carlin, and N. Grandjean, , Phys. Rev.  
B vol. 73, 153305, (2006).
- [17].M. Zamfirescu, A. Kavokin, B. Gil, G. Malpuech, and M. Kaliteevski, Phys. Rev.  
B 65, 161205 (2002)
- [18].K. Kornitzer, T. Ebner, K. Thonke, R. Sauer, C. Kirchner, V. Schwegler, M.  
Kamp, M. Leszczynski, I. Grzegory, and S. Porowski, Phys. Rev. B 60, 1471  
(1999).
- [19].S. Nakamura, G. Fosol, and S. J. Pearton, The blue laser diode: the complete  
story, Berlin, New York, Springer, (2000).
- [20].T. Someya, R. Werner, A. Forchel, M. Catalano, R. Cingolani, and Y. Arakawa ,  
Science, vol. 285, 1905 (1999).



- [21]. Y. -K. Song, H. Zhou, M. Diagne, I. Ozden, A. Vertikov, A. V. Nurmikko, C. Carter-Coman, R. S. Kern, F. A. Kish, and M. R. Krames, *Appl. Phys. Lett.*, vol. 74, 3441 (1999).
- [22]. T. Tawara, H. Gotoh, T. Akasaka, N. Kobayashi, and T. Saitoh, *Appl. Phys. Lett.*, vol. 83, 830 (2003).
- [23]. A. Castiglia, D. Simeonov, H. J. Buehlmann, J. -F. Carlin, E. Feltin, J. Dorsaz, R. Butté, and N. Grandjean, *Appl. Phys. Lett.*, vol. 90, 033514, 2007.
- [24]. T. -C. Lu, C. -C. Kao, H. -C. Kuo, G. -S. Huang, and S. -C. Wang, *Appl. Phys. Lett.*, vol. 92, 141102, 2008
- [25]. M. Zamfirescu, A. Kavokin, B. Gil, G. Malpuech, and M. Kaliteevski, *Phys. Rev. B* 65, 161205(R)(2002).
- [26]. A. Imamoglu and J. R. Ram, *Phys. Lett. A* 214, 193 (1996).
- [27]. U. Ozgur, Y. I. Alivov, C. Liu, A. Teke, M. A. Reshchikov, S. Dogan, V. Avrutin, S. J. Cho, and H. Morkoc, *J. Appl. Phys.* 98, 041301 (2005).
- [28]. R. Shimada, J. Xie, V. Avruton, U. Ozgur, and H. Morkoz, *Appl. Phys. Lett.* 92, 011127(2008).
- [29]. R. Schmidt-Grund, B. Rheinlander, C. Czekalla, G. Benndorf, H. Hochmuth, A. Rahm, M. Lorenz, and M. Grundmann, *Superlattices Microstruct.* Vol.41, 360 (2007).
- [30]. R. Schmidt-Grund, B. Rheinländer, C. Czekalla, G. Benndorf, H. Hochmuth, M. Lorenz, and M. Grundmann, *Appl. Phys. B: Lasers Opt.*, 93, 331 (2008).

- [31].L. Sun, Z. Chen, Q. Ren, K. Yu, L. Bai, W. Zhou, H. Xiong, Z. Q. Zhu, and X. Shen, *Phys. Rev. Lett.* 100, 156403 (2008).
- [32].S. Christopoulos, G. Baldassarri Höger von Högersthal, A. J. D. Grundy, P. G. Lagoudakis, A. V. Kavokin, J. J. Baumberg, G. Christmann, R. Butté, E. Feltn, J. –F. Carlin, and N. Grandjean, *Phys. Rev. Lett.*, vol. 98, 126405, Mar.( 2007).
- [33].G. Christmann, R. Butté, E. Feltn, J. –F. Carlin, and N. Grandjean, *Appl. Phys. Lett.*, vol. 93, pp. 051102 (2008).
- [34]. Mark Fox, *Quantum Optics*, OXFORD university press, (2006)
- [35]. Mark Fox, *Optical Properties of Solids*, OXFORD university press, (2008)
- [36]. Hui Deng, Thesis “DYNAMIC CONDENSATION OF SEMICONDUCTOR MICROCAVITY POLARITONS” (2006)
- [37]. C. Klingshirn *et al.*, *Superlattices Microstruct.* 38, 209 (2005).
- [38]. Peiliang Chen *et al.*, *Appl. Phys. Lett.* 89, 111112 (2006).
- [39]. Lambert K. van Vugt *et al.*, *Phys. Rev. Lett.* 97, 147401(2006).
- [40]. R. Schmidt-Grund *et al.*, *Superlattices Microstruct.* 41, 360 (2007).
- [41]. F.B. Naranjo, S. Fernández, M.A. Sánchez-García, F. Calle, E. Calleja, *Appl. Phys. Lett.* 80 2198(2002).
- [42].M. Diagne, Y. He, H. Zhou, E. Makarona, A.V. Nurmikko, J. Han, K.E. Waldrip, J.J. Figiel, T. Takeuchi, M. Krames, *Appl. Phys. Lett.* 79 3720 (2001).
- [43].T.-C. Lu, J.-R. Chen, S.-W. Chen, H.-C. Kuo, C.-C. Kuo, C.-C. Lee, S.-C. Wang, *IEEE J. Sel. Topics Quantum Electron.* 15 850(2009).

- [44].E. Feltin, G. Christmann, J. Dorsaz, A. Castiglia, J.-F. Carlin, R. Butté, N. Grandjean, S. Christopoulos, G. Baldassarri, H. von Högersthal, A.J.D. Grundy, P.G. Lagoudakis, J.J. Baumberg, *Electron. Lett.* 43 924(2007).
- [45].G.S. Huang, T.C. Lu, H.H. Yao, H.C. Kuo, S.C. Wang, C.-W. Lin, L. Chang, *Appl. Phys. Lett.* 88 061904 (2006).
- [46].Charalambos C. Katsidis and Dimitrios I. Siapkas, *APPLIED OPTICS*, Vol. 41, 3978
- [47].S. Faure, T. Guillet, P. Lefebvre, T. Bretagnon, and B. Gil, *Phys. Rev. B* 78, 235323 (2008).
- [48].S. Faure, T. Guillet, P. Lefebvre, T. Bretagnon, and B. Gil ,“Comparison of strong coupling regimes in bulk GaAs, GaN, and ZnO semiconductor microcavities,” *Phys. Rev. B*, vol.78, 235323, (2008).
- [49].G. E. Jellison and L. A. Boatner, *Phys. Rev. B* 58, 3586 (1998).
- [50].R. J. Elliott, *Phys. Rev.* 108, 1384 (1957)
- [51]. A. Tredicucci, Y. Chen, V. Pellegrini, M. Böger, L. Sorba, F. Beltram, *Phys. Rev. Lett.* 75, 3906 (1995)
- [52]. R.M.A. Azzam, N.M. Bashara, *Ellipsometry and Polarized Light* (North-Holland, Amsterdam, 1977)
- [53]. N. Ollier, F. Natali, D. Byrne, P. Disseix, M. Mihailovic, A. Vasson, J. Leymarie, F. Semond, J. Massies, *Jpn. J. Appl. Phys.* 44, 4902 (2005)

- [54]. S. L. Chuang, *Physics of Photonic Devices, 2<sup>nd</sup> edition* (John Wiley & Sons, New Jersey, United States of America, 2009), p. 679-680.(2008)
- [55]. Y. Chen, A. Tredicucci, F. Bassani, *Phys. Rev. B* 52, 1800 (1995)
- [56]. M.D. Sturge, *Phys. Rev.* 127, 768 (1962)
- [57]. J.F. Muth, J.H. Lee, I.K. Shmagin, R.M. Kolbas, H.C. Casey, B.P. Keller, U.K. Mishra, S.P. DenBaars, *Appl. Phys. Lett.* 71, 2572 (1997)
- [58]. G.E. Jellison, L.A. Boatner, *Phys. Rev. B* 58, 3586 (1998)
- [59]. J.-R. Chen, T.-C. Lu, Y.-C. Wu, S.-C. Lin, W.-R. Liu, W.-F. Hsieh, C.-C. Kuo, C.-C. Lee, *Appl. Phys. Lett.* 94, 061103 (2009)
- [60]. R. Johne, D.D. Solnyshkov, G. Malpuech, *Appl. Phys. Lett.* 93, 211105 (2008)
- [61]. V. Savona, L.C. Andreani, P. Schewndimann, A. Quattropani, *Solid State Commun.* 93, 733 (1995)
- [62]. F. Réveret, F. Médard, P. Disseix, J. Leymarie, M. Mihailovic, A. Vasson, I.R. Sellers, F. Semond, M. Leroux, J. Massies, *Opt. Mater.* 31, 505 (2009)
- [63]. R. Butté, G. Christmann, E. Feltn, J.-F. Carlin, M. Mosca, M. Ilegems, N. Grandjean, *Phys. Rev. B* 73, 033315 (2006)
- [64]. F. Médard, J. Zuniga-Perez, P. Disseix, M. Mihailovic, J. Leymarie, A. Vasson, F. Semond, E. Frayssinet, J. C. Moreno, M. Leroux, S. Faure, T. Guillet, *Phys. Rev. B* 79, 125302 (2009)
- [65]. R. Shimada, J. Xie, V. Avrutin, Ü. Özgür, H. Morkoç, *Appl. Phys. Lett.* 92, 011127 (2008)

- [66]. W.Y. Liang, A.D. Yoffe, Phys. Rev. Lett. 20, 59 (1968)
- [67]. R. Rapaport, A. Qarry, G. Ramon, E. Cohen, A. Ron, L.N. Pfeiffer, Solid State Commun. 120, 387 (2001)
- [68]. J.R. Jensen, P. Borri, W. Langbein, J.M. Hvam, Appl. Phys. Lett. 76, 3262 (2000)
- [69]. M. Maghrebi Mellitia, R. Chtouroua, J. Blockb, V. Thierry-Miegb, Physica E, 30, 17 (2005)
- [70]. F. Médard, J. Zúñiga-Perez, E. Frayssinet, J.C. Moreno, F. Semond, S. Faure, P. Disseix, J. Leymarie, M. Mihailovic, A. Vasson, T. Guillet, M. Leroux, Photonics Nanostruct. Fundam. Appl. 7, 26 (2009)
- [71]. V. Savona, C. Piermarocchi, Phys. Stat. Sol (a), 164, 45 (1997)
- [72]. G. Christmann, R. Butté, E. Feltin, J.-F. Carlin, N. Grandjean, Appl. Phys. Lett. 93, 051102 (2008)
- [73]. G. Coli, K.K. Bajaj, Appl. Phys. Lett. 78, 2861 (2001)
- [74]. K. Koike, G.-Y. Takada, K. Fujimoto, S. Sasa, M. Inoue, M. Yano, Physica E, 32, 191 (2006)
- [75]. R.T. Senger, K.K. Bajaj, Phys. Rev. B, 68, 205314 (2003)
- [76]. S. Nakamura, T. Mukai, and M. Senoh, Appl. Phys. Lett. 64, 1687 (1995).
- [77]. I. Akasaki and H. Amano, Jpn. J. Appl. Phys. Lett. 36, 5393 (1997).
- [78]. S. Nakamura, Science 281, 956 (1998).
- [79]. T. Kobayashi, T. Segawa, Y. Morimoro, and T. Sueta, 46th Fall Meeting, Japan

- Appl. Phys. Soc., Fukuoka, Japan, Sep. 28–30, 1982, Paper 29a-B-6.
- [80]. H. Yokoyama and S. D. Broson, J. Appl. Phys. 66, 4801 (1989).
- [81]. Y. Yamamoto, S. Machida, and K. Igeta, 16th European Conf. Opt. Commun., Amsterdam, The Netherlands, Paper MoF4.6, Sep. 16–20, (1990).
- [82]. J. M. Redwing, D. A. S. Loeber, N. G. Anderson, M. A. Tischler, and J. S. Flynn, Appl. Phys. Lett. 69, 1 (1996).
- [83]. I. L. Krestnikov, W. V. Lundin, A. V. Semenov, A. S. Usikov, A. F. Tsatsul'nikov, N. N. Ledentsov, A. Hoffmann, and D. Bimberg, Appl. Phys. Lett. 75, 1192(1999).
- [84]. H. Zhou, M. Diagne, E. Makarona, A. V. Nurmikko, J. Han, K. E. Waldrip, and J. J. Figiel, Electron. Lett. 36, 1777 (2000).
- [85]. T. Someya, R. Werner, A. Forchel, M. Catalano, R. Cingolani, and Y. Arakawa, Science 285, 1905 (1999).
- [86]. F. Tassone and Y. Yamamoto, Phys. Rev. B 59, 10830 (1999).
- [87]. G. Malpuech, A. Kavokin, A. Di Carlo, and J. J. Baumberg, Phys. Rev. B 65, 153310(2002).
- [88]. D. Porras, C. Ciuti, J. J. Baumberg, and C. Tejedor, Phys. Rev. B 66, 085304 (2002).
- [89]. R. Balili, V. Hartwell, D. Snoke, L. Pfeiffer, and K. West, Science 316, 1007 (2007)
- [90]. J. Kasprzak, M. Richard, S. Kundermann, A. Baas, P. Jembrun, J. M. J. Keeling,

- F. M. Marchetti, M. H. Szymanska, R. André, J. L. Staehli, V. Savona, P. B. Littlewood, B. Deveaud, and L. S. Dang, *Nature (London)* 443, 409 (2006)
- [91].S. Christopoulos, G. Baldassari, A. J. D. Grundy, P. Lagoudakis, A. V. Kavokin, J. J. Baumberg, G. Christmann, R. Butte, E. Feltin, J.-F. Carlin, and N. Grandjean, *Phys. Rev. Lett.* 98, 126405 (2007)
- [92].J. R. Tischler, M. S. Bradley, V. Bulovic, J. H. Song, and A. Nurmikko, *Phys. Rev. Lett.* 95, 036401 (2005)
- [93].L. Sapienza, A. Vasanelli, R. Colombelli, C. Ciuti, Y. Chassagneux, C. Manquest, U. Gennser, and Carlo Sirtori, *Phys. Rev. Lett.*
- [94].T. Tawara,\* H. Gotoh, T. Akasaka, N. Kobayashi,† and T. Saitoh, *Phys. Rev. Lett* (2004)
- [95].Y. Narukawa, Y. Kawakami, S. Fujita, S. Fujita, and S. Nakamura, *Phys. Rev. B* 55, R1938 (1997).
- [96].Y. Narukawa, Y. Kawakami, S. Fujita, and S. Nakamura, *Phys. Rev. B* 59, 10 283 (1999).
- [97].S. F. Chichibu, T. Azuhata, T. Sota, T. Mukai, and S. Nakamura, *J. Appl. Phys.* 88, 5153 (2000).
- [98].Kian-Giap Gan, and John E. Bowers, *IEEE Photonic Tech L*, VOL. 16, 1256, (2004)
- [99].Jiunn-ChyiLee, Ya-FenWu, Yi-PingWang, Tzer-EnNee, *J. Cryst. Growth* vol. 310, 5143 (2008)



[100]. M. Pophristic, F. H. Long, C. Tran, I. T. Ferguson, and R. F. Karliceck, Jr., J.

Appl. Phys, vol. 86, 1114.

[101]. Zeki Yarar Solid State Commun., vol. 147, 98

